CLINAM

European Foundation for Clinical Nanomedicine

13/2022

Basel, May 2–4

POSTER SESSION

POSTER

CLINAM 2022

CHITOSAN-BASED QUININE THERMOSENSITIVE GELS FOR THE INTRANASAL TREATMENT OF CEREBRAL MALARIA IN RURAL AREAS IN SUB-SAHARAN AFRICA

Agbo C.P.[1*], Nwabueze H.U.[1], Offor E.N.1, Ubachukwu U. [1], Ugwuanyi T.C. [1], McConville C.[2], Ofokansi K.C.[1], Attama A.A.[1]

[1]Department of Pharmaceutics, Faculty of Pharmaceutical Sciences, University of Nigeria, Nsukka, Enugu State, Nigeria.

[2]School of Pharmacy, Institute of Clinical Sciences, College of Medical and Dental Sciences, Sir Robert Aitken Institute for Medical Research, University of Birmingham.

Introduction: Intranasal route of drug administration provides a safe and convenient alternative to access the central nervous system for the treatment of diseases such as cerebral malaria. However, nasal clearance of drugs prevents significant permeation of drugs from nasally administered formulations. Chitosan is a natural polymer, a permeation enhancer and a gel forming agent used for the design of drug delivery systems.

Aim: This research was aimed at formulating chitosan-based quinine (QHCl) thermosensitive gels (TSG) having characteristics for surmounting the challenges encountered with intranasal administration, and serve as an alternative to parenteral quinine for the treatment of cerebral malaria.

Methods:

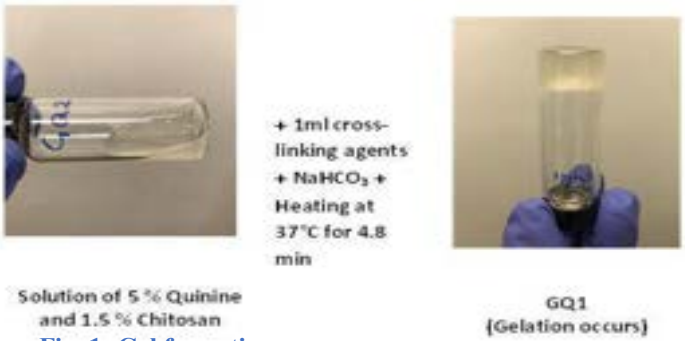

Fig. 1: Gel formation process

Results:

Tab. 1 : Gelling time and temperatures of QHCl-TSGs

BATCH	GELLING TIME (MIN)	GELLING TEMPERATURE (°C)
GQ1	4.8 ± 0.30	34.3 ± 2.9
GQ2	3.4 ± 0.41	28.4 ± 1.0

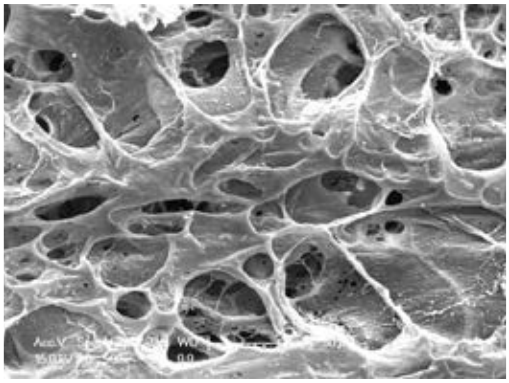

GQ1 surface structure 500 x

Fig. 2: SEM Image of quinine TSGs

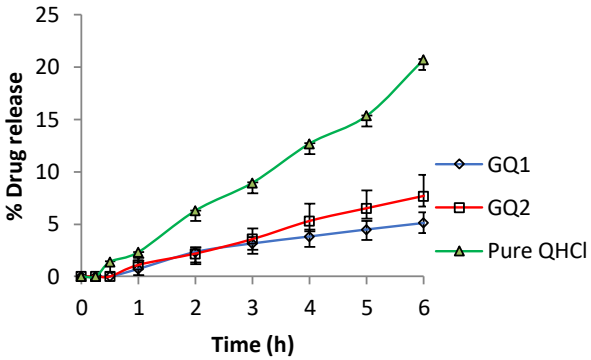

Fig. 3: *In vitro* release of QHCl from TSGs in SNF.

Highlights:

- QHCl TSGs were successfully formulated and demonstrated rapid gelation at 37 ± 2°C with gelling times being ≤ 4.8 ± 0.03 min.
- Scanning electron microscope images of gels showed crosslinking, as well as porous gel networks which should permitted drug release.
- Both *in vitro* and *ex vivo release* studies in pig nasal mucosa showed that quinine release from TSG was more sustained than unprocessed pure QHCl over a long period of time.

Conclusion:

The characteristics of the QHCl TSG formulated has potentials for successful intranasal administration.

Soft biomimetic lipid membrane-based nanoparticle carriers of neuroprotective compounds

Borislav Angelov[1,*], Markus Drechsler[2], and Angelina Angelova[3]

[1] Institute of Physics, ELI Beamlines, Academy of Sciences of the Czech Republic, Na Slovance 2, CZ-18221 Prague, Czech Republic,
[2] Keylab "Electron and Optical Microscopy", Bavarian Polymerinstitute (BPI), University of Bayreuth, D-95440 Bayreuth, Germany
[3] Université Paris-Saclay, CNRS, Institut Galien Paris-Saclay UMR8612, F-92290 Châtenay-Malabry, France

Contact: borislav.angelov@eli-beams.eu

Executive Summary

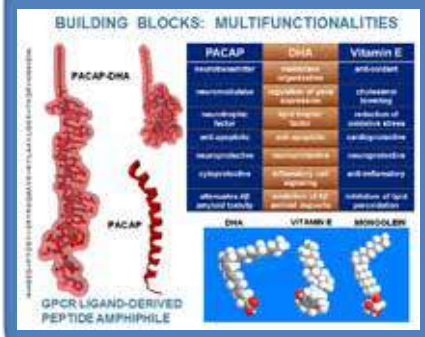

Delivery of natural compounds promoting the neurotrophin receptor signaling in the central nervous system (CNS) present ongoing interest for combination therapy development. Recent research on human SARS-CoV-2 coronavirus has emphasized that COVID-19 can affect the brain depending on the severity of the viral infection. Coronavirus-provoked inflammatory changes, cerebrovascular and ischemic lesions can cause neuronal and axonal damages, which last several months and may lead to post-COVID-19 neuronal dysfunction and neuropsychiatric complications. It can be suggested that nanomedicine-based strategies may help for recovery from the neuronal damages in the post-COVID-19 infection related to early Parkinsonism and other neurological disorders. Here we investigated a synthetic construct of the pituitary adenylate cyclase-activating polypeptide (PACAP38) coupled to a docosahexaenoic acid (DHA: an ω3-PUFA) in order to create liquid crystalline assemblies from neuroprotective compounds. The hormone PACAP38 is a ligand of the class B PAC1 G-protein-coupled receptor (GPCR), whereas DHA is a lipid trophic factor. The lipidated peptide PACAP-DHA is co-assembled into hierarchical nanostructures elaborated from hybrid vesicle-micelle reservoirs as well into PEGylated cubosomes composed of multiple neuroprotective building blocks.

Results of SAXS Analysis

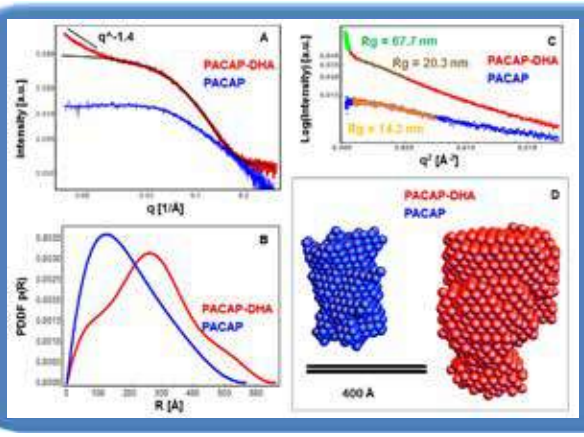

(A) Small-angle X-ray scattering (SAXS) of the lipidated peptide hormone PACAP-DHA (PACAP bound to a docosahexaenoic acid DHA) at concentration 29 mg/mL (red plot) and of the native PACAP peptide (blue plot; 10 mg/mL). The fitted plot without large aggregates (black curve overlay) visibly deviates from the aggregation slope (black line). (B) Pair Distance Distribution Functions (PDDF) corresponding to PACAP (blue plot) and PACAP-DHA (red) solutions. (C) Guinier plot for determination of the Rg in case of the aggregated PACAP-DHA (green overlay) and non-aggregated PACAP-DHA (brown overlay) and PACAP (orange overlay). (D) 3D dummy atom models derived from the PDDF (panel B) for PACAP (blue) and PACAP-DHA (red).

Cryo-TEM

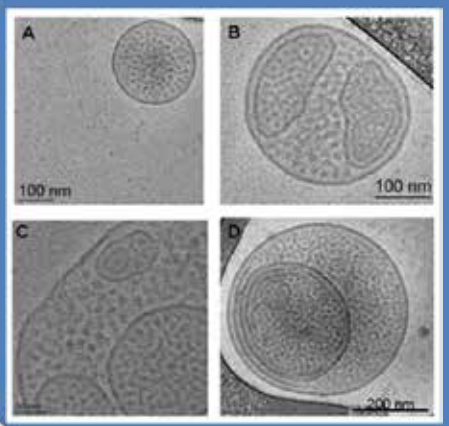

Cryo-TEM images of pep-lipid assemblies with internal compartments: Membrane-mimetic environment of DHA/vitamin E/VPGS-PEG1000 (54/23/23 molar ratio) (A) into which the peptide PACAP is embedded at a concentration 4 mg/mL (B). (C,D) PACAP-DHA/vitamin E/VPGS-PEG1000 assemblies obtained at an equivalent molar ratio of the lipid components as in (A,B). The PACAP-DHA concentration is 1 mg/ml for the sample volume. The observed hierarchical organization comprises a coexistence of small micelles and compartmentalized vesicles. The generated vesicular membranes evolve to close shells that encapsulate small pep-lipid aggregates (D).

Acknowledgement

The performed research was funded by the projects "Advanced research using high-intensity laser produced photons and particles" (CZ.02.1.01/0.0/0.0/16_019/0000789) and "Structural Dynamics of Biomolecular Systems" (ELIBIO) (CZ.02.1.01/0.0/0.0/15_003/0000447) from the European Regional Development Fund. AA acknowledges a membership in CNRS GDR2088 BIOMIM network.

References

1. Angelova, A.; Drechsler, M.; Garamus, V.M.; Angelov, B., ACS Omega, 2018, 3, 3235-3247.
2. Rakotoarisoa, M.; Angelov B., Garamus, V. M.; Angelova, A. ACS Omega, 2019, 4, 3061-3073.
3. Angelova, A.; Angelov, B., Garamus, V.M.; Drechsler, M., J. Mol. Liq., 2019, 279, 518-523.
4. Angelov, B.; Garamus, V. M.; Drechsler, M.; Angelova, A., J. Mol. Liq., 2017, 235, 83-89.
5. Angelov, B.; Angelova, A.; Filippov, S.; Drechsler, M. et al. ACS Nano, 2014, 8, 5216-5226.
6. Angelova, A., Drechsler, M, V.M. Garamus, Angelov, B, ChemNanoMat, 2019, 5, 1381–1389.

Liposomal Celecoxib Combined with Dendritic Cell Therapy in B16F10 Mouse Model for Melanoma

Leila Arabi1,2*; Vajiheh Jahani1; Mona Yazdani1; MahmouReza Jaafari1,2
1-Nanotechnology Research Center, School of Pharmacy, Mashhad University of Medical Sciences, Mashhad Iran.
2-Department of Pharmaceutical Nanotechnology, School of Pharmacy, Mashhad University of Medical Sciences, Iran, * Presenting Author
leilaa.arabi@gmail.com, Arabil@mums.ac.ir

INTRODUCTION

The immunosuppressive nature of the tumor microenvironment caused by immunosuppressive cells like regulatory T cells (Tregs), inflammation and inhibitory factors limit the effectiveness of anticancer vaccines. Inspired by the role of cyclooxygenase-2 (COX-2) in inflammation in tumor site as well as induction of Tregs, we proposed that normalization of tumor microenvironment by celecoxib as a COX-2 inhibitor might improve the efficacy of dendritic cell (DC) therapy in a melanoma model. In the present study, liposomal celecoxib was combined with ex vivo generated DC vaccines pulsed with gp100 antigen (in liposomal and non-liposomal forms) in both a prophylactic and therapeutic model.

STUDY DESIGN AND METHODOLOGY

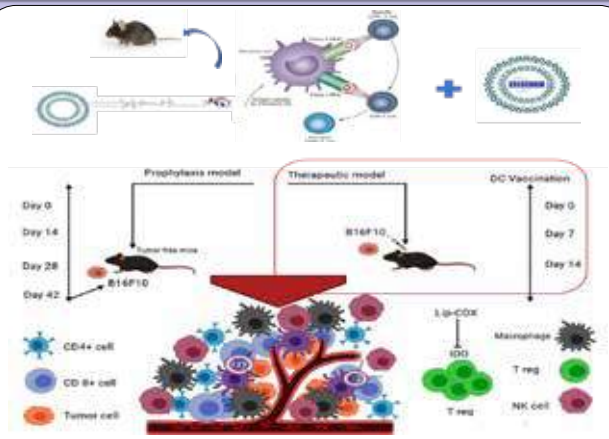

The thin film plus sonication method was used for the preparation of liposomes. Liposomal celecoxib was combined with dendritic cells matured by gp-100 peptide linked to the liposomes. Liposomal formulations containing gp-100 peptide and celecoxib were characterized. Linking of peptide to maleimide-PEG2000-DSPE through covalent binding between the thiol group of C terminal cysteine residue of peptide and maleimide (1).

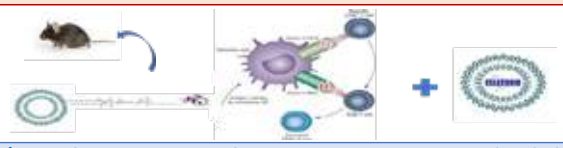

C57BL/6 mice bearing B16F10 melanoma tumors were vaccinated with different formulations of gp-100 peptide in combination with IV administration of liposomal celecoxib.

Immunological tests such as ELISpot assay, flow cytometry and cytotoxicity assay were performed on splenocyte suspensions (2), and the remaining mice were evaluated for tumor growth and survival analysis.

RESULTS

Therapeutic combination of liposomal celecoxib and gp-100 demonstrated an effective immune response and tumor regression in C57BL/6 mice bearing B16F10 melanoma.

The combinational therapy of dendritic cells + liposomal gp-100peptide + liposomal celecoxib leads to a significant amount of IFN-γ secretion and increased number tumor infiltrated lymphocytes (TILs) and cytotoxic activity

In this study, therapeutic combination of liposomal celecoxib and gp-100 demonstrated an effective immune response and tumor regression in C57BL/6 mice bearing B16F10 melanoma (figure). The significant tumor growth inhibition by combination therapy (DC+peptide/Lip-peptide+Lip-COX) could be a result of increased IFN-Y secretion alongside the cytottoxic activity of T cells.

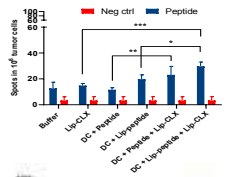

In vivo therapeutic efficacy of different liposomal formulations and tumor volume (mm3) of each mouse in each treatment group were evaluated and compared with Buffer groups. The values are means of tumor size ± SEM. Survival analysis of therapeutic groups were monitored by the multiple comparison log-rank (Mantel–Cox) test. Effects of treatments on survival time were monitored for a period of 30 days among B16F10 tumor model of C57BL/6 mice (n=6).

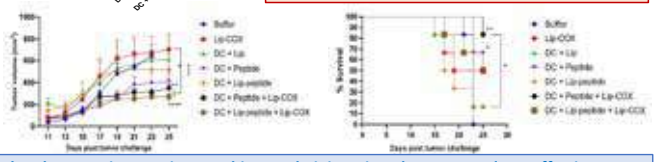

In the therapeutic experiment, this co-administration demonstrated an effective tumor regression and enhanced survival compared to the other groups.

CONCLUSION

In conclusion, our findings suggest that DC therapy alongside liposomal celecoxib has a significant effect on immune responses and enhanced therapeutic outcomes in a mouse model of melanoma and this combination therapy may have great potential to improve the immunotherapy in solid tumors.

REFERENCES

1- Matbou Riahi, M., et al. Int J Pharm, 2018. 540(1-2): p. 89-97.
2- Zamani, P et al., Journal of Controlled Release 303 (2019) 223–236

RCSI

Development of inhalable Retinoic acid-loaded polymeric nanoparticles as targeted host directed immunotherapy for *Mycobacterium tuberculosis*

Ahmad Z.Bahlool [1,2,3], Sarinj Fattah[1,2,4], Andrew O'Sullivan[1,5], Brenton Cavanagh[6] , Ronan MacLoughlin[5] , Joseph Keane[3], Mary P O'Sullivan [3], Sally-Ann Cryan[1,2,4,7]

[1] School of Pharmacy and Biomolecular Sciences, Royal College of Surgeons in Ireland (RCSI), 123 St Stephens Green, Dublin, Ireland.
[2] Tissue Engineering Research Group, Royal College of Surgeons in Ireland (RCSI), 123 St Stephens Green, Dublin, Ireland.
[3] Department of Clinical Medicine, Trinity Translational Medicine Institute, St. James's Hospital, Trinity College Dublin, The University of Dublin, Dublin 8, Ireland.
[4] SFI Centre for Research in Medical Devices (CÚRAM), NUIG & RCSI, Dublin, Ireland.
[5] Aerogen Ltd, Galway Business Park, Dangan, Galway, Ireland
[6] Cellular and Molecular Imaging Core, Royal College of Surgeons in Ireland RCSI, Dublin 2, Ireland.
[7] SFI Advanced Materials and Bioengineering Research (AMBER) Centre, RCSI and Trinity College Dublin, Dublin, Ireland.

RCSI DEVELOPING HEALTHCARE LEADERS WHO MAKE A DIFFERENCE WORLDWIDE

Introduction

Tuberculosis (TB) is the **top bacterial infectious disease killer** and one of the top ten causes of death worldwide. **The emergence of strains of multiple drug-resistant tuberculosis (MDR-TB)** has pushed our available stock of anti-TB agents to the limit of effectiveness. An adjunctive**, host-directed therapy (HDT) designed to act on the host**, instead of the bacteria, by boosting the host immune response through activation of intracellular pathways could help address this issue. The integration of multidisciplinary approaches of repurposing currently FDA-approved drugs, with a targeted drug-delivery platform is a very promising option to accelerate new therapeutics reaching the clinic. Previous work conducted by our group showed the efficacy of All Trans Retinoic Acid (ATRA) as a HDT toward TB both *in vitro* and *in vivo.* **The goal of this project is to develop Poly-Lactic-co-Glycolic Acid (PLGA) nanoparticles (NPs) to target ATRA to the lungs via inhalation and enhance uptake by alveolar macrophages (AM) which are the host cells for *Mtb*.**

Successful development of a scalable formulation of ATRA-PLGA NPs with desired physicochemical characteristics:

Table 1: Physicochemical properties of ATRA-PLGA nanoparticles; nanoparticles were formulated using nanoprecipitation method or Ignite Nanoassemblr® microfluidics system (1:20 w/w drug:polymer) . All loaded formulations were purified using centrifugation, disrupted in 1:10 (v/v) NPs/MeOH. Drug content was quantified by UV-Vis at 348 nm. The average hydrodynamic size, PDI and zeta potential of PLGA NPs were measured by the Nanosizer ZS90 (Malvern, UK) using dynamic light scattering and electrophoretic mobility. Data shown as mean ± SD (n =3). PDI: Polydispersity index, EE: Encapsulation efficiency.

Manufacturing method	Size (nm)	PDI	Surface charge (mV)	EE%
Bench Scale	251.6 ±9.7	0.187 ± 0.030	-1.80 ±0.410	69.8 ± 12.4
Microfluidics	260.8 ± 9.49	0.187 ± 0.011	- 1.90 ± 0.620	76.4 ± 5.4

ATRA-PLGA NPs showed a dose response effect against bacterial growth

Figure 1: ATRA treatment arrests growth of Mtb (H37Ra) in infected THP-1 derived macrophages Efficacy of treatment was assessed at A) 72 hrs and B) 120 hrs post-treatment by monitoring the change in bacterial growth (%), using the BacT/ Alert® 3D system (bioMerieux), MOI: 1–10/cell (n=3).

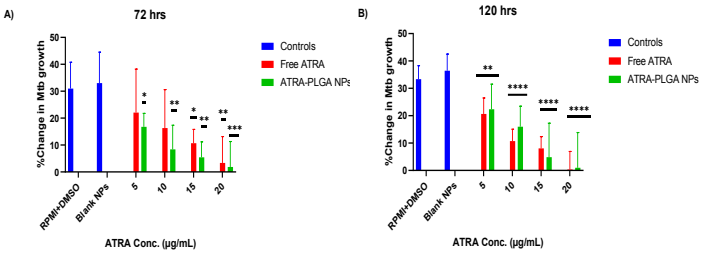

ATRA-PLGA NPs have no toxicity on airway cells *in vitro*

Figure 2: The effect of ATRA treatment on cell viability. Cell viability of THP-1 macrophages or A549 alveolar epithelium was determined by MTS assay 72 hrs post-treatment. Toxicity studies were carried out in the absence of Mtb infection (H37Ra). Dotted lines represents 50% viability as cut-off toxicity value. Results were plotted as (%) Metabolic activity relative to RPMI group. Data shown as mean ± SD (n = 3).

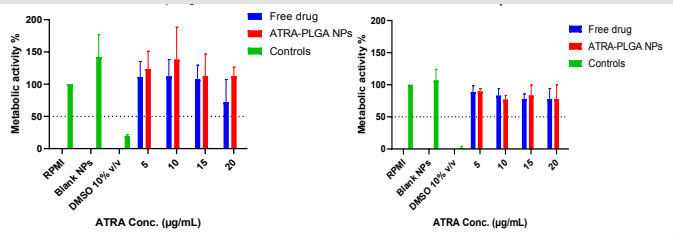

Nebulized ATRA-PLGA NPs showed an optimum droplet size required for aerosol deposition in the lung (**1-5 µm**)

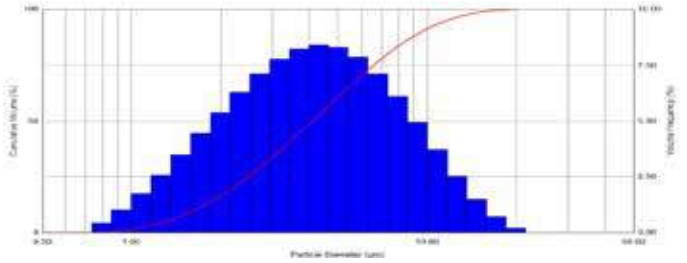

Figure 3: Particle size distribution of nebulized droplets of ATRA-PLGA nanoparticles aerosolized using Aerogen Solo® vibrating mesh nebulizer as measured by laser diffraction via Malvern spraytec.

Volume Median Diameter (µm): 4.09 ± 0.01

Nebulized NPs potentially indicate properties to deliver ATRA to peripheral airways

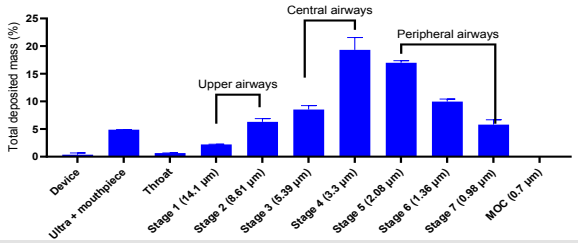

Figure 4: Quantification of the deposited ATRA-PLGA NPs aerosolized using Aerogen Solo® vibrating mesh nebulizer . Mass distribution of nebulized nanoparticles was determined using Westech 7 impactor (Westech, UK). Results are expressed as the percentage of total drug deposited on all stages of the impactor including the throat and was represented by the mean ± standard deviation. The data are represented as mass percentage of nominal dose (n = 3).

~ Half of the delivered dose deposited in the terminal bronchi and alveolar region (TB-infection area)

High dose delivery in simulated normal adult breathing pattern

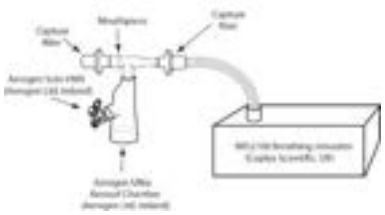

Courtesy of Aerogen

Adult breathing profile:
15 breaths per minute (BPM)
Inhalation to exhalation (I:E) ratio: 1:1
Tidal volume: 500 mL

65.1% of the dose was inhaled

Conclusions and future perspective :

- Demonstrated the ***in vitro* efficacy and cell biocompatibility** of ATRA-PLGA-NPs in macrophages and alveolar epithelium cells
- Successful integration of the ATRA nanoformulation with Aerogen Solo® nebulizer to enable **efficient delivery to the site of TB infection** in the lungs
- 65.1% of the dose was inhaled in simulated normal adult breathing pattern which higher than many commercially available inhalers for respiratory diseases
- **Scalable and reproducible manufacturing** protocol for ATRA-PLGA NPs using Ignite Nanoassemblr® microfluidics system
- Future work will include the assessment of efficacy and toxicity of ATRA-PLGA NPs in a clinically relevant ***in vivo* model**

Acknowledgment: RCSI Strategic Academic Recruitment (StAR) PhD program

@ahmadbahlool Ahmad Bahlool Ahmadbahlool@rcsi.com

RCSI Leading the world to better health
Trinity College Dublin
ST. JAMES'S HOSPITAL
Aerogen

Rafal Baker

Nose-to-brain Delivery of Riluzole-loaded Nanoparticles for The Treatment of Amyotrophic Lateral Sclerosis (ALS)

Institute of Pharmaceutical Science, Faculty of Life Sciences and Medicine, King's College London

Rafal Baker, Julie Tzu-Wen Wang, Shunping Han, Ben Forbes, Sukhi Bansal & Khuloud Al-Jamal

INTRODUCTION

- ALS is a fatal neurodegenerative disorder affecting motor neurones where death due to respiratory failure happens within 3 years of symptoms onset.[1]
- ALS drug of choice, **Riluzole** [**RLZ**], has poor efficacy, and is associated with hepatic side effects.[2]
- Nose-to-brain (N2B) delivery offers a convenient, non-invasive direct mean of transport to the brain and spinal cord through the olfactory and trigeminal nerves, bypassing the BBB.[3]

HYPOTHESES & AIMS

We ***hypothesise*** that encapsulation of RLZ in polymeric nanoparticles improves its aqueous solubility & eliminates the need for organic solvents. Intra-nasal administration increases CNS bioavailability and reduce systemic absorption.

This project ***aims*** to:

1. Formulate biocompatible RLZ nanoparticles, suitable for N2B delivery **(Figure 1.A)**
2. Synthesise and characterise radiolabelled RLZ for quantitative *in vivo* studies. **(Figure 1.A)**
3. Evaluate ^{14}C-RLZ amounts in major organs following administration in healthy mice **(Figure 1.B)**

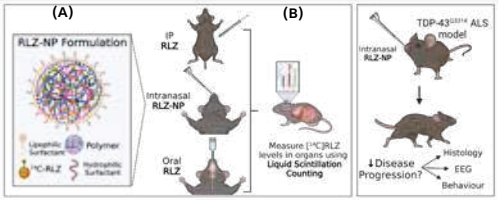

METHODOLOGY

1) Solution-phase synthesis of RLZ

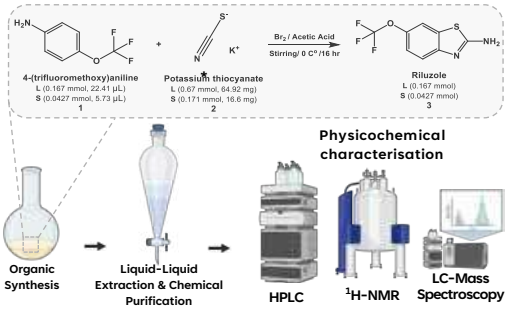

2) Preparation & characterisation of RLZ-NP

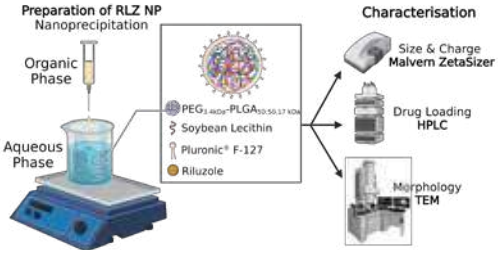

3) *In vivo* biodistribution studies in C57BL/6 mice

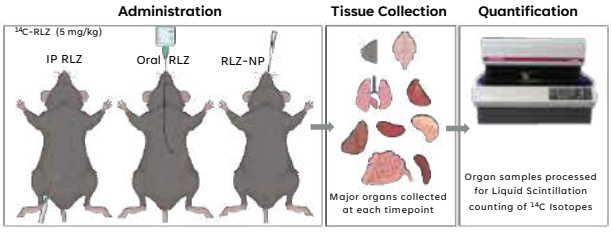

RESULTS

1) Solution-phase synthesis of RLZ

Scale[a]	% Yield[b] (mass)	% Yield[c] (HPLC)
Large (n=2)	78.14 ±2.15	N/A
Small (n=5)	73.18 ±15.64	33.4 ±16.48

- *Data expressed as average ± SD*
- *[a] Large & small refer to 39 and 10 mg theoretical RLZ yield, respectively.*
- *[b] based on pure product mass*
- *[c] based on HPLC analysis of pure product*

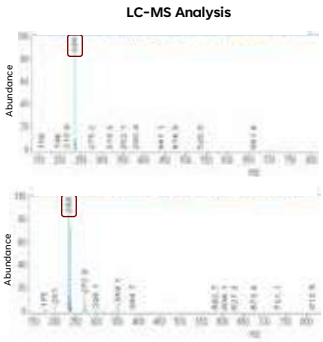

- Cold RLZ synthesis gave a calculated yield of ~75% based on product mass, and ~33% based on HPLC analysis.
- LC-MS showed experimental M_{wt} of product matches that of riluzole (234 Da).
- The specific radioactivity of ^{14}C-RLZ is ~35 µCi/mg

RESULTS CONT.

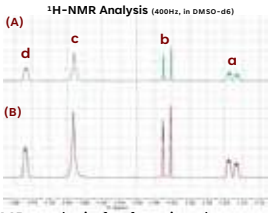

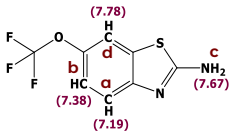

- ^{1}H-NMR analysis for functional groups peaks of product (A) compared to commercial RLZ (B) in the region of 7-8 ppm confirms synthesis product is RLZ.

2) Preparation & characterisation of RLZ-NP

NP type	Z-Average (d.nm)	PdI	Zeta Potential (mV)	EE%	DL%
Blank-NP$_{75:25}$	122.9 ±4.0	0.21 ±0.03	-27.6 ±0.03	-	-
RLZ-NP$_{75:25}$	109.8 ±8.4	0.18 ±0.05	-30.8 ±0.74	14.08 ±3.05	2.49 ±0.72
RLZ-NP$_{50:50}$	112.6 ±3.3	0.17 ±0.03	-30.4 ±1.34	11.94 ±0.25	2.14 ±0.16
PEG-RLZ-NP$_{50:50}$	99.3 ±2.5	0.19 ±0.02	-9.9 ±1.3	19.7 ±4.7	3.16 ±0.75

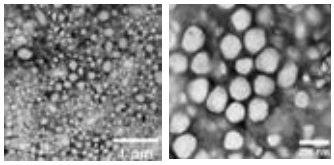

Figure 4. Transmission Electron Microscopy (TEM) images of PEG-RLZ-NP stained with UA-Zero®

- PEG-RLZ-NP had appropriate characteristics for intranasal administration and had EE% of ~20% thus it was taken further.
- TEM imaging confirmed that the particles were monodispersed and spherical in shape.

3) *In vivo* biodistribution studies in C57BL/6 mice

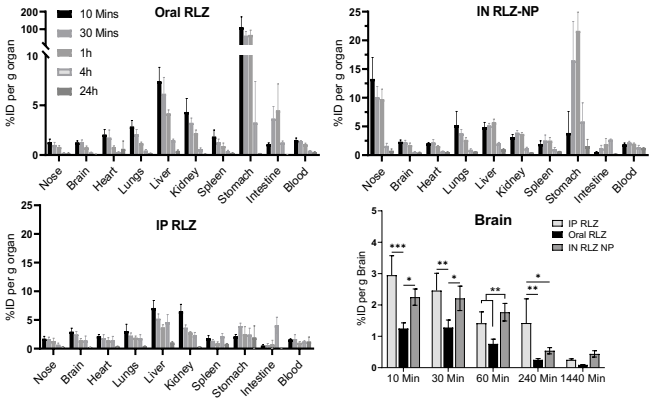

- The brain uptake order was IP (invasive route)> IN> Oral (clinically used).
- RLZ achieves its highest concentration in the brain within 10-30 min post administration, followed by a gradual reduction to less than 0.5% injected dose per gram brain after 24 hours.
- In addition to direct delivery to the brain, RLZ can be absorbed systemically after IN administration, enabling a systemic access route to the brain *via* the BBB.

CONCLUSIONS & FUTURE WORK

- The formulated RLZ-NP offers promising characteristics for N2B delivery.
- RLZ-NP demonstrated a superior brain bioavailability compared to oral delivery currently used by patients.
- Despite higher brain delivery achieved compared to oral delivery, systemic administration could not be avoided.
- Therapy studies in TDP-43^{Q331K} ALS mice models after RLZ-NP & oral RLZ administration will conclude on the utility of RLZ-NP for ALS therapy.

REFERENCES

[1] Shatunov, A., & Al-Chalabi, A. (**2020**). *The genetic architecture of ALS. Neurobiology of Disease, 105156.*
[2] Miller, R. G. (1996). Clinical trials of riluzole in patients with ALS. Neurology, 47(4 Suppl 2), 86S-92S.
[3] Illum, L. (**2003**). Nasal drug delivery—possibilities, problems, and solutions. *Journal of controlled release, 87*(1-3), 187-198.
[4] Bruschi, M.L. Strategies to Modify the Drug Release from Pharmaceutical Systems; **2015**; Chapter 6; pp. 87–194.

Danielle Brain

Assessment of cell phenotype following repeat exposure to NRTIs: FTC and 3TC

Danielle E. Brain[1], Christopher A.W. David [1], and Neill J. Liptrott [1].

[1]Department of Pharmacology and Therapeutics, Institute of System of Molecular and Integrative Biology, University of Liverpool, Liverpool, UK

Introduction

- HIV treatment requires chronic exposure to antiretrovirals, as it is incurable (Ruelas & Greene, 2013).
- Long-acting formulations of antiretroviral medication can help to improve adherence to medication, resulting in better treatment outcomes (Chandiwana et al., 2021).
- Currently nucleoside reverse-transcriptase inhibitors (NRTIs): emtricitabine (FTC) and lamivudine (3TC) are being explored in long-acting delivery.
- A key question in this type of delivery is, with long-acting formulations, does chronic exposure of the drugs to human cells alter their phenotype?

Repeated Exosure of the cell lines to FTC and 3TC

- **Cells in culture** - THP-1, MUTZ-3, CEM, or KU812
- **Drug molecule** - FTC (1.8 µg/mL), or 3TC (2 µg/mL)
- Repeat exposure of the cell lines to FTC or 3TC was carried out for 7 weeks and cells were passaged twice weekly.

Cell Health Assessments

- CellROX™ Green reagent used to detect ROS levels.
- ThiolTracker™ Violet used to detect reduced glutathione levels.
- JC-1 reagent used to measure mitochondrial membrane potential.

Exposure of Cells to Positive Controls and Marker Expression Analysis

- Cells were treated with positive controls depending on the cell type.
  - THP-1 = LPS
  - MUTZ-3 = LPS or Resiquimod (R848)
  - KU812 = C5a or Calcium ionophore
  - CEM = PHA
- Cells were stained with antibodies for specific activation markers depending on the cell line tested.

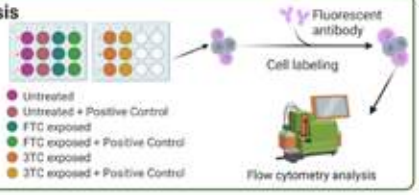

THP-1

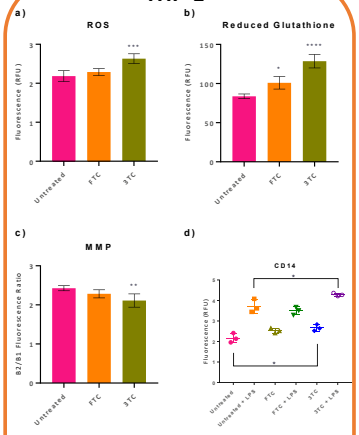

Figure 1: a) Intracellular ROS, n=4, mean ± SD. b) Intracellular reduced glutathione, n=4, mean ± SD. c) MMP, n=4, mean ± SD. d) CD14 expression, as assessed by flow cytometry n=3, mean ± SD. P <0.0001 = ****, P<0.001 = ***, P <0.01 = ** and P <0.05 = *.

- Intracellular **ROS levels were significantly higher** in the 3TC-cultured cells than the untreated cells (P= <0.001).
- Intracellular **reduced glutathione levels were also significantly higher** in both the FTC- and 3TC-cultured cells compared to those untreated (P= <0.05 and P= <0.0001 respectively).
- 3TC-cultured cells also demonstrated a significantly **lower MMP** (P= <0.01).
- When compared to the untreated, **3TC-treated** cells showed a significantly **higher expression of CD14** (P= <0.05). When compared to the LPS-treated cells, the **3TC-cultured LPS-treated cells showed significantly higher CD14 expression** (P = <0.05).

MUTZ-3

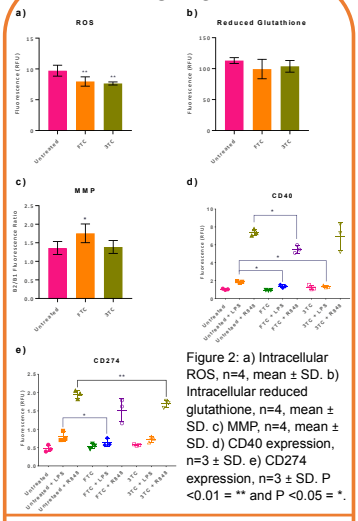

Figure 2: a) Intracellular ROS, n=4, mean ± SD. b) Intracellular reduced glutathione, n=4, mean ± SD. c) MMP, n=4, mean ± SD. d) CD40 expression, n=3 ± SD. e) CD274 expression, n=3 ± SD. P <0.01 = ** and P <0.05 = *.

- Intracellular **ROS levels were significantly lower** in the FTC- and 3TC-cultured cells, than the untreated cells (P= <0.01).
- **FTC-cultured cells displayed a significantly higher MMP** (P= <0.05).
- When compared to the **LPS-treated cells, the FTC- and 3TC-cultured LPS-treated cells showed a significantly lower CD40 expression** (P = <0.05). **FTC-cultured R848-treated cells** in comparison with the R848-treated cells showed significantly **lower CD40 expression** (P = <0.05).
- When compared to the LPS-treated cells, the **FTC-cultured LPS-treated** cells showed a significantly **lower CD274 expression** (P = <0.05). **3TC cultured, R848-treated cells** when compared to the R848-treated cells showed a significantly **lower CD274** expression (P = <0.01).

CEM

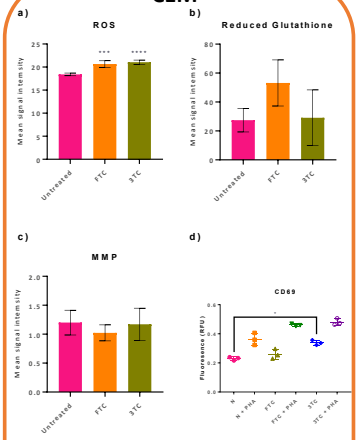

Figure 4: a) Intracellular ROS, n=4, mean ± SD. b) Intracellular reduced glutathione, n=4, mean ± SD. c) MMP, n=4, mean ± SD. d) CD69 expression, n=3 ± SD. P <0.0001 = ****, P <0.001 = *** and P <0.05 = *.

- Intracellular **ROS levels were significantly higher** in the FTC- and 3TC-cultured cells, than the untreated cells (P= <0.001 and P < 0.0001 respectively).
- No significant differences were seen for the reduced glutathione levels or the mitochondrial membrane potential for either the FTC- or 3TC-cultured cells.
- When compared to the Untreated cells, the **3TC-cultured cells** showed a significantly **lower CD69 expression** (P = <0.05).

KU812

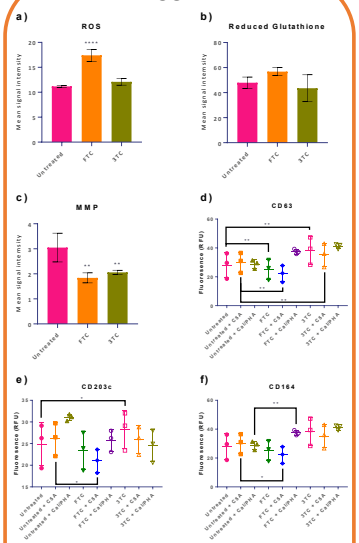

Figure 3: a) Intracellular ROS, n=4, mean ± SD. b) Intracellular reduced glutathione, n=4, mean ± SD. c) MMP, n=4, mean ± SD. d) CD63 expression, n=3 ± SD. e) CD203c expression. F) CD164 expression, n=3 ± SD. P <0.0001 = ****, P <0.01 = ** and P <0.05 = *.

- Intracellular **ROS levels were significantly higher in the FTC-cultured cells**, than the untreated cells (P= <0.0001).
- FTC- and 3TC-cultured cells displayed a **significantly lower MMP** (P= <0.01).
- When compared to the **FTC- and 3TC-cultured C5A-treated cells, the C5A-treated cells showed a significantly lower or higher CD63 expression respectively** (P = <0.01). When compared to the untreated cells, the **FTC- and 3TC-cultured cells showed a significantly lower or higher CD63 expression respectively** (P = <0.01).
- **3TC-cultured cells** cells in comparison with the Untreated cells showed significantly **higher CD203c expression** (P = <0.05). **FTC-cultured C5A-treated** cells when compared to C5A-treated cells showed significantly **lower CD203c** expression (P< 0.05).
- **FTC-cultured C5A-treated** cells when compared to the C5A-treated cells showed a significantly **lower CD164** expression (P = <0.05). **FTC-exposed Calcium Ionophore/PHA-treated** cells when compared to Calcium Ionophore/PHA-treated cells had a **higher expression of CD164** (P< 0.01).

Conclusions

- Higher production of ROS would intuitively be associated with a lower amount of reduced glutathione. In THP-1, CEM and KU812 cell lines, however, we have observed the opposite for some of the treated cells. This may be a consequence of prolonged increased ROS levels, leading to a greater intracellular reserve of reduced glutathione to counteract the deleterious effects of elevated ROS.
- CD14 expression is known to increase as a result of LPS challenge (Zamani, Zare Shahneh, Aghebati-Maleki & Baradaran, 2013), if following repeated exposure of the cells to 3TC causes a basal increase of CD14 expression, this may potentially impact subsequent exposure of cells to LPS or other pathogens.
- CD40 is upregulated on activated DCs (Ma & Clark, 2009), a decreased expression of CD40 suggests that both FTC and 3TC may have impacted the MUTZ-3 cells ability to respond to DC-specific positive controls. This could potentially imply that repeated exposure could cause a reduced ability of the bodies DCs to fight off immunological challenges.
- CD274, also known as programmed death ligand 1 (PD-L1), plays a role in controlling T-cell responses via the receptor PD-1 (Hudson, Cross, Jordan-Mahy & Leyland, 2020), this again poses the question whether repeated exposure may prevent the immune system from carrying out its normal roles.
- CD69 is expressed at the early stages on activated T cells, as previously discussed the increased basal activation levels of the 3TC-cultured cells may also prevent appropriate immune responses.
- CD63, CD203c and CD164 are all markers of basophil activation, the changes in these markers at basal levels and following exposure to known activators may play an important role in allergic responses following repeated exposure and should be explored further.
- These results have, potential, consequences for long-acting formulations and implants as they show possible effects of repeat exposure to antiretrovirals that may be used in such preparations.

References

Chandiwana NC, Serenata CM, Owen A, Rannard S, Pérez Casas C, Scott C, *et al.* (2021). Impact of long-acting therapies on the global HIV epidemic. AIDS 35.

Hudson K, Cross N, Jordan-Mahy N, & Leyland R (2020). The Extrinsic and Intrinsic Roles of PD-L1 and Its Receptor PD-1: Implications for Immunotherapy Treatment. Frontiers in Immunology 11.

Ma DY, & Clark EA (2009). The role of CD40 and CD154/CD40L in dendritic cells. Semin Immunol 21: 265-272.

Ruelas Debbie S, & Greene Warner C (2013). An Integrated Overview of HIV-1 Latency. Cell 155: 519-529.

Zamani F, Zare Shahneh F, Aghebati-Maleki L, & Baradaran B (2013). Induction of CD14 Expression and Differentiation to Monocytes or Mature Macrophages in Promyelocytic Cell Lines: New Approach. Adv Pharm Bull 3: 329-332.

Interaction of nanocarriers with anti-PEG antibodies

MAX PLANCK INSTITUTE FOR POLYMER RESEARCH

Mareike Deuker, Volker Mailänder, Svenja Morsbach, Katharina Landfester
Max Planck Institute for Polymer Research, Ackermannweg 10, 55128 Mainz

INTRODUCTION

Many biomedical applications employ poly(ethylene glycol) (PEG) to reduce unspecific protein interaction and prolong the nanocarriers (NC) circulation time. Nevertheless, increasing reports demonstrate the administration of repeated doses of PEGylated NC lead to an accelerated blood clearance via anti-PEG antibodies.
The protein corona, determined by bound proteins to the NC surface, critically affects the NC's identity as recognized by cells. Accordingly, anti-PEG antibodies in the protein corona might be an important factor for the fate of the NC in vivo.

Despite the potential serious consequences of circulating anti-PEG antibodies, their influence on the effect of therapeutics and on related side effects remains an unanswered question. Therefore a detailed study of pre-existing anti-PEG antibodies in healthy individuals among the German population was performed using an enzyme linked immunosorbent assay (ELISA). To further evaluate the biological response, we investigated the enrichment of anti-PEG antibodies in the protein corona of PEGylated silica nanocapsules (SiNC). Additionally, the cellular uptake of PEGylated NC with varying amounts of bound anti-PEG antibodies was monitored.

1. PLASMA SCREENING

Plasma screening to analyse anti-PEG antibody concentration and prevalence in a sample of the German population (n = 500)

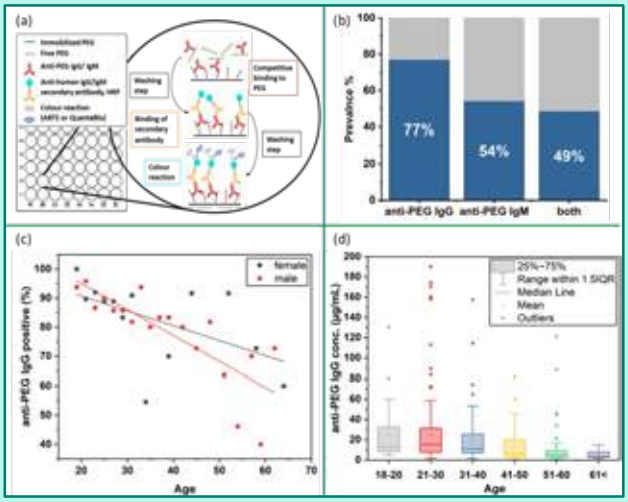

(a) Schematic setup of the ELISA.
(b) Prevalence of anti-PEG IgG antibodies (grey: all samples (100%) blue: anti-PEG antibody positive samples)
(c) Distribution of anti-PEG IgG positive samples with age (grouping of 10 ≤ samples per data point)
(d) Concentration of anti-PEG IgG antibodies in age groups.

2. PROTEIN CORONA

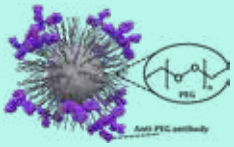

The protein corona is the biological coating of the NC that creates its biological identity as recognized by cells. The accumulation of anti-PEG antibodies in the protein corona can be analysed via LC-MS and ELISA.

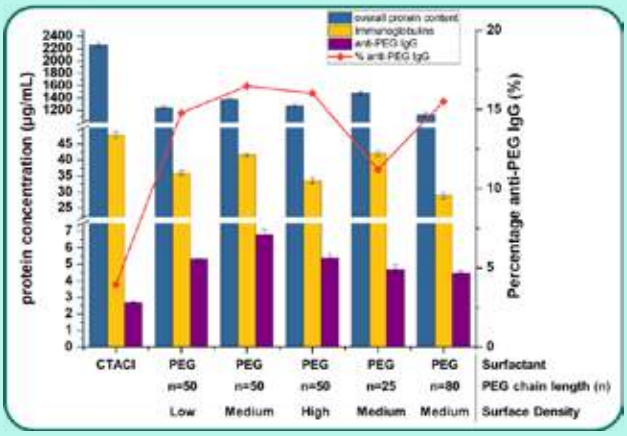

Anti-PEG IgG concentration in the protein corona of different SINC compared to overall protein and immunoglobulin content:
- Without PEG (CTACl as surfactant)
- Increasing PEG density (Low, Medium, High)
- Increasing PEG length (n=25 to 80)

3. CELL UPTAKE

Cell uptake of SINC with different amount of anti-PEG IgG in the protein corona

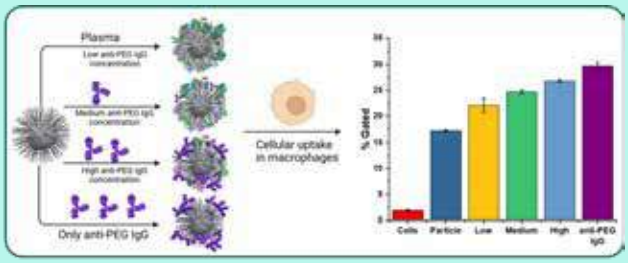

Protein corona composed of plasma proteins with increasing anti-PEG IgG concentration and only anti-PEG IgG.
Uptake in RAW 264.7 after incubation for 2h at 37°C.

CONCLUSION

1. High amount of anti-PEG IgG and IgM throughout the samples.
   - Notably, the concentration and prevalence decreased with increasing age.
2. Enrichment of anti-PEG antibodies in the protein corona of PEGylated NC compared to non-PEGylated NC.
3. Cell uptake in macrophages increased with the anti-PEG antibody concentration in the protein corona.

The existence and concentration of anti-PEG antibodies in the protein corona of different (PEGylated and non-PEGylated) NC should be further evaluated to determine the potential effects *in vivo*.

SFB 1066

POLYMERIC SQUARED MICROPLATES AS A NEW TOOL FOR THE LOCAL TREATMENT OF POST-TRAUMATIC OSTEOARTHRITIS

Martina Di Francesco[a], Sean K. Bedingfield[b], Juan M. Colazo[b], Valentina Di Francesco[a], Fang Yu[b], Miguel Ferreira[a], Daniele Di Mascolo[a], Craig Duvall[b], Paolo Decuzzi[a].

[a] Laboratory of Nanotechnology for Precision Medicine, Italian Institute of Technology – Genoa (IT)
[B] Department of Biomedical Engineering, Vanderbilt University, Nashville, TN 37235, United States.

Presenting poster: martina.difrancesco@iit.it

INTRODUCTION

Osteoarthritis (OA) is a chronic disabling disease that affects people of all age around the world. It is caused by the combination of biomechanical factors and genetic predisposition, resulting in substantial pain, function loss and, eventually, permanent disability. So far, therapeutic strategies clinically available help to alleviate symptoms and enhance temporarily joint mobility and function, without reverting OA progression itself [1]. Within this framework, a top-down strategy (**Fig.1A**) was applied for developing microsized square -poly (D,L-lactide-co-glycolide) (PLGA) microPlates (µPLs) for local, slow and continuous releases of small anti-inflammatory molecules or nanoparticles loaded themselves with drugs. Dexamethasone (DEX)[2] and matrix metalloproteinase 13 (MMP-13) RNA interference nanoparticles (siMMP13-NPs)[3] were selected as payloads and two different formulations were developed. After investigating physical-chemical, mechanical and pharmacological properties of both formulations, their therapeutic efficacy was proven *in vivo* in a mechanically-induced OA mouse model (PTOA).

µPLs SYNTHESIS AND CHARACTERIZATION

µPLs, synthetized using 15 mg of PLGA, displayed a squared shape with a length of 20 µm and a height of 10 µm (**Fig. 1B** and **C**) Mechanically speaking, they showed an apparent Young's modulus of ~ 3 MPa, similar to that of cartilage, and a high damping capability (tan δ= 0.3) (**Fig. 1D** and **E**). Also, both developed formulations demonstrated a good drug loading and a sustained and continuous drug or particles release in biologically relevant volumes, still preserving their pharmacological activity.

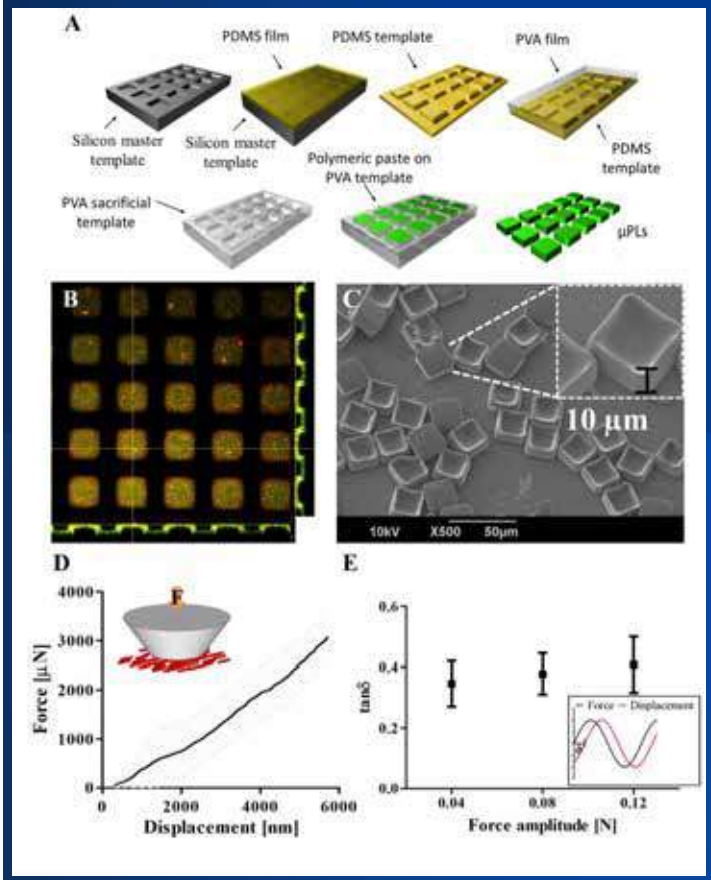

Fig 1. PLGA microPlates (µPLs) physico-chemical and mechanical characterization. **A.** Sequential replica molding steps, starting from a silicon template, passing through a PDMS and finally obtaining the PVA layer that is loaded with the polymeric paste to generate µPLs . **B.** Confocal microscopy image of the PVA template containing Cy5-siNPs (red) dispersed within PLGA paste. **C.** SEM images of the µPLs released from the PVA template. **D.** Force-displacement curve for a flat punch indentation experiment on an ensemble of µPLs (average curve and standard deviation). In the inset, a schematic of the experimental setup is provided. **E.** Energy dissipation ability of µPL upon cyclic mechanical loading (frequency 5 Hz) as a function of the force oscillation amplitude. In the inset, a schematic of the testing routine is provided highlighting the phase angle δ- dissipation parameter.

IN VIVO µPLs THERAPEUTIC EFFICACY

After thorough physico-chemical and *in vitro* pharmacological characterization, the two formulations were tested *in vivo* in different OA models. As first thing µPLs retention pharmacokinetic and biodistribution in a murine overload injury model (PTOA) was evaluated. Cy5 was covalently conjugated to the surface of particles. Results showed that particles were well retained in the knee after a IA single injection for 1 month (**Fig 2**) [2].

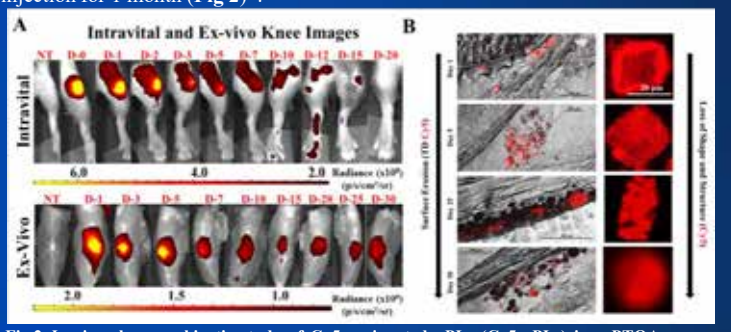

Fig.2 *In vivo* pharmacokinetic study of Cy5-conjugated µPLs (Cy5-µPLs) in a PTOA mouse model. A. Representative pharmacokinetic time course intravital images (skin on) and ex vivo knee images (skin off) of Cy5-µPLs injected intra-articularly into PTOA mouse knee. **B.** 20x Images zoomed in on Cy5-µPLs within a mouse model of PTOA at days 1, 5, 25, and 30.

Both formulations showed good results in vivo on PTOA model (**Fig. 3**). On one side, a single intra-articular (IA) injection of DEX-µPLs reduced the expression of pro-inflammatory cytokines, such as IL-1β, TNF-α, IL-6 and MMP-13. Also, they protected articular cartilage and synovial tissues from load-induced histological changes compared to Saline and DEX free groups 2 (**Fig. 3C**)[2]. While on the other, a single IA injection siMMP13-NPs loaded µPLs provided 70% of gene silencing efficiency and reduction of related inflammatory markers and damages in the same animal model (**Fig. 3D**)[3].

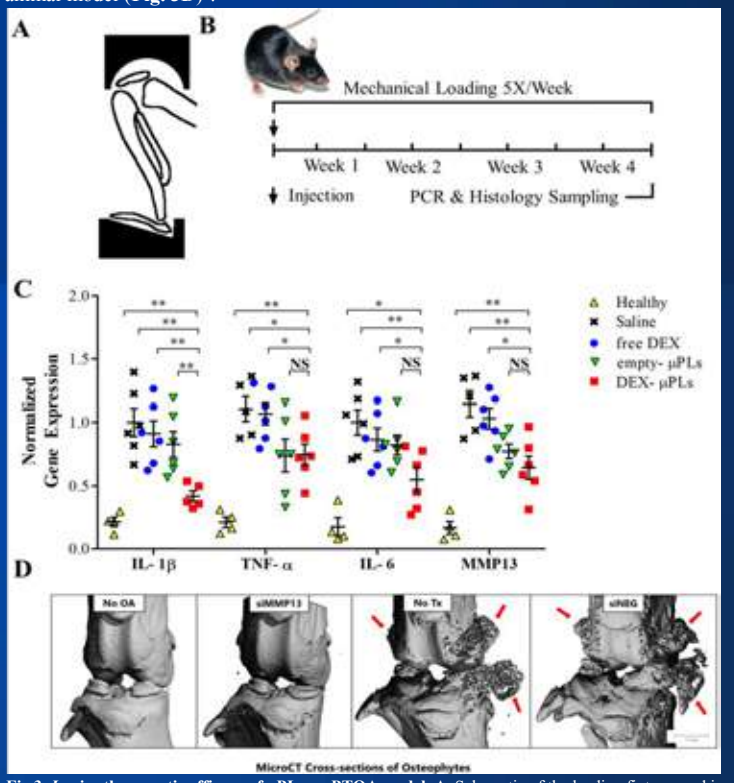

Fig 3. *In vivo* therapeutic efficacy of µPLs on PTOA model. A. Schematic of the loading fixture used in the mechanical loading of mouse knee joints to induce PTOA. B. Mechanical loading regimen. C. *in vivo* expression of IL-1β, TNF-α, IL-6, and MMP-13 after a single IA injection of DEX- µPLs measured by TaqMan qPCR. D. MicroCT analysis of ectopic mineralization and osteophyte outgrowth at 28 days after siMMP13-µPL treatment.

CONCLUSIONS

A top-down fabrication approach allowed us to realize shaped-defined µPLs that can be efficiently used as intra-articular biodegradable devices to address both inflammation and degradation in OA.

REFERENCES

[1] Martel-Pelletier et al., Osteoarthritis. Nature Reviews Disease Primers, 2016. 2(1): p. 16072.2.
[2] Di Francesco et al., ACS Applied Materials & Interfaces, 2021. 13 (27), 31379-313923.
[3] Bedingfield et al, ACS nano 15 (9), 2021.14475-14491

CLINAM
European Foundation for Clinical Nanomedicine
13th European and Global Summit for Nanomedicine

UNIVERSITÄTSmedizin. MAINZ
Department of Dermatology

MAX-PLANCK-INSTITUT FÜR POLYMERFORSCHUNG

Achieving dendritic cell subset-specific targeting *in vivo* by site-directed conjugation of targeting antibodies to nanocarriers

Michael Fichter[1,2], Johanna Simon[2], Gabor Kuhn[1], Maximilian Brückner[2], Jenny Schunke[1], Tanja Klaus[1], Richard da Costa Marques[2], Stephan Grabbe[1], Katharina Landfester[2], Volker Mailänder[1,2]

1. *Department of Dermatology, University Medical Center of the Johannes Gutenberg University Mainz*
2. *Max Planck Institute for Polymer Research Mainz*

Introduction

The major challenge of nanocarrier-based anti-cancer vaccination approaches is their targeted delivery of antigens and immunostimulatory agents to cells of interest, such as specific subtypes of dendritic cells (DCs), in order to induce robust antigen-specific anti-tumor responses. An undirected cell and body distribution of nanocarriers can lead to unwanted delivery to other immune cell types like macrophages reducing the vaccine efficacy. Aim of the present study was the site-directed and orientated conjugation of DC-specific antibodies onto nanocarriers and, therefore, the targeting of DC subsets *in vivo*.

Summary & Conclusion

- **Fc-specific and orientated conjugation of DC-targeting antibodies onto nanocarriers**
- **Substantial differences between *in vitro* and *in vivo* protein corona**
- **Anti-CD11c-functionalized NCs efficiently targeted pan dendritic cells in liver and spleen following intravenous injection**
- **Intravenously injected anti-CLEC9A-functionalized NCs specifically targeted conventional DCs type 1 in the spleen**

Results

1 *In vivo* protein corona formation

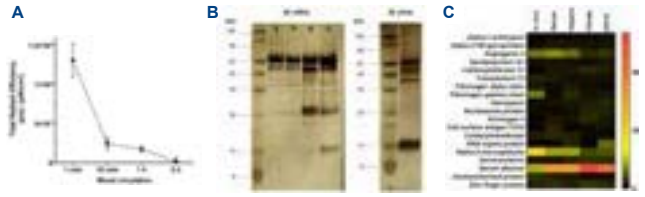

Figure 1. A) Blood circulation time of antibody-functionalized NCs. Mice were treated with mgHES-CD11c NCs or PBS as a control. At different time points blood was isolated and analyzed via the IVIS® SpectrumCT. Background fluorescence measured from PBS-treated mice was subtracted. B) SDS-PAGE of the protein corona of antibody-functionalized NCs incubated under *in vitro* conditions for 1 min (S = Serum, H = Heparin Plasma, E = EDTA Plasma, C = Citrate Plasma) or after recovery from the blood stream after 1 min (*in vivo*). C) LC-MS analysis of the protein corona of antibody-functionalized NCs.

2 *In vitro* uptake of antibody-functionalized NCs

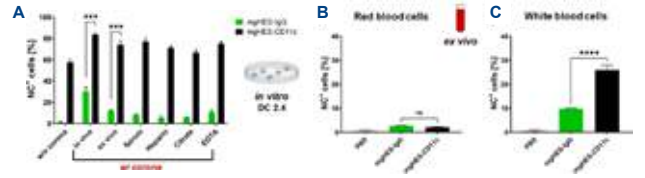

Figure 2: *In vitro* and *ex vivo* targeting properties of anti-CD11c-functionalized nanocarriers. A) DC2.4 cells were incubated with antibody-functionalized nanocarriers (37.5 µg mL^{-1}) without protein corona coating (indicated as w/o corona), after *in vivo* circulation (1 min, indicated as *in vivo* w/ corona), after *ex vivo* protein coating for 1 min (indicated as *ex vivo*), or after *in vitro* protein coating for 2 h (indicated as Serum, Heparin, Citrate, EDTA w/ corona). B+C) Interaction of whole blood components with antibody-functionalized nanocarriers. The whole blood was analyzed via flow cytometry and the interaction of antibody-functionalized nanocarriers with red blood cells (B) and white blood cells (C) was measured using flow cytometry.

3 Fluorescence *in vivo* imaging

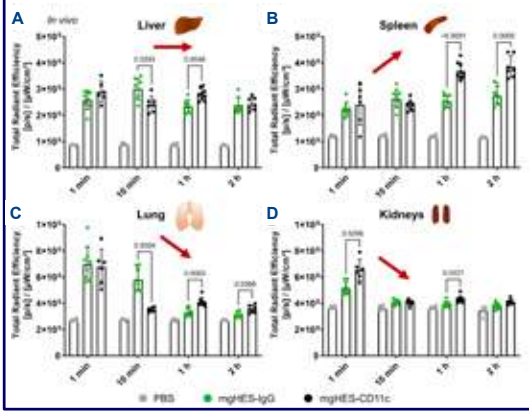

Figure 3: Biodistribution of antibody-functionalized mgHES nanocarriers into different organs over time. A-D) Animals were intravenously injected with mgHES-IgG or mgHES-CD11c nanocarriers (1 mg). Liver (A), spleen (B), lung (C), and kidneys (D) were dissected at different time points post injection (1 min – 2 h) and imaged using the IVIS® SpectrumCT.

4 Targeting of CD11c⁺ dendritic cells

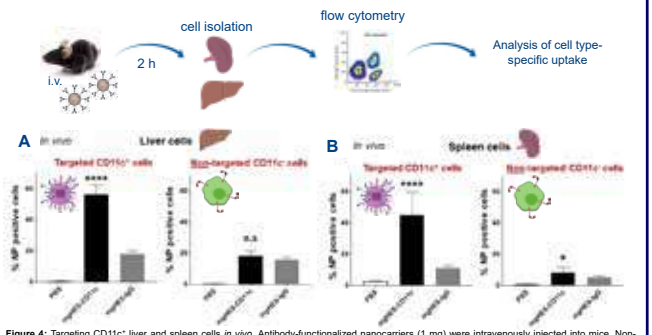

Figure 4: Targeting CD11c⁺ liver and spleen cells *in vivo*. Antibody-functionalized nanocarriers (1 mg) were intravenously injected into mice. Non-parenchymal liver cells (A) were isolated 2 h and splenocytes (B) 1 min after injection and nanocarrier uptake by CD11c⁺ or CD11c⁻ cells was analyzed using flow cytometry.

5 Targeting of DC subsets *in vivo*

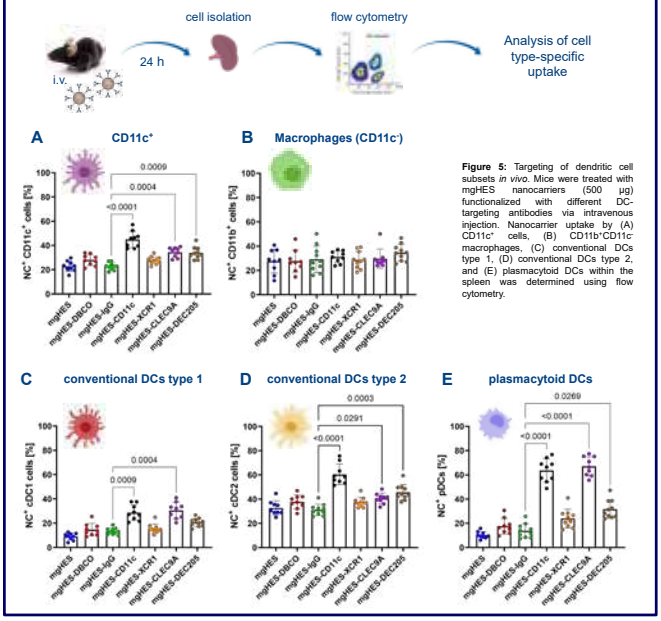

Figure 5: Targeting of dendritic cell subsets *in vivo*. Mice were treated with mgHES nanocarriers (500 µg) functionalized with different DC-targeting antibodies via intravenous injection. Nanocarrier uptake by (A) CD11c⁺ cells, (B) CD11b⁺CD11c⁻ macrophages, (C) conventional DCs type 1, (D) conventional DCs type 2, and (E) plasmacytoid DCs within the spleen was determined using flow cytometry.

Methods

Site-specific antibody conjugation

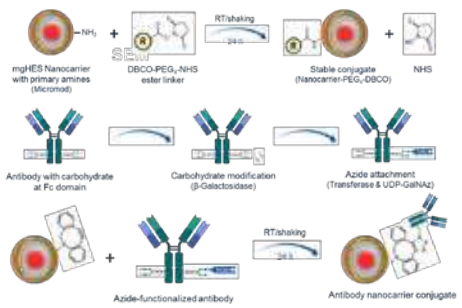

***In vivo* protein corona.** NCs were recovered from the blood stream 1, 10, 60, or 120 min after intravenous injection via cardiac puncture followed by magnetic separation and washed with PBS (3x) to remove loosely bound and unbound proteins. The firmly attached proteins were desorbed from the surface using 2% SDS (with 62.5 mM Tris*HCl) and heated up to 95 ˚ C for 5 min. The nanocarrier pellet was magnetically separated and the resulting protein supernatant was analyzed by Pierce Assay, SDS-PAGE, and LC-MS.

***In vitro* uptake studies.** DC2.4 cells were incubated in the presence of NCs for 2 h. Nanocarriers left untreated, pre-treated with mouse serum/plasma or isolated after *in vivo* intravenous injection were added to cells at a concentration of 37.5 µg mL^{-1} in cell culture medium w/o FBS. Cells were subsequently analyzed via flow cytometry using the Attune NxT (Thermo Fisher Scientific).

***In vivo* animal studies.** NCs were administered intravenously via tail vein injection in C57BL/6J mice and C57BL/6 albino mice. Animals were sacrificed after 2 h and all organs (lung, spleen, liver, and kidney) were prepared and imaged via IVIS® SpectrumCT. For the comparison of different DC-targeting antibodies conjugated onto the NC surfaces, mice were sacrificed 24 h after injection via cervical dislocation and spleens were dissected and dissociated for subsequent flow cytometric analyses.

SFB 1066

Funding:
This work was partially supported by the German Research Foundation within Sonderforschungsbereich 1066 (SFB 1066).

DFG

Co-delivering of Docetaxel and Curcumin using polymeric Nanoconstructs for the treatment of Neuroblastoma

Agnese Fragassi [a, b], Martina Di Francesco [a], Fabio Pastorino [c], Miguel Ferreira [a], Valentina Di Francesco [a], Annalisa Palange [a], Christian Celia [d], Luisa Di Marzio[d], Veronica Bensa [c], Mirco Ponzoni [c], Paolo Decuzzi [a]

[a] Laboratory of Nanotechnology for Precision Medicine, Fondazione Istituto Italiano di Tecnologia (IIT), via Morego 30, Genova, 16163, Italy.
[b] Department of Chemistry and Industrial Chemistry, University of Genova, 16146 Genova,
[c]ItalyLaboratory of Experimental Therapy in Oncology, Istituto Giannina Gaslini, Via G. Gaslini 5, Genoa 16147, italy
[d]Department of Pharmacy, University of Chieti-Pescara "G. D'Annunzio", Via dei Vestini, Campus Universitario, Chieti 66100, Italy

Presenting poster: agnese.fragassi@iit.it

INTRODUCTION

Neuroblastoma (NB) is the most common extracranial childhood solid tumor and it accounts for 15% of deaths in pediatric tumor. It is characterized by biological and clinical heterogeneity and, despite aggressive therapies, by adverse outcomes. Also, most approved anticancer drugs are being used at maximally tolerated doses, leading to short- and long-term toxicity [1]. Nanomedicine and combination therapies provide formidable tools to address this disease while minimizing chemotherapy-associated toxicity [2].

SYNTHESIS AND CHARACTERIZATION OF SPNs

Spherical polymeric nanoconstructs (SPNs) for co-delivering Docetaxel (DTXL) and Curcumin (CURC) to NB malignant masses were developed. Both empty and drug loaded particles showed a narrow size distribution (PdI < 0.15) with an average size of about 190 nm (**Fig. 1A**). All the formulations exhibited a biphasic release profile, with almost 90% of the loaded drug being released within the first 24 hours (**Fig. 1B**).

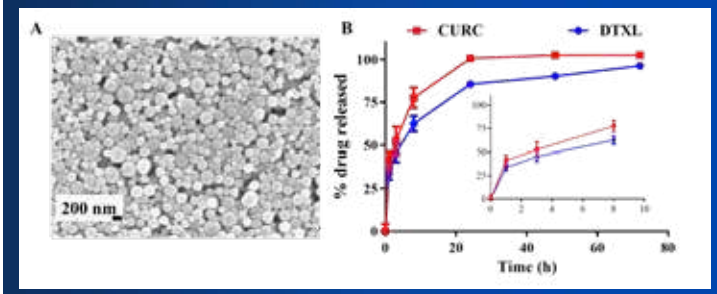

Figure 1. SPNs physico-chemical and biopharmaceutical characterization. A. Representative TEM image of empty SPN; **B**. Release profile of CURC and DTXL from CURC/DTXL-SPNs in PBS, at pH 7.4 and 37±2 °C.

IN VITRO CYTOTOXIC EFFECT OF DTXL/CURC SPNs

The potential cytotoxic effect of free CURC, free DTXL, free CURC/DTXL (1:2 mass ratio), CURC-SPNs, DTXL-SPNs and CURC/DTXL-SPNs (1:2 mass ratio) was assessed on SHSY-5Y LUC$^+$ cells (**Fig. 2**). An analysis of the IC_{50} values showed that the encapsulation of the two drugs, in combination or individually, into SPNs was generally associated with a higher cytotoxic effect. Also, the Combination Index (CI) listed in **Fig. 2C** confirmed the synergism between CURC and DTXL on SHSY-5Y LUC$^+$.

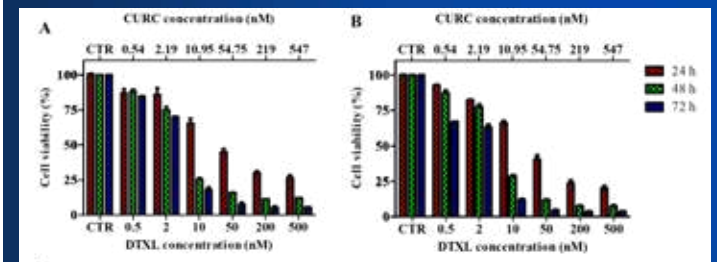

Sample	IC_{50} (nM) 24 h	48 h	72h	CI (average) 72h
DTXL	43.9 ± 8.1	11.2 ± 2.9	6.4 ± 0.9	
CURC	6168 ± 453	4169.5 ± 600.3	2989.5 ± 0.7	
DTXL-SPNs	22.6 ± 5	3.0 ± 0.3	3.2 ± 0.9	
CURC- SPNs	6517 ± 1026.7	2789 ± 158.4	1898.5 ± 215.7	
CURC/DTXL (DTXL)	42.5 ± 6.3	4.8 ± 1.1	3.4 ± 0.04	0.53
CURC/DTXL- SPNs (DTXL)	32.6 ± 13.3	4.9 ± 0.6	2.1 ± 0.1	0.65

Figure 2. *In vitro* cytotoxicity of combination of DTXL and CURC as free or loaded SPNs on SHSY-5Y LUC$^+$ cells. A. and **B.** SHSY-5Y LUC$^+$ cells viability upon incubation with different concentrations of DTXL and CURC as free or loaded SPNs, respectively. **C.** IC_{50} for DTXL, CURC and their combination free or loaded in SPNs on SHSY-5Y LUC$^+$ cells and CI values for their combinations.

IN VIVO THERAPEUTIC EFFICACY OF DTXL/CURC SPNs

After particles efficacy *in vivo* was studied in a mouse NB model. Specifically, omozygous CD1 nu/nu athymic female mice (4 to 6-weeks old) were injected with SHSY-5Y LUC$^+$ cells in the left adrenal gland. Results showed that mice treated with DTXL/CURC–SPNs had a significant increase in life span as compared to untreated mice (control) (p=0.0002), mice treated with CURC-SPNs (p=0.0205), DTXL-SPNs (p=0.0391), and free DTXL (p=0.0054) (**Fig 3**).

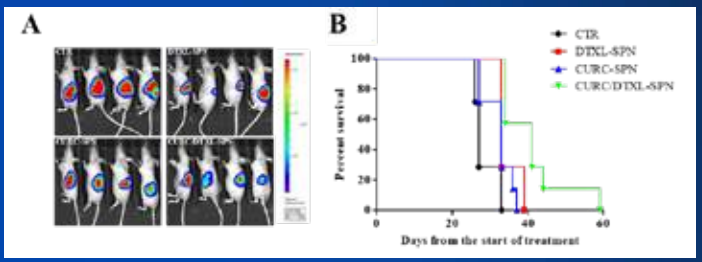

Figure 3. *In vivo* efficacy of DTXL/CURC –SPNs in NB model. A. Representative bioluminescence imaging taken 3 weeks post treatment initiation (24h post 9th administration) for the 3 nanoformulation therapeutic groups (CURC-SPNs; DTXL-SPNs; and DTXL/CURC-SPNs) and untreated control (CTR); **B.** Kaplan-Meyer survival curves with corresponding statistical analysis comparing the nanoformulation therapeutic groups with CTR and CURC/DTXL-SPN with SPN monotherapy.

MRI TUMOR IMAGING AND SPNs BIODISTRIBUTION

Particles biodistribution were investigated in the same animal model by injecting i.v. SPNs labeled with ^{64}Cu, while tumor mass progression was studied using Magnetic Resonance Imaging (MRI) (**Fig 4**). Specifically, at 8 days post tumor cell inoculation, the percentage of injected SPNs normalized by the mass of the organ (%ID/g) was equal to 45 ± 7.1% ID/g in the liver, 26 ± 7% ID/g in the spleen, and 4.9 ± 0.6% ID/g in the kidneys. For the tumor, a SPNs accumulation of 2.3 ± 0.5 % ID/g was measured at day 8 post inoculation.

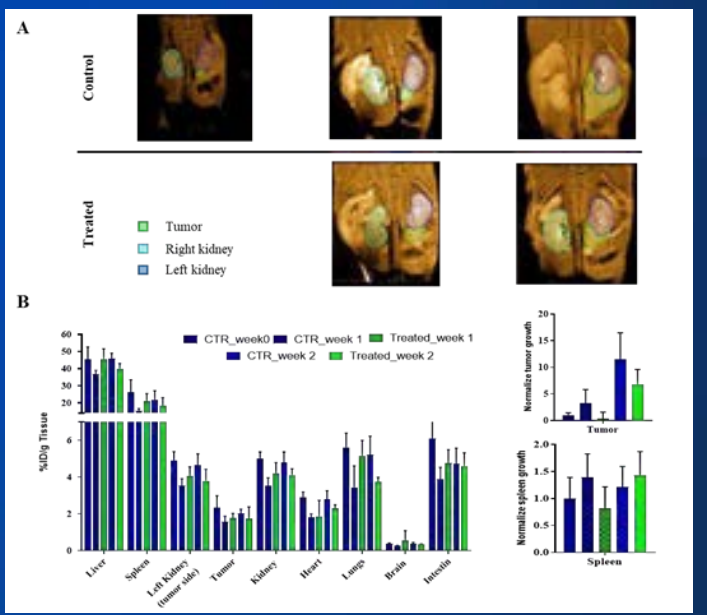

Figure 4. Tumor progression (MRI) and SPN Biodistribution analyses. A. Longitudinal tumor burden by MR imaging analysis (**left**) and ex-vivo weight measurements (**right**) (green contour: tumor; light blue contour: right kidney with tumor; dark blue contour: left kidney with no tumor). **C.** Biodistribution analysis of ^{64}Cu-SPNs at 0, 1 and 2 weeks.

CONCLUSIONS

This work demonstrated that enabling combination therapies via Nanomedicine can modulate NB progression with a significant increase in overall survival.

REFERENCES
1. Luksch, R., et al., *Neuroblastoma (Peripheral neuroblastic tumours)*. Critical reviews in oncology/hematology, 2016. **107**: p. 163-181.
2. Pastorino, F., et al., *Overcoming biological barriers in neuroblastoma therapy: the vascular targeting approach with liposomal drug nanocarriers*. Small, 2019. **15**(10): p. 1804591.

Development of a liposomal nanoformulation for the treatment of lysosomal storage diseases

Valentina Francia, Aleksandra Filippova, Scott McNeil
Laboratory of Nanopharmaceutical & Regulatory Science, Department of Pharmaceutical Sciences, University of Basel
valentina.francia@unibas.ch

AIM

Reducing the immunogenicity and increase the bioavailability of recombinant acid α-glucosidase (Myozyme) by liposomal encapsulation

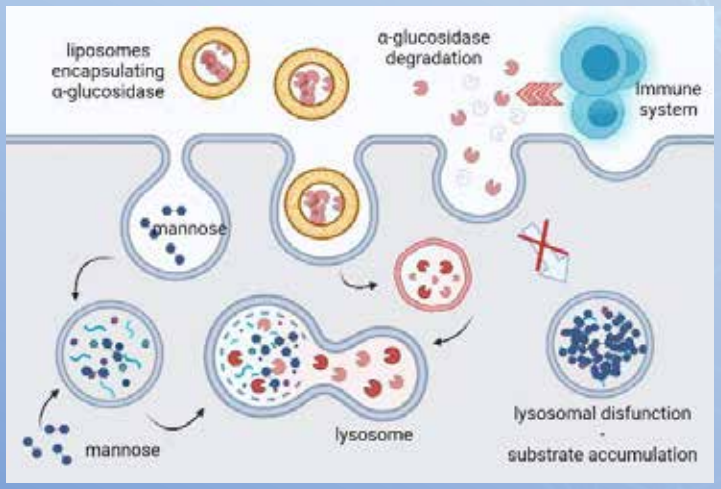

Figure 1: Pompe disease patients miss the lysosomal acid α-glucosidase. Enzyme replacement therapy with Myozyme, a recombinant α-glucosidase, revert the phenotype, but can cause severe immune reactions after repeated administrations. Encapsulation into drug delivery systems (liposomes) can decrease enzyme immunogenicity and increase its bioavailability in patients.

MATERIALS and METHODS

Figure 2: DOPC/Cholesterol/DSPE-PEG2000 liposomes are loaded with α-glucosidase and extruded. To remove the unencapsulated enzyme, fast protein liquid chromatography is performed.

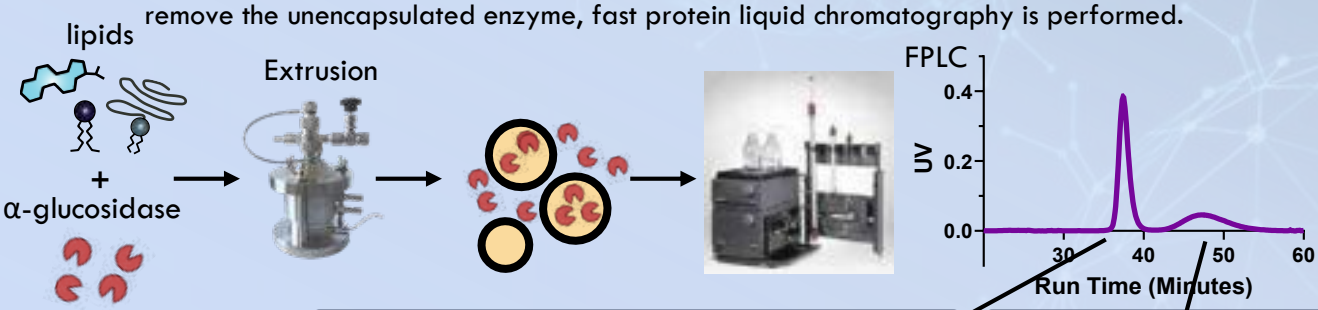

Figure 3: FPLC fractions are collected and their size measured by CryoEM and DLS

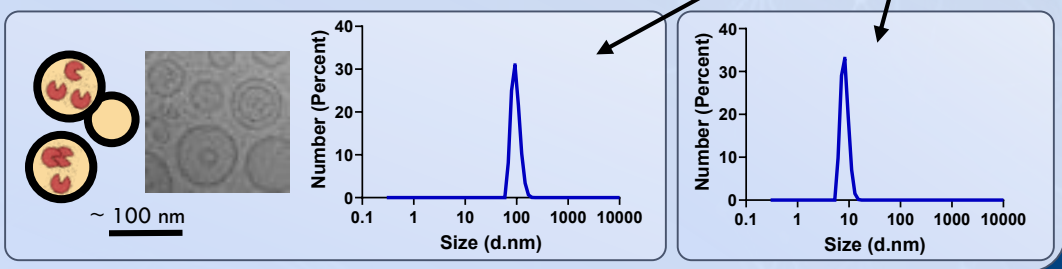

RESULTS

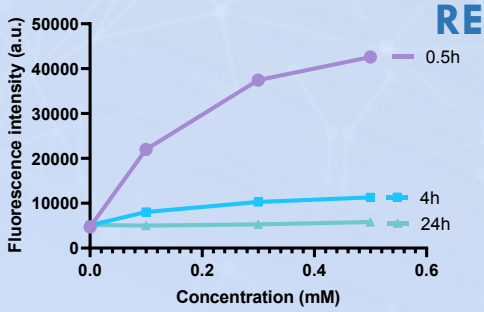

Figure 4: Dose and time-dependent uptake of the fluorescently-labelled enzyme-loaded liposomal formulation in HUVECs.

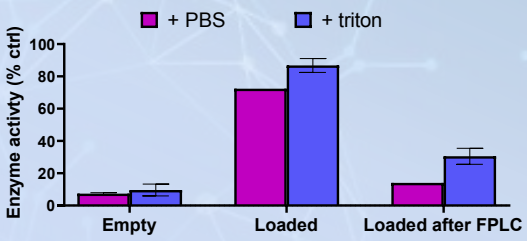

Figure 5: Enzyme activity of empty and loaded formulations. After the formulation process, the enzyme only partially retains its activity. Triton is used to break liposomes

REFERENCES

Platt, F. M., *et al.* **Lysosomal storage diseases.** Nat. Rev. Dis. Prim. 4, (2018).

Farjadian, F. *et al.* **Nanopharmaceuticals and nanomedicines currently on the market: Challenges and opportunities.** Nanomedicine vol. 14 93–126 (2019).

Lipid Nanoparticle Formulation of Niclosamide (nano NCM) Effectively Inhibits SARS-CoV-2 Replication In Vitro.

Hanmant Gaikwad, Guankui Wang, Mary K. McCarthy, Mercedes Gonzalez-Juarrero, Yue Li, Michael Armstrong, Nichole Reisdorph, Thomas E. Morrison, and Dmitri Simberg

Skaggs School of Pharmacy and Pharmaceutical Sciences, University of Colorado Denver | Anschutz Medical Campus, Aurora, CO 80045 USA.

ABSTRACT

Abstract: Niclosamide (NCM) is an old anthelminthic drug with pleiotropic pharmacological activities. NCM is almost completely insoluble in water, which limits its clinical use. We developed a cost-effective lipid nanoparticle formulation of NCM (nano NCM) using only FDA-approved excipient and demonstrated potency against SARS-CoV-2 infection in cells (Vero E6 and ACE2-expressing lung epithelium cells).

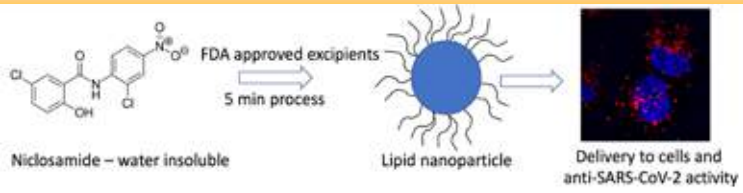

RESULTS

NCM is a class II drug with poor bioavailability, limiting its potential use. DSPE-PEG2000 (10 mM in ethanol) to the basic ethanol afforded a fully clear dispersion at 11.1 mg/mL NCM and 3.33 mM DSPE-PEG2000 (Fig. 1A, step 1, and Fig. 1B). Upon subsequent 10-fold dilution step with water (Fig. 1A, step 2), the formulation presented as clear, colloidally stable dispersion (Fig. 1B). In the final step done immediately after the dilution, the dispersion was neutralized with equinormal HCl (Fig. 1A, step 3, and Fig. 1B).

A

Step	NCM, mg/ml	DSPE-PEG2000, mM	NCM:DSPE-PEG2000 molar ratio	NCM:DSPE-PEG2000 weight ratio	Solvent composition
1. NCM solubilization	11.11	3.33	10.2:1	1.19:1	33mM NaOH; 67% EtOH
2. Dilution	1.03	0.31	10.2:1	1.19:1	31mM NaOH; 6.2% EtOH
3. Neutralization	1.00	0.30	10.2:1	1.19:1	30mM NaCl; 6% EtOH

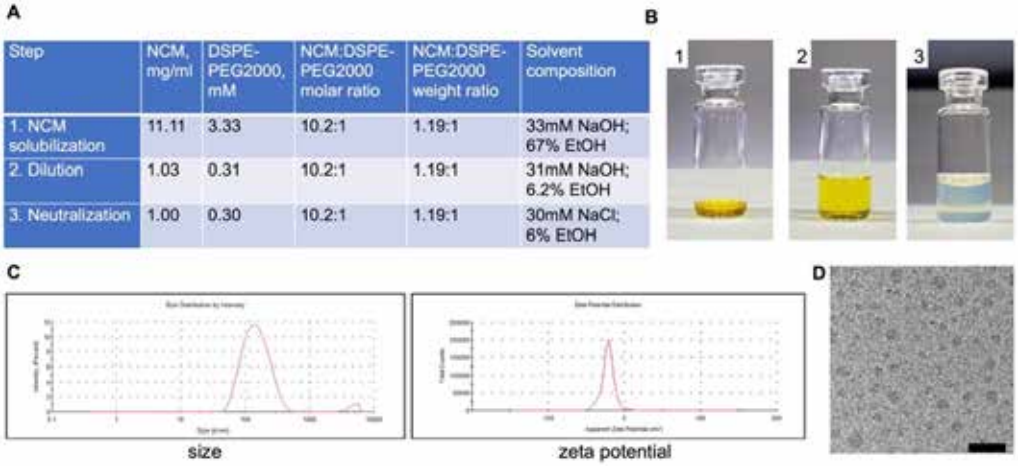

Figure 1. Nano NCM Preparation and Characterization. (**A-B**) description and appearance of formulation at each step; **C**) size and zeta potential of a representative formulation in water; **D**) negative contrast (uranyl acetate) TEM. Size bar 200nm.

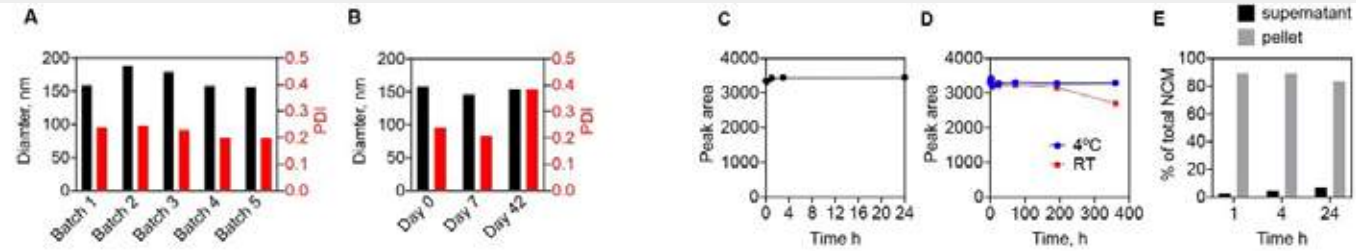

Figure 2. Stability of water-based DSPE-PEG2000 formulation (F23). A) Size reproducibility across different batches. Black bars refer to left axis, right bars refer to right axis; **B**) size stability of the formulation upon storage. Black bars refer to left axis, right bars refer to right axis; **C**) HPLC stability of the API (NCM) in basic ethanol conditions (step 1); **D**) HPLC stability of NCM in the final formulation at 4°C and room temperature (RT); **E**) HPLC assay of NCM release in the supernatant after ultracentrifugation of formulation (stored at 4°C).

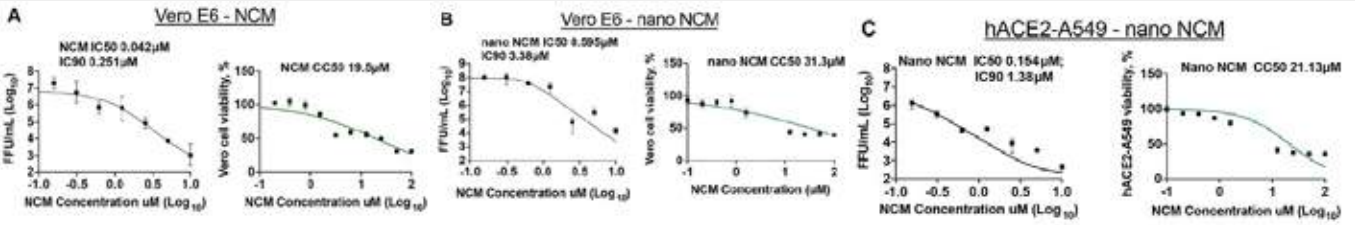

Figure 3. Efficacy and selectivity towards SARS-CoV-2 virus. A) NCM (in DMSO) effect on infection (left) and cell growth (right) in Vero E6 cells; **B**) nano NCM effect on infection (left) and cell growth (right) in Vero E6 cells; **C**) nano NCM effect on infection (left) and cell growth (right) in hACE2-A549 lung epithelial cells. N=3 technical replicates for each data point.

CONCLUSION

We developed a simple process for nano solubilization of NCM, stability, efficacy and selectivity for SARS-CoV-2 inhibition. The resulting formulation can be scaled up and tested in preclinical models and in COVID-19 patients. Niclosamide as a generic anthelmintic drug with anti-viral and anti-SARS-CoV-2 properties. Due to its lack of solubility, it will benefit from nanoformulation. There is a need in simple and cost effective formulation approaches, which is addressed in this work. https://doi.org/10.33218/001c.18813

ACKNOWLEDGEMENTS: We appreciate the funding R01CA194058, R01EB022040 and R01AI154959 from NIH

UNIVERSITÄTS KLINIKUM Jena

Selective uptake into inflamed human intestinal tissue and immune cell targeting by wormlike polymer micelles

Elena Gardey[1,3], Fabian Sobotta[2,3], Johannes C. Brendel[2,3], Andreas Stallmach[1,3]

[1] Clinic of Internal Medicine IV (GHI) University Hospital Jena
[2] Advanced Polymer Synthesis Group (APS) Friedrich Schiller University Jena
[3] Jena Center for Soft Matter (JCSM), Friedrich Schiller University Jena

The limited efficacy and potentially severe side effects associated with the use of systemic anti-inflammatory drugs call for new approaches in the therapy of inflammatory bowel disease (IBD). Selective targeting of inflamed areas in the gastrointestinal tract with local drug release could be an effective treatment that avoids adverse effects. Our studies show that the shape of polymeric nanoparticles (micelles) represents a key to the necessary tissue selectivity in the colon that has received so far little attention. Using human colon biopsies in ex vivo experiments, we demonstrated that wormlike micelles (filomicelles) with a dense poly(ethylene oxide) (Fig. 1) shell composition selectively penetrate inflamed human mucosa without showing significant interactions with healthy tissue. Similarly shaped small spherical micelles (~25 nm) rapidly cross the epithelial barrier but without the necessary selectivity for the inflamed mucosa of patients with IBD. In contrast, large vesicles (~120 nm) are hardly taken up (Fig. 2). We demonstrated that after crossing the gastrointestinal barrier, the wormlike nanoparticles localize in immune cells of the lamina propria (Fig. 3,4).

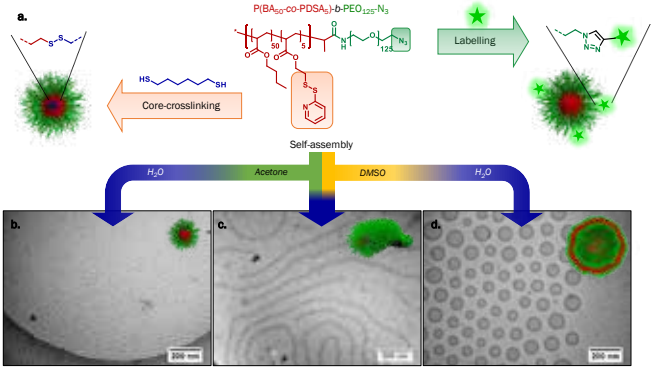

Figure 1. Preparation of core-crosslinked polymeric nanostructures with different shapes based on the same polymer. a) Schematic representation of the solvent switch approach to generate nanostructures of different morphology including subsequent core-crosslinking and labeling steps. b) cryo-TEM image of spheres prepared with acetone as co-solvent after crosslinking and labeling. c) cryo-TEM of worm-like micelles prepared with DMSO/acetone as co-solvent after crosslinking and labeling. d) cryo-TEM of vesicles with DMSO as co-solvent after crosslinking and labeling.

Thus, the filomicelles represent an innovative carrier nanoparticle for efficient and selective targeting of inflamed areas and the main proinflammatory cells in the case of IBD. The comparatively large volume of these wormlike nanoparticles compared to spherical nanoparticles also promises a higher transport capacity of anti-inflammatory drugs to these targets, which is currently under investigation. The ability to further modify the large surface area of these nanostructures should further increase selectivity and further enhance accumulation in immune cells of the inflamed mucosa.

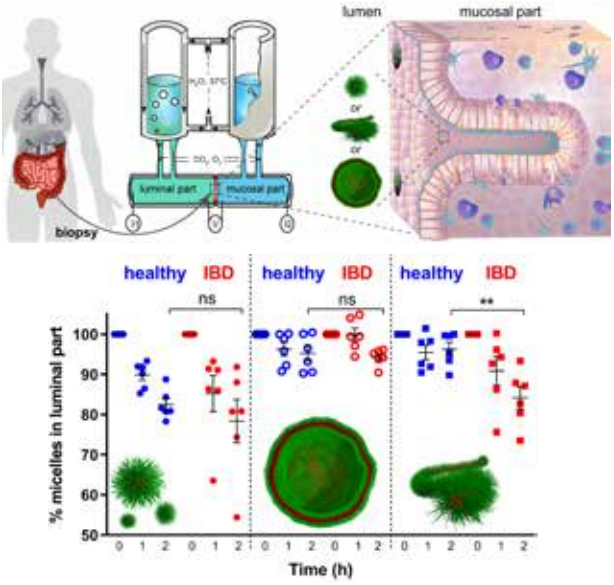

Figure 2. Uptake of spherical micelles (full dots), polymeric vesicles (empty dots) and worms (squares) in healthy (blue) and in inflamed (red) mucosa. The results (M ± SEM) are presented as the percentage of relevant concentration; $^{**}p < 0.001$, n = 6 (n – number of donors/patients). Nanoparticles were added to the mucosal part of the Ussing chambers.

The scheme of colon mucosa

Localization of micelles in human mucosa

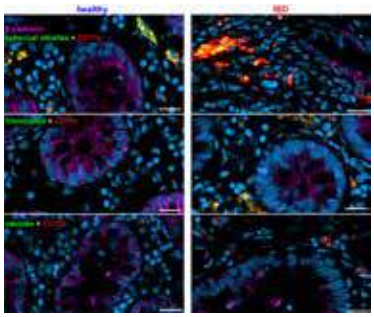

Figure 3. Localization of nanoparticles in healthy and inflamed human mucosa. Localization of spherical micelles, wormlike micelles and vesicles in human mucosa after 2 h incubation in Ussing chambers. Accumulation of micelles in immune cells of inflamed human mucosa. blue (DAPI) - nuclei; red (CD11b) - immune cells, green: nanoparticles; violet: E-cadherin (epithelium). Scale bar is 20 µm.

Time-dependent uptake of filomicelles

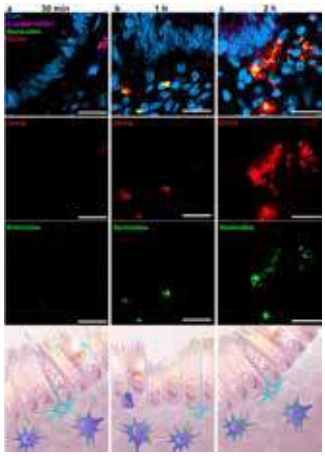

Figure 4. Uptake kinetics of wormlike micelles into inflamed human mucosa after 30 min (a), after 1 h (b) and 2 h (c) incubation in Ussing chambers. (green: nanoparticles; blue (DAPI): nuclei; violet: tight or adherens junctions in epithelium), scale bar is 20 µm.

Overall, we conclude that the structure of polymeric nanoparticles is a key factor for selective uptake in inflamed areas in the colon. We believe that our study is important for the further successful development of nanoparticle delivery systems for efficient IBD therapy.

[1] Gardey, E.; Sobotta, F.H.; Hoeppener, S.; Bruns, T.; Stallmach, A.; Brendel, J.C. *Biomacromolecules*, 2020, 21, (4), 1393-1406.

[2] Gardey, E.; Sobotta, F.H.; Haziri, D.; Grunert, P.C.; Kuchenbrod, M.T.; Gruschwitz, F.V.; Hoeppener, S.; Schumann, M.; Gaßler, N.; Stallmach, A.; Brendel, J.C.; 2021 *doi.org/10.1101/2021.01.26.428316, bioRxiv*

Liposomes - a highly efficient drug delivery system for different clinical applications

Maria Manuela Gaspar
Research Institute for Medicines, iMed.ULisboa, Faculty of Pharmacy, Universidade de Lisboa, Portugal
mgaspar@ff.ulisboa.pt

Infectious diseases

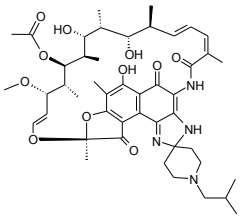

Rifabutin (RFB)
MW = 847

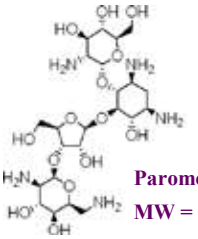

Paromomicin (PRM)
MW = 846

Therapeutic activity of RFB liposomes

***M. avium* model of infection**

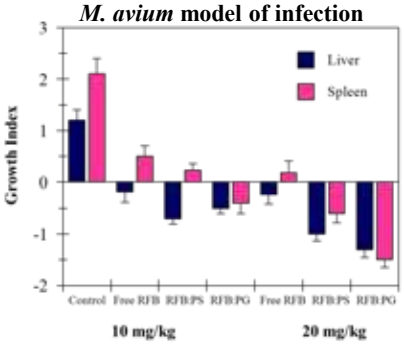

Lipid compositions: PC:PS (RFB:PS) and **PC:PG** (RFB:PG). Mice were treated at doses of 10 and 20 mg/kg of body weight i.v. 3 times a week for 3 weeks.

***M. tuberculosis* model of infection**

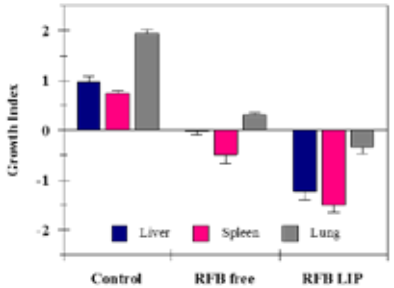

RFB in free form (Free RFB) or incorporated in DPPC:DPPG liposomes
BALB/c mice infected with *M. tuberculosis* strain H37Rv. Mice were treated at doses of 20 mg/kg of body weight i.v. 3 times a week for 2 weeks.

Gaspar MM *et al.*, (2000), Antimicrob Agents Chemother. **44**: 2424-2

Therapeutic effect of PRM liposomes *vs* Ambisome®

Parasite burden of BALB/c mice infected with *L. Infantum*
Influence of administered dose

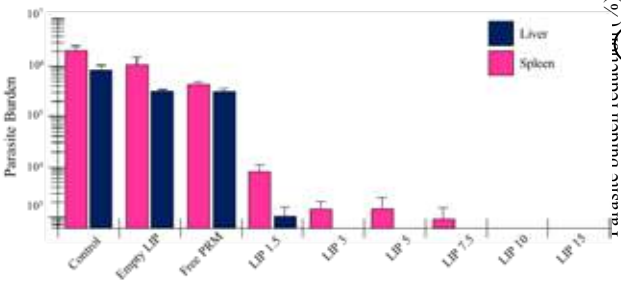

Spleen

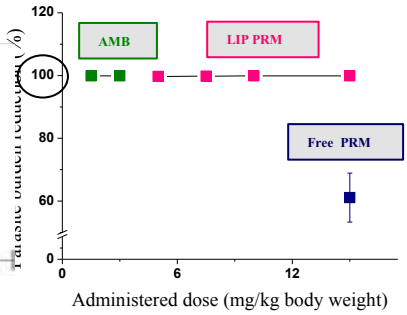

Liver

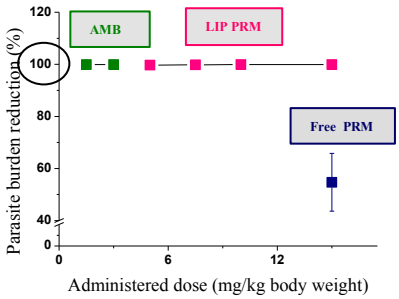

PRM Lip - LIP PRM (DPPC:DPPG) Mean size: 0.14 µm / Dose:s ranging from 1.5-15 mg/kg body weight (i.v.) / **PRM Free** – Free PPRM / Dose:15 mg/kg body weight (i.v.). (MHOM/MA/67/ITMAP-263)

Gaspar MM *et al.*, (2015), N: NBM, **11**: 1851-1860.

Cancer

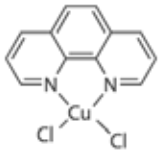

Copper Complex
MW = 315

Therapeutic effect of Cuphen liposomes in a syngeneic murine melanoma model

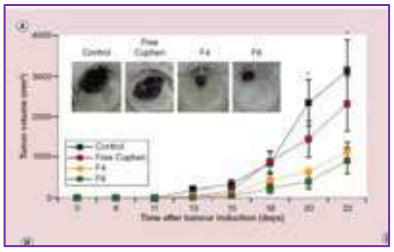

F4– DMPC:Chol:DSPE-PEG; **F6** - DMPC:CHEMS:DSPE-PEG; Mice received i.v. injections of the formulations under study at a dose of 2.5 mg/kg of body weight, three times a week, for two weeks.

Pinho J *et al*, Nanomedicine UK, 2019, 14(7):835-850.

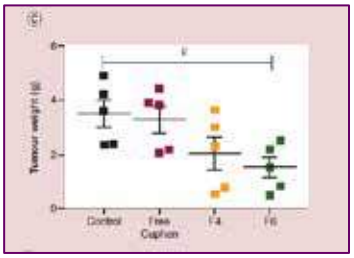

Therapeutic effect of Cuphen liposomes in a syngeneic murine colon cancer model

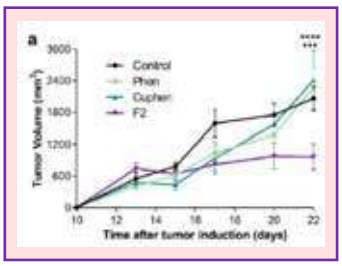

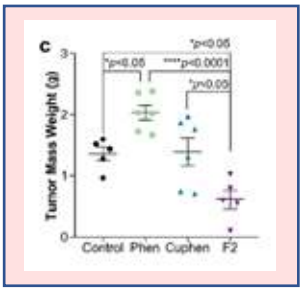

F2– DOPE:CHEMS:DMPC:DSPE-PEG; Mice received i.v. injections of the formulations under study at a dose of 2.5 mg/kg of body weight, three times a week, for two weeks.

Antiproliferative effect of Cuphen formulations towards murine melanoma and colon cancer cell lines (IC_{50} µM)

Formulation	B16F10	CT-26
Free Cuphen	3.4 ± 0.6	2.2 ± 0.1
LIP Cuphen **(F4)**	2.1 ± 0.6	-
LIP Cuphen **(F6)**	2.7 ± 0.9	-
LIP Cuphen **(F2)**	-	2.7 ± 0.1

Pinho J *et al*, Int. J. Pharmaceutics, 2021, 599:120463.

RAMAN SPECTROSCOPY: IN *VIVO* APPLICATION FOR BONE EVALUATION IN ORAL SURGERY

E. Gatin[1, 2], P. Nagy[3], S.M. Iordache[4] , A.M. Iordache[4], C. Luculescu [5] , C. Berlic [1], C. Cosconel [2]

1 University of Bucharest, Faculty of Physics, Magurele – Bucharest, Romania; **2** University of Medicine "Carol Davila", Blv. Eroii Sanitari 8, Sector 5, Bucharest, Romania; **3** Semmelweiss University, Faculty of Dentistry, Periodontology Department, Budapest, Hungary; **4** Optospintronics Department, INOE 2000 Magurele, Romania; **5** INFLPR – CETAL, Magurele – Bucharest, Romania.

INTRODUCTION

The majority of studies evaluating the effects of different surgical procedures aimed at defect fill with bone grafts and only employed clinical outcome measures, such as probing pocket depth, probing attachment level, radiological analysis and direct visualization, following surgical re-entry procedures. Such approaches did not facilitate the determination of true bone quality or regeneration, an outcome that requires histologic investigation.

OBJECTIVE

A non-invasive and quick method for the evaluation of chemical compounds from bone tissues is requested. We suggest a new method, based on the Raman spectroscopy. This non destructive optical method is able toevaluate the quality of the bone, revealing the different phases for calcified tissues independent of the medical history of the patient in relation to periodontitis by means of *in vivo* Raman spectroscopy.[1, 2, 3]

Materials and Methods

Regarding our study, a group of ten patients was involved to our study after a clinical evaluation. The classification was performed according their medical status (healthy, history periodontitis and periodontitis. Investigation mainly was performed by RAMAN technique, first in vivo and then in vitro for the harvested bone samples. Raman results were back supported by SEM and EDX investigation. [1, 2, 3]

Results

Differences in peaks intensity on raw spectra (both vivo and vitro) reflect the differences in the quantities of the chemical components (related to specimens concentration) for the investigated specimens. Sensitive information obtained from the Raman spectra (peak intensities, shape related to fluorescence) using raw data, were then compared with those data obtained from SEM and EDX investigation methods. [2,3]

Regarding patients' bone samples, higher PPi peak intensities were obtained for periodontitis patiens balanced with a higher peak for immature bone. This rate was used for PCA analyse and obtaining a good correlation with the clinical observations. A medium value was obtained for healthy and with periodontitis history patients. PPi is known acting as a potent inhibitor of HAP crystals precipitation (biological mineralization), aspect that might causes periodontal disease. The rate of PPi / HAP phases (mature / immature bone) can be a marker for bone quality cuantification. [2,3]

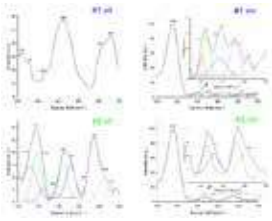

Fig. 1 Raman spectra for bone, patients #1 and #2. Details: in vitro and in vivo. **[3]**

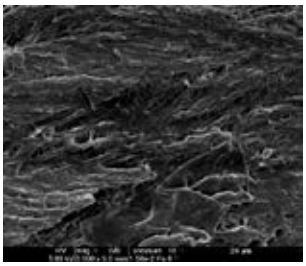

Fig.2 SEM micrograph patient #1**. [3]**

TABLE 1. Targeted Raman shift for bone specimens, **"list of four"**.

Raman shift	Characteristics	Assignment	References
430 - 450 cm^{-1}	very strong	v_2 PO_4^{3-}	
955 - 960 cm^{-1} 955 cm^{-1} 957 cm^{-1}	very strong	**Extensive mineral immature bone;** v_1 PO_4^{3-}, P – O phase; v_1 PO_4^{3-}, extensive HPO_4^{2-}	[2,3,4]
960 – 965 cm^{-1}	very strong	**Mineral mature bone;** $v_1PO_4^{3-}$ tetrahedral internal mode.	[2,3,4,5]
1,023 cm^{-1}	strong	**PP_i ($P_2O_7^{4-}$), inorganic pyrophosphate**; symmetric P••O stretch modes of PO_3^{2-} moieties; v_S PO_3 and of P–O– P bridging.	[4, 5, 6, 7]

Conclusions

Raman technique is capable to offer a complete bone evaluation (qualitative / quantitative), in the meantime being an independent method.

References:

1) Sfeatcu R, Luculescu C, Ciobanu L, Balan A, **Gatin E**, Patrascu I. Dental Enamel Quality and Black Tooth Stain: A New Approach and Explanation by using Raman and AFM Techniques. Particulate Science and Technology 2015: 33(4): 429-435
2) **Gatin, E.;** Nagy, P.; Paun, I.; Dubok, O.; Bucur, V.; Windisch, P. **Raman spectroscopy: Application in periodontal and oral regenerative surgery for bone evaluation. *IRBM* 2019, 40(5), 279 – 285.**
3) **E. Gatin,** P. Nagy, S.M. Iordache, A.M. Iordache, C. Luculescu, **Raman Spectroscopy: *In vivo* Application for Bone Evaluation in Oral Reconstructive (Regenerative) Surgery, Diagnostics 2022, accepted, in press 2022;**
4) Nathanael AJ, Sun Ig Hong, Mangalaraj D, Pao Chi Chen. Large scale synthesis of hydroxyapatite nanospheres by high gravity method. Chemical Engineering Journal **2011**: 173: 846 – 854;
5) Daizy P, Bini LG, Aruldhas G. IR and Polarized Raman Spectra of - Na4P2O7. 10H20. Journal of Raman spectroscopy **1990**: 21: 523-524;
6) Bouchaib M, Brahim El Bali, Surendra KS, Revansidha PG. High-pressure studies of SrNi3 (P2O7)2 pyrophosphate by Raman spectroscopy and X-ray diffraction. J Mol Struct **2006**: 794:334–340;
7) Hua D, Callender R, Schramm VL, Grubmeyer C. Pyrophosphate activation in Hypoxanthine-Guanine phosphoribosyltransferase with transition state analogue. Biochemistry **2010**: 30; 49(12): 2705–2714.

Comparative analyses of gold nanorod uptake in mice brain after intranasal administration

Shunping Han, Julie Tzu-Wen Wang, Jane Sosabowski and Khuloud T. Al-Jamal

Institute of Pharmaceutical Science, Faculty of Life Sciences & Medicine, King's College London, 150 Stamford Street, London SE1 9NH, United Kingdom

Introduction and Aim

- Intranasal administration (IN) is an alternative route to access the brain non-invasively with the reduced systemic exposure of the therapeutic agent [1].
- Gold nanorods (AuNRs) demonstrate attractive optical and biological properties compared with spherical ones [2]. However, the biodistribution of AuNRs after IN administration has never been reported.
- This work aims to apply different analytical and imaging modalities to comprehensively understand the brain uptake of AuNRs which could offer insights into the potential application of AuNRs as drug delivery systems *via* the intranasal route.

Methods

Preparation of functionalized AuNRs

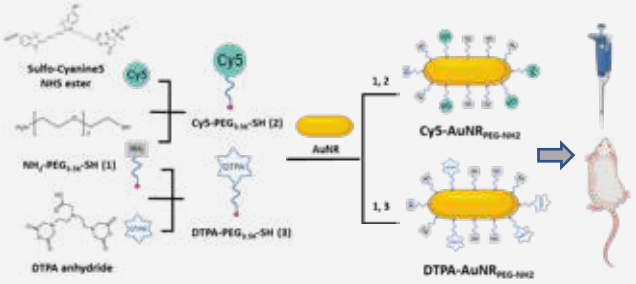

Mice were intranasally administrated with 20 µL of 300 nM AuNRs in CTS solution (0.5% CMC, 0.1% Tween 20 and 0.9% NaCl).

Characterisation of functionalised AuNRs

Hydrodynamic Diameter and Zeta Potential

Compound	Size by DLS (nm)	Zeta potential (mV)	Physical stability
$AuNR_{PEG-NH2}$	47.2 ± 1.5	42.6±0.9	+++
Cy5-$AuNR_{PEG-NH2}$	85.6 ± 14.9	24.0±0.3	+++
DTPA-$AuNR_{PEG-NH2}$	64.0 ±3.4	11.4±0.5	+++

- The functionalised AuNRs showed increased hydrodynamic size (65 – 85 nm) and decreased Zeta potential (11 - 25 mV).
- All particles showed good colloidal stability.

Mophology of the particles

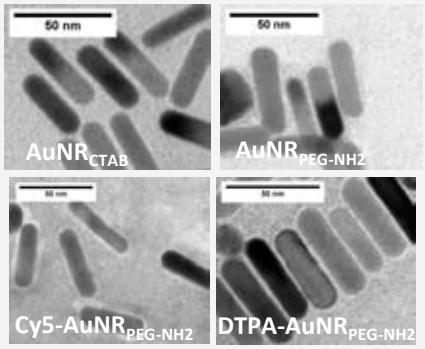

- All Particles showed monodispersed rod morphology.
- No apparent structure differences was observed after Cy5 or DTPA functionalization.

- Samples were stained with UA-Zero® for imaging.

Ref

[1] Agrawal M, Saraf S, Saraf S, et al, Journal of controlled release, 2018, 281: 139-77.
[2] Vigderman L, Khanal B P, Zubarev E R., Advanced materials, 2012, 24(36): 4811-41.

Optical Imaging

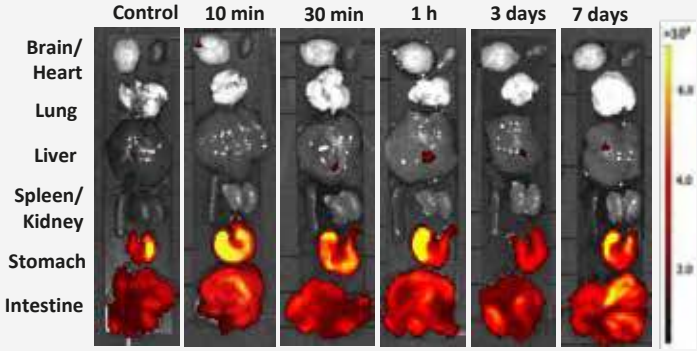

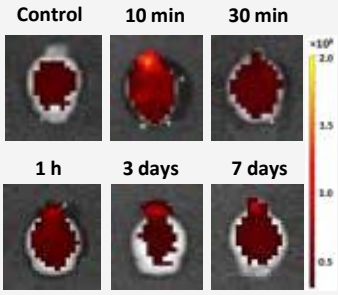

ICP-MS

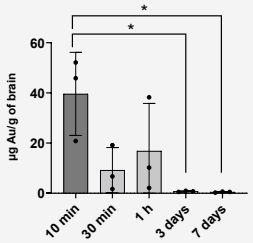

- 10 min post-administration showed the highest brain uptake

Gamma counting

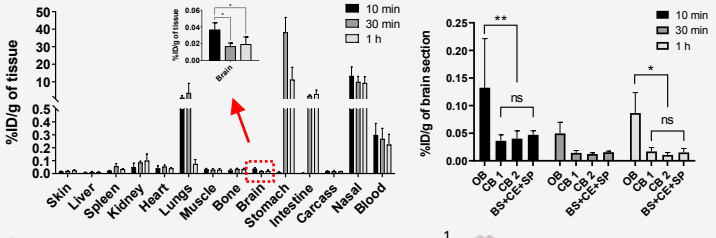

- 10 min post-administration showed the highest brain uptake. The high signal was detected in the olfactory bulbs.
- A proportion of the particles were swallowed by the mice through to the gastrointestinal tract.

1: Olfactory bulbs (OB)
2: Cerebrum 1 (CB 1)
3: Cerebrum 2 (CB 2)
4: Brain stem, cerebellum and spinal cord (BS+CE+SP)

Autoradiography

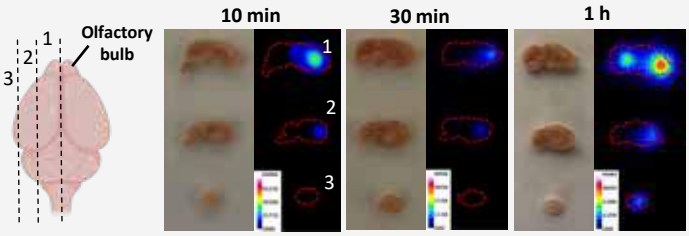

- The region-specific brain accumulation of $AuNR_s$ as a function of time.

Conclusion

- ✓ AuNRs demonstrated rapid brain uptake after intranasal administration.
- ✓ For the individual brain, olfactory bulb showed the highest signal.
- ✓ AuNRs showed a more widespread distribution to other brain regions as a function of time.

LMU LUDWIG-MAXIMILIANS-UNIVERSITÄT MÜNCHEN

ENHANCING DRUG EFFICACY WITH A HEAT-ACTIVATED DRUG-DELIVERY PLATFORM BASED ON PHOSPHATIDYL-(OLIGO)-GLYCEROL NANOCARRIER

B. S. Heiß[1], K. Zimmermann[2], R. Schmidt[1], K. Troedson[2], S. Kort[1], M. Hossann[1*], J. Hirschberger[2], T. L. ten Hagen[3], L. H. Lindner[1*]
[1] Medizinische Klinik und Poliklinik III, Klinikum Universität München - Großhadern, Munich, Germany
[2] Kleintierklinik, Ludwig-Maximilian-Universität, Munich, Germany
[3] Department of Pathology, Laboratory Experimental Oncology and Nanomedicine Innovation Center Erasmus, Rotterdam, The Netherlands
* hold founder's equity shares in Thermosome GmbH, which develops drug candidates based on phosphatidyl-oligo-glycerols. None of the other authors declare a conflict of interest.

Introduction

Liposomes are in the focus of cancer research because of their potential to effectively enhance cancer drug delivery after systemic application and greatly reduce off-site toxicity. Nevertheless, the lack of a release mechanism in traditional liposomes leads to low contents of bioavailable drug within the tumor and therefore limiting therapeutic efficacy [1]. In order to circumvent this, numerous groups have been investigating lipid compositions to gain stimuli-responsiveness in lipid-based nanocarriers [1, 2]. Our group focusses on controlled drug release from **thermosensitive liposomes (TSL)** which rely on phosphatidyl-(oligo)-glycerols ($DPPG_n$; n = 2,3), synthetic phospholipid excipients. This **$DPPG_n$-TSL drug delivery platform** achieves rapid **heat-triggered drug release** upon **mild hyperthermia (41-43 °C; HT)** and are characterized by prolonged circulation half-life in plasma and ultra-fast drug release in the heated tissue after systemic injection. The presented study focuses on exploring intravenously (i.v.) injected **Doxorubicin** (DOX) loaded $DPPG_n$-TSL in combination with regional Hyperthermia (RHT) in two different **pre-clinical settings**: the **rodent sarcoma model BN175** and the **spontaneous Fibrosarcoma in feline patients** [3].

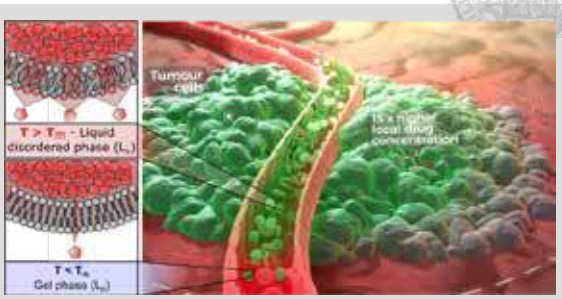

Figure 1. Schematic representation of intravascular heat-triggered drug release from $DPPG_n$-TSL. The lipid bilayer forming the TSL membrane is defined by a specific lipid composition resulting in a characteristic phase transition temperature (T_m). At temperatures (T) above T_m, the lipids melt from solid-gel (L_β) to liquid-disordered phase state (L_d), allowing a loaded drug to escape the TSL. In contrast, drug stays encapsulated at T below T_m (e.g., physiological range).

Heat-responsiveness of $DPPG_n$-TSL *in vitro*

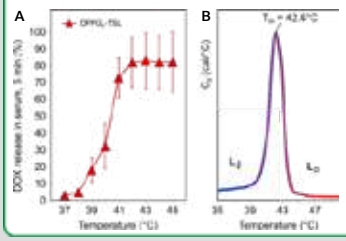

Figure 2. Temperature-dependent drug release and phase transition temperature T_m of $DPPG_n$-TSL. **(A)** Samples of $DPPG_n$-TSL-DOX were incubated at increasing temperatures (37 - 45 °C, 5 minutes) and DOX content was measured via HPLC and is shown in %. The resulting data reflect a temperature-dependent DOX release profile with stable encapsulation at 37 °C and 80 % release at temperatures above 42 °C. **(B)** T_m was determined via differential scanning calorimetry of $DPPG_n$-TSL to be 42.6 °C, proving that heat-responsiveness of TSL is defined by the specific melting temperature of the lipids [2].

10-fold increased drug concentration in heated tumor tissue in BN175 sarcoma model

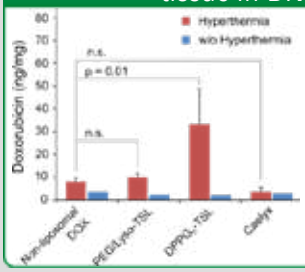

Figure 3. Drug accumulation in HT treated BN175 tumors. Male Brown Norway rats bearing two subcutaneous BN175 sarcomas on the hind legs were i.v. injected with 5 mg/kg of DOX in respective formulations (conventional DOX or different liposomal DOX formulations) at the beginning of a 60-minute regional HT treatment (41°C; red bars) of one tumor (size ~ 500 mm^3). The contralateral tumor was left unheated (physiological body temperature; blue bars). After HT treatment, DOX uptake in all tumors was measured via HPLC. For $DPPG_n$-TSL, DOX tumor concentration of heated tumor was 10-fold higher than unheated tumor and significantly higher than with conventional DOX or PEG/Lyso-TSL [3].

Intravascular heat-triggered drug release translates in local antitumor efficacy in BN175 sarcoma model

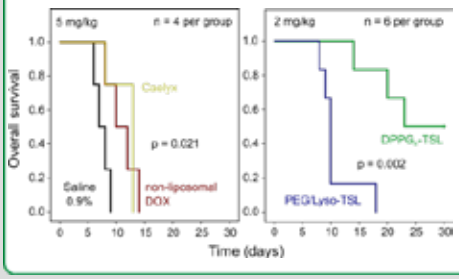

Figure 4. Efficacy study in BN175. Male Brown Norway rats bearing one subcutaneous BN175 sarcoma on the hind leg (100 mm^3) were injected i.v. with 5 or 2 mg/kg of DOX in respective formulations (conventional DOX or different liposomal DOX formulations) at the beginning of a 60-minute regional HT treatment. Kaplan-Meier survival plot of all treated animals shows prolonged survival after $DPPG_n$-TSL-DOX treatment with 2 mg/kg [3].

Efficient intravascular heat-triggered drug release *in vivo*

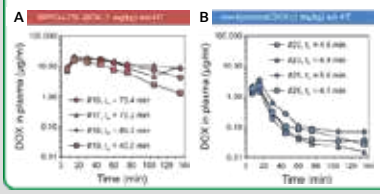

Figure 5. Pharmacokinetic profile of DOX. Anaesthetized cats were i.v. injected (15 min infusion) with 1 mg/kg of DOX in **(A)** liposomal or **(B)** free form followed by blood sampling at 7, 15, 30, 45, 60, 75, 105 and 135 minutes. DOX concentration in plasma was measured via HPLC, revealing significantly higher drug content in plasma of cats treated with $DPPG_n$-TSL-DOX as well as prolonged plasma half life ($t_{1/2}$) [3].

Significantly better metabolic response in Pet-MRI after multiple treatment of spontaneous feline Fibrosarcoma

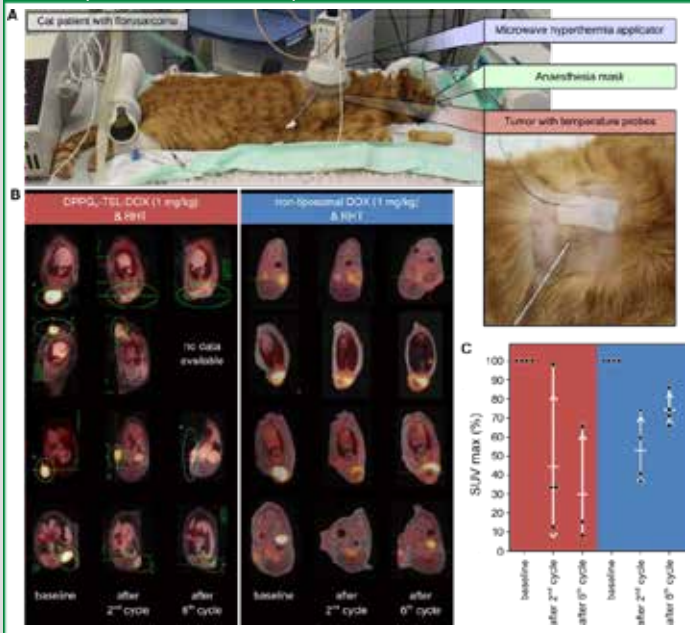

Figure 6. Neoadjuvant treatment of feline sarcoma with $DPPG_n$-TSL-DOX + RHT or conventional DOX + RHT. (A) Under general anesthesia, privately owned cats with histologically confirmed spontaneous Fibrosarcoma were infused i.v. (15 min infusion) with 1 mg/kg DOX, in either liposomal or free form, at the beginning of a 60-minute regional HT treatment (41°C, RHT) conducted with a BSD50 microwave applicator (MA-151 applicator, Sennewald Medizintechnik) and monitored with an invasive intratumoral temperature probe. Treatment was repeated six times with subsequent ^{18}FDG-PET/MRI at baseline, 2nd and 6th cycle and followed by a final chirurgic intervention (surgery). **(B)** In both groups, three out of four cats received all six cycles. Surgery was successfully conducted in 4/4 cats after $DPPG_n$-TSL-DOX treatment with histologically confirmed < 10-20 % residual vital tumor cells in resected tumors. One cat treated with conventional DOX developed lung metastasis, leaving 3/4 for surgery which revealed > 50-60 % residual vital tumor cells in histological evaluation of resected tumors. **(C)** All cats treated with $DPPG_n$-TSL-DOX achieved metabolic partial response (PR; < 30% decrease in SUVmax; PERCIST criteria) after 2nd and 6th cycle whereas cats with conventional DOX reached PR after the 2nd but showed metabolic progression after the 6th cycle [3].

Conclusion

Our $DPPG_n$-TSL based drug delivery platform succeeded in enhancing antitumoral efficacy of Doxorubicin in pre-clinical settings and has great potential for clinical application in locally advanced tumors.

References

[1] Seynhaeve A. et al., Advanced Drug Delivery Reviews, 2020. 163-164: 125-144
[2] Kneidl B. et al., International Journal of Nanomedicine, 2014. 9: 4387-4398
[3] Hossann M. et al., Advanced NanoBiomed Research, 2021. 1: 2000089

If you have further questions, please contact Bettina S. Heiß: Sonja.Muckenthaler@med.uni-muenchen.de

Acknowledgments

LMU LUDWIG-MAXIMILIANS-UNIVERSITÄT MÜNCHEN
TUM
THERMOSOME
Bundesministerium für Bildung und Forschung
DFG
Deutsche Krebshilfe
DR. SENNEWALD medizintechnik gmbh
HelmholtzZentrum münchen Deutsches Forschungszentrum für Gesundheit und Umwelt

Nottingham Trent University

MANCHESTER 1824 The University of Manchester

Mechanism Behind Selective Infiltration of Lipid Nanoparticles in the Spleen Following Ischemic Stroke

Satinderdeep Kaur[1], Laura McCulloch[2], Mohammed Abdulamaksoud[3], Dhifaf Jasim[3], Barry McColl[2]
Kostas Kostarelos[3], Stuart M. Allan[4], Zahraa S. Al-Ahmady[1,5]

[1]Department of Pharmacology, Nottingham Trent University, [2]UK Dementia Research Institute, University of Edinburgh, [3]Nanomedicine Lab and [4]Division of Neuroscience & Experimental Psychology and [5] School of Pharmacy and Optometry, Faculty of Biology, Medicine and Heath, University of Manchester, United Kingdom

satinderdeep.kaur2019@my.ntu.ac.uk; stuart.allan@manchester.ac.uk; zahraa.al-ahmady@ntu.ac.uk

Introduction

Available therapeutic approaches to manipulate the spleen mediated peripheral Immune modulation responses are not selective, and their clinical translation potential is still controversial. These repeated translational failures stresses the need for more selective technologies.

Our recent data provide the evidence that lipid nanoparticles can be selectively targeted to the spleen with more than 90% of the I.D. when administered into stroke-bearing animals. Interestingly, significantly higher uptake of liposomes by white pulp cells (WP) of the spleen was found as early as 2hrs after I.V in the stroke animals.

Aim &Hypothesis

The aim of this study is to investigate the mechanisms behind selective infiltration of liposomes into the WP of the spleen post-stroke.

Hypothesis:

We hypothesised that alterations in the splenic extracellular matrix (ECM), phagocytosis capacity and blood vessel permeability could allow the accumulation of liposomes into the splenic WP cells.

Experimental design

I. Liposome Preparation and Characterisation

A clinically-used liposomal formulation of around 100 nm in mean diameter was selected for this study.

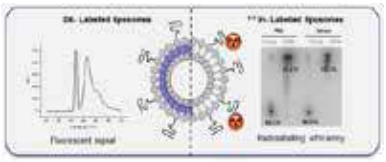

LIPOSOME CHARACTERISTICS:
Size 127 +/- 0.53 nm
Surface Charge -27 +/- 0.37mV

II. Stroke Model & Experimental Design

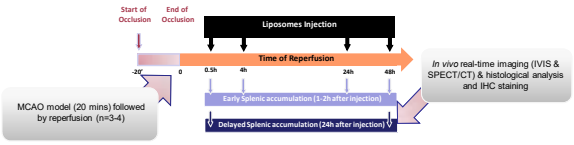

Results and discussion

I. Whole body SPECT/CT imaging of ^{111}In-Labelled liposomes (2h & 24h after I.V.)

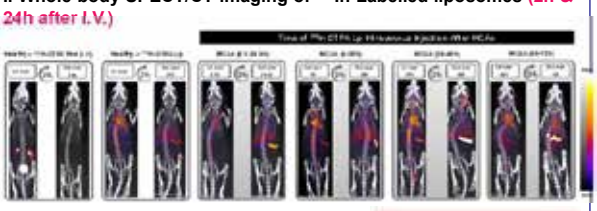

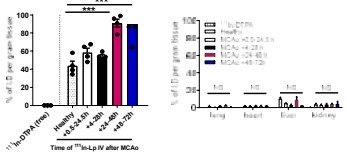

Whole body SPECT/CT imaging and quantification of liposomal accumulation into peripheral organs using ^{111}In-DTPA-liposomes indicated significant selective liposomal recruitment and accumulation into the spleen particularly when administered in the late phase post stroke (>24h)

II. Localisation of Dil-liposomes in Different Splenic compartments after Stroke (2h after I.V)

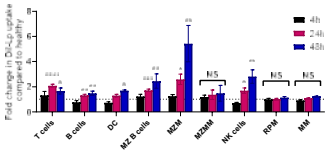

Selective liposomal infiltration into the WP and marginal zone of spleen as early as 2h after intravenous administration.

III. Structural changes in the spleen post-stroke (H &E staining and TEM Imaging)

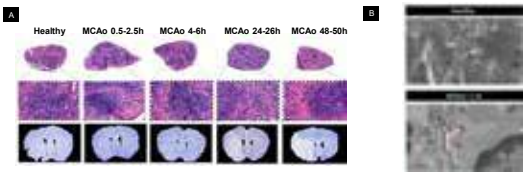

- The H&E images showed a clear reduction in the diameter of the WP and marked loss of hematopoietic elements 1-2 days after MCAo.
- Similarly, TEM images showed a clear disruption of the WP splenic conduit system suggesting a loss in ECM components.

IV. The role of ECM disruption in the selective distribution of liposomes in the spleen

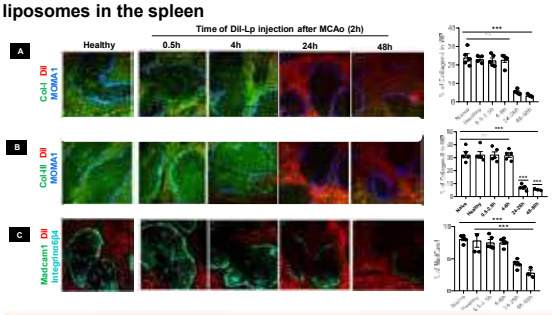

- A clear reduction in Collagen-I and Collagen-III, Integrins in the WP area of the spleen 1-2days after stroke.
- Significant reduction as Marginal zone sinus lining(Madcam1) in the WP of the spleen post-stroke.

V. Degradation of ECM and ECM remodelling of spleen post-stroke

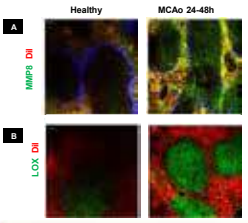

- Enhanced expression of matrix-metalloproteinases (MMP8) and ECM remodelling enzyme, lysyl oxidase (Lox) in the WP.

VI. Alterations in blood-vessel permeability and phagocytosis post-stroke

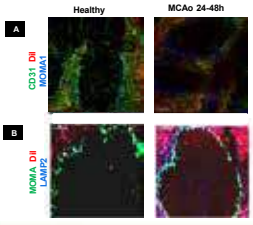

- Significant reduction in endothelial cell marker, CD31 in the WP post-stroke.
- Increase in phagocytic capacity of macrophages (LAMP2) after stroke.

Conclusions

This study highlights ***the potential of utilising liposomes as a selective tool for peripheral immunomodulation*** to accelerate the development of effective therapies for post-stroke immunological complications.

UNIVERSITÄTSmedizin. MAINZ

Nanocarrier Systems Targeting the Tumor Microenvironment: pH-Modulation and the Choice of Antibody Attachment

Joshua Krehan[1], Barbara Graefen[2], Lukas Gleue[3], Mark Helm[3], Andrea Tuettenberg[2], Andreas Walther[1]

Concept: GARP-targeting Liposomes

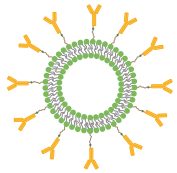

Glycoprotein A Repetition Predominant (**GARP**) is highly expressed on the surface of immunosuppressive and tumor promoting cells, such as activated Tregs[1] and numerous tumor entities, as melanoma[2] and glioblastoma.[3]

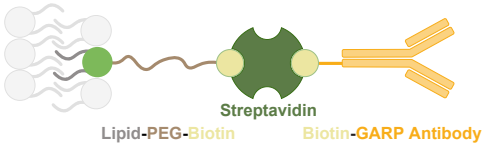

Biotin can be bound to streptavidin highly efficiently with up to four times. Biotin-linked-antibodies can thereby be attached to Lipid-PEG-Biotin containing liposomes.

Biotin Binding Efficiency

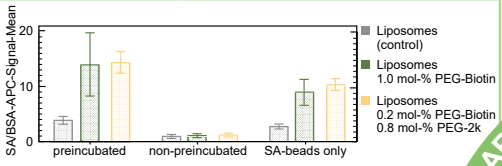

Flow cytometry confirms binding of pH-responsive liposomes, containing Lipid-PEG-Biotin, to dye-labeled streptavidin-silica-beads as a model antibody. Binding is increased by preincubation compared to non-preincubation.

Concept & Background

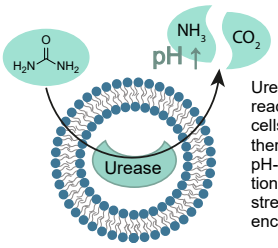

Urease catalyzes the reaction of urea (present in cells) to ammonia and can therefore be used as a pH-modulator. Rapid degradation of urease in the blood stream can be prevented by encpasulation.

Immunosuppressive tumor-associated M2 macrophages can be reprogrammed to pro-inflammatory M1 macrophages by increasing the pH value, thereby activating the innate immune system.[4,5]

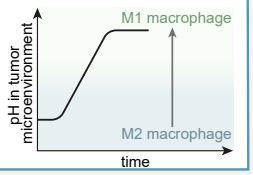

Uptake of Calcein-loaded Liposomes in MaMel-19 Cells

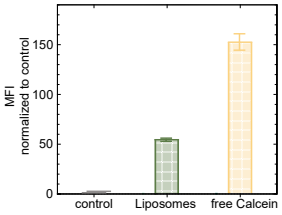

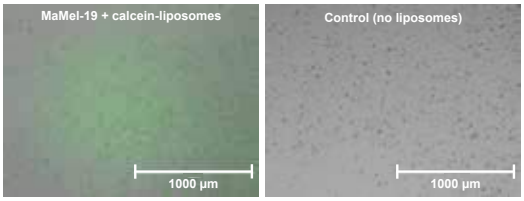

MaMel-19 cells successfully uptake calcein encapsulated into a pH-responsive liposome formulation[4].

Anti-GARP Antibody Binding Assay

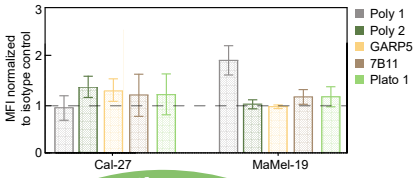

Screening of different anti-GARP antibodies in binding to GARP on human Cal-27 (epithelial tongue cancer) and MaMel-19 cells (commercially availabe).

Poly 1 shows a higher binding affinity to GARP-expressing MaMel-19.

- Streptavidin effectively binds to PEG-Biotin-functionalized lipsomes.
- MaMel-19 cells successfully uptake cargo of pH-responsive liposomes.
- Poly 1 anti-GARP antibody shows high binding efficiency to MaMel-19.

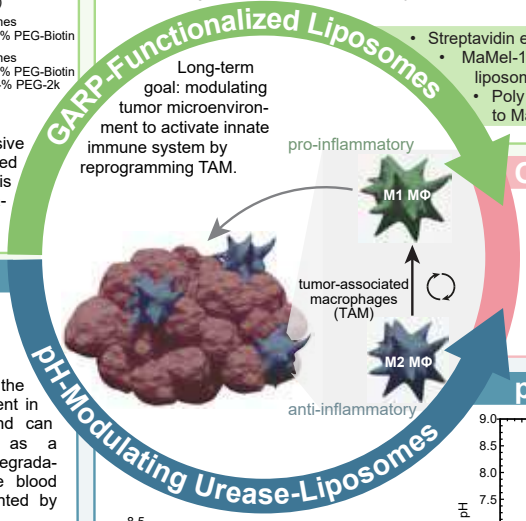

Outlook

- Repolarizing M2 macrophages by pH-modulation using urease-liposomes.
- Surface funtionalization of urease-liposomes with GARP antibodies.

pH-Modulation of Cell Medium

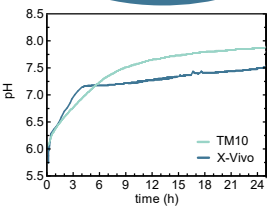

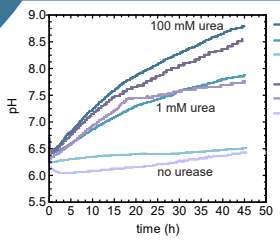

TM10, 100 mM urea
TM10, 1 mM urea
TM10, 100 mM urea, no urease
X-Vivo, 100 mM urea
X-Vivo, 1 mM urea
X-Vivo, 100 mM urea, no urease

Control: pure, unencapsulated urease increases pH of cell culture medium TM10 and X-Vivo.

Urease-liposomes effectively modulates the pH of cell culture media to a favourable physiological pH.

Liposome Formation

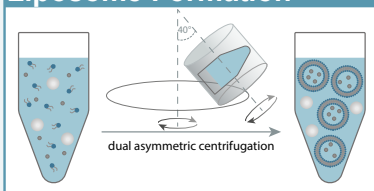

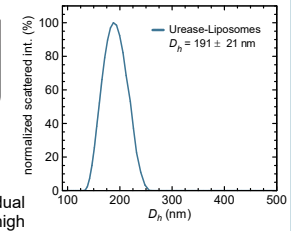

- PCR tube
- aqueous phase
- lipids
- payload
- ceramic beads

Liposome formation using dual asymmetric centrifugation: high encapsulation effciency of up to 50%, small amount of cargo required, fast, high sample number.

Permeability & pH-Modulation

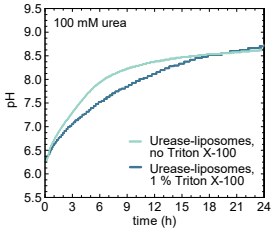

Liposomes are permeable to urea. Triton X-100 = surfactant

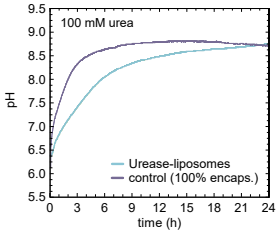

Urease-liposomes increase pH from 6.1 to 8.7 after 24 h by adding 100 mM urea.

Funding

SFB 1066

These projects have received funding by the DFG through the collaborative research center 1066, project B14N.

References

[1] H. Wang, L. Burns, *PLoS ONE* **2008**.
[2] J. Dräger, H. Hahn, *Oncotarget* **2017**, 8, 3259-3273.
[3] N. Zimmer, A. Tüttenberg, *Int. J. Mol. Sci.* **2019**, 20, 3676.
[4] C. Cui, L. Becker, *Nature Nanotechnology* **2021**, 16, 1394-1402.
[5] B. Tian, H. Cao, *Bioconjugate Chem.* **2015**, 26, 1144−1155.

Contact

[1]Department of Chemistry, Johannes Gutenberg University Mainz
[2]Department of Dermatology, University Medical Center, Johannes Gutenberg-University, Mainz
[3]Institute for Pharmaceutical and Biomedical Science, Johannes Gutenberg-University, Mainz

E-Mail: Joshua.Krehan@uni-mainz.de

www.walther-group.com

Phycocyanin sorafenib nanoformulation with enhanced oral bioavailability and anti-tumor efficacy against FLT3-ITD acute myeloid leukemia

Lekshmi G Kumar[1], Maya.S[1], Shalin C[1], Sneha James[1], Maneesh Manohar[1], Deepthymol C[1], Divya S[2], AKK Unni[2], Pavithran K[3], Shantikumar V Nair[1*], Manzoor Koyakutty[1*]

[1] Centre for Nanosciences and Molecular Medicine, Amrita Vishwa Vidyapeetham, AIMS Ponekkara Kochi, Kerala 682041, India
[2] Central Animal Lab Facility, Amrita Institute of Medical Sciences and Research Center, Ponekkara Kochi, Kerala 682041, India
[3] Department of Medical Oncology, Amrita Institute of Medical Sciences and Research Center, Ponekkara Kochi, Kerala 682041, India
[*]**Corresponding Authors:** Dr Manzoor Koyakutty and Dr Shantikumar V Nair; ***email:*** manzoork@aims.amrita.edu; shantinair@aims.amrita.edu

INTRODUCTION

Sorafenib is a small molecule oral kinase inhibitor approved for the treatment of various cancer types including Renal Cell Carcinoma (RCC) and Hepatocellular Carcinoma (HCC). The molecule was identified to inhibit FMS-like tyrosine kinase 3 specifically with internal tandem duplication mutation (*FLT3-ITD*) which is occurring in 25 to 30% of Acute Myeloid Leukemia (AML) patients. The low oral bioavailability of sorafenib due to aqueous insolubility, high rate of metabolism and limited gastrointestinal absorption, always impose the need for higher dosing frequencies which can ultimately result in toxicity burden in the patients. Nanopharmacology emerged by designing biocompatible nanocarriers so as to enhance the bioavailability, improve the therapeutic efficacy and limit the toxicity of chemodrugs. The current study focuses on the development of oral sorafenib nanomedicines using a novel protein, phycocyanin as a carrier and this protein-sorafenib nanoformulation was evaluated for its potential in the treatment of AML. The nanoformulation consist of protein sorafenib nanoparticles surface coated with mucoadhesive and mucopenetrating polymers as a result of which the PK parameters were improved compared to that of the current clinical formulation (NATCO-Tablet). The tumor volume reduction in subcutaneous xenograft AML model in NOD-SCID mice infer to the in vivo antitumor potential of this oral protein-sorafenib nanoformulation compared to that of the clinical formulation.

RESULTS

MATERIAL CHARACTERIZATION

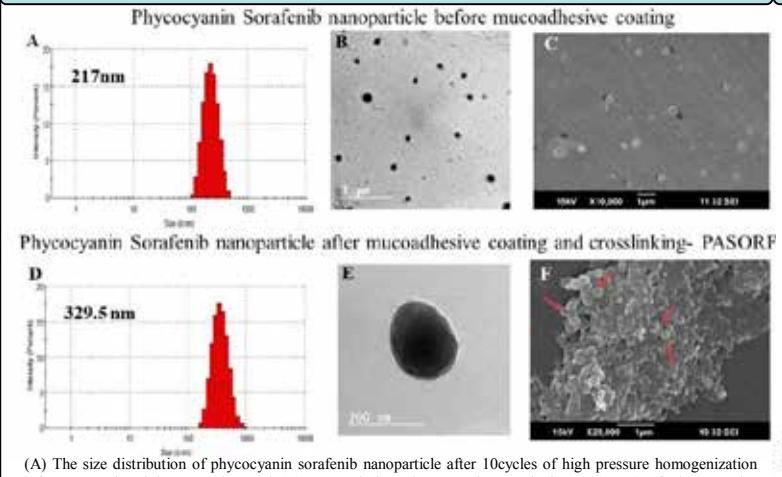

(A) The size distribution of phycocyanin sorafenib nanoparticle after 10cycles of high pressure homogenization using Dynamic Light Scattering and (B) Transmission electron microscopic image (TEM) of phycocyanin-sorafenib nanoparticle. (C) Scanning electron microscopic image (SEM) of phycocyanin-sorafenib nanoparticle. (D) The size distribution of phycocyanin-sorafenib nanoformulation-2 after coating with blend of bioavailability enhancer, mucopenetrating and release modifying polymeric layer (E) TEM image of phycocyanin sorafenib nanoformulation-2 after coating. (F) SEM of phycocyanin sorafenib nanoformulation after crosslinking (nanoparticles shown in red arrows)

BATCH-To- BATCH Reproducibility Of PASORF Oral nanoformulations

BATCH NUMBER	SIZE (nm)	ZETA POTENTIAL (mV)	Drug-ENCAPSULATION EFFICIENCY (%)	LOADING EFFICIENCY (%)
PASORF-APE-SH-160518	345	-50.1	92.5	40.1
PASORF-APE-SH-191118-02	329.5	-59.8	90.5	39.6
PASORF-APE-SH-090119	333	-55.2	97.35	42.6
PASORF-APE-SH-220319	369.7	-54.7	98.02	40.84
PASORF-APE-SH-190819	385.6	-40	94.56	48.6
AVERAGE	352.56	-51.96	94.5	42.35
SD	24.2	7.5	3.18	3.67

PHARMACOKINETIC STUDY

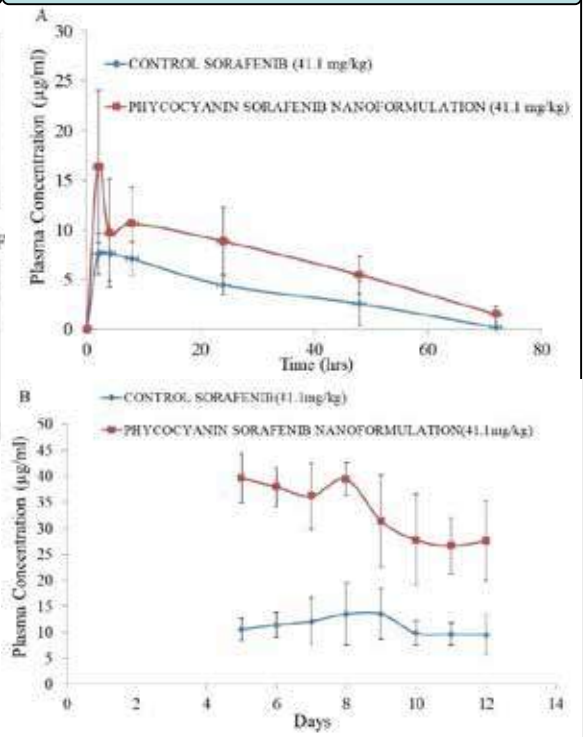

(A) Pharmacokinetics of 41.1mg/kg of phycocyanin sorafenib nanoformulation compared with control sorafenib following single oral administration in healthy SD rats. (B): Plasma concentration profile for sorafenib after continuous multiple doses of phycocyanin sorafenib nanoformulation and control sorafenib for 12 days.

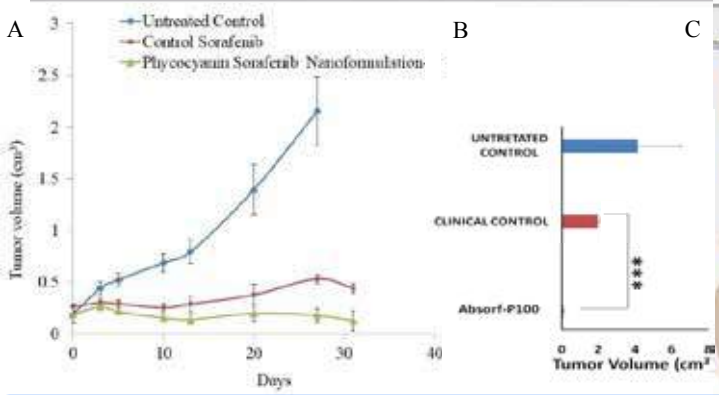

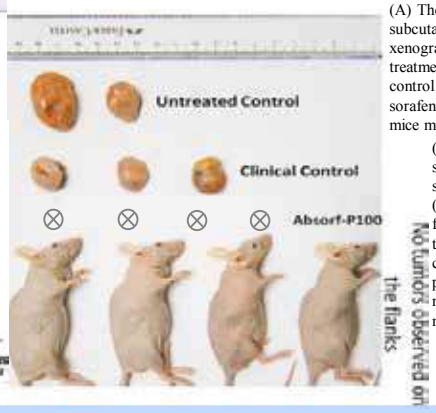

(A) The tumor reduction profile of subcutaneous AML (MV-4-11) xenografts following alternate day treatment with 41.1mg/kg of control sorafenib and phycocyanin sorafenib nanoformulation in nude mice models.

(B) Graph (C) Image showing the final day tumor size of subcutaneous AML (MV-4-11) xenografts following alternate day treatment with 41.1mg/kg of control sorafenib and phycocyanin sorafenib nanoformulation in nude mice models.

CONCLUSION

- Preparation of PASORF nanoformulations was done using scalable process of high pressure homogenization (HPH) and standardized with protein-Soraf weight ratio of 1:1 and 90% encapsulation efficiency.
- PASORF nanoformulations showed a 2-fold enhanced PK compared to clinically used sorafenib tablets (NATCO Pharmaceuticals).
- Anti tumor studies of oral protein nanoformulations in subcut AML xenograft model showed better tumor regression compared to clinical NATCO Sorafenib formulations.

REFERENCES
- Cheng AL. et.al; Efficacy and safety of sorafenib in patients in the Asia-Pacific region with advanced hepatocellular carcinoma: a phase III randomised, double-blind, placebo-controlled trial, Lancet Oncol, 10 (2009) 25-34.
- Zhu RX et. al, Epidemiology of Hepatocellular Carcinoma in the Asia-Pacific Region, Gut Liver 2016 may,10(3):332-339.
- Chhaniwal1 N, Li C, Wang J, Qiang G, Qi T, Maher H. Hepatocellular Carcinoma: Review of Current Treatment with a Focus on Transarterial Chemoembolization and Radiofrequency Ablation. Open Journal of Radiology, 2015; 5:50-58.

Acknowledgements: Department of Biotechnology (DBT), India for providing financial support under Translational Nanomedicine (Protein Nanomedicine)(Ref. No.BT/PR7665/NNT/28/658/2013).

GUT-HOMING STABLE ENZYME ACTIVITIES TO DEVELOP EFFICIENT DIGESTIVE THERAPIES

Chiem MN[1], Briand M[1], Dudal Y[1], Gaiser C[2] ,Suter-Dick L[2],Patrick Shahgaldian[2] and Laprévotte E[1]*

1 Perseo pharma AG, Hofackerstrasse 40B, CH-4132 Muttenz, Switzerland
2 FHNW, Hofackerstrasse 30, CH-4132 Muttenz, Switzerland

Introduction

Enzymes are the pillars of digestion, and responsible for the quality of nutrients ready for gastrointestinal uptake. Thus, enzymes have been developed for therapeutic purposes for those patients with faulty digestion or to control nutrient quality uptake. However, digestive diseases still represent a high unmet medical need as existing oral enzyme formulations show poor stability, susceptibility to gut conditions, lack of specific localization, and trigger variable intolerance profiles. Therefore, we have developed an oral therapeutic enzyme platform to coat the intestine with stabilized enzyme activity. The platform is made of nanoparticles in which the enzyme is shielded and fully active while remaining unexposed to the harsh gut conditions and surrounding epithelium. The nanomedicine is further functionalized to provide mucoadhesive properties and coat the intestine with stabilized enzyme activity.

1. Long lasting biocatalytic activity

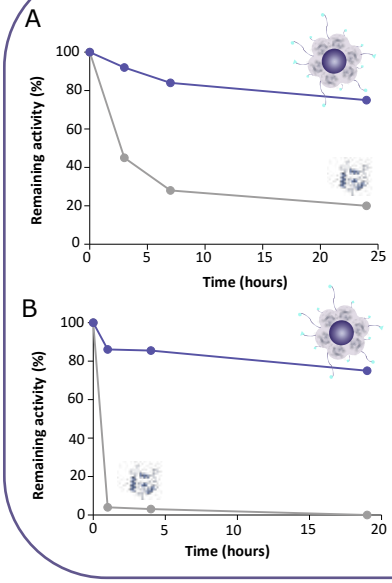

The comparison of the enzymatic activity of shielded enzyme (on the nanomedicine) and the free enzyme incubated at 37°C for 24h shows a stabilization of the biocatalytic activity on the nanomedicine **(A)**. In presence of proteases (to mimic gut stresses) the protected enzyme on the nanomedicine is not susceptible to proteolytic degradation while the free enzyme is quickly degraded **(B)**.The monitoring of the enzymatic activity points out the benefits of the protective layer of the nanomedicine to maximize the enzymatic activity in gastrointestinal conditions.

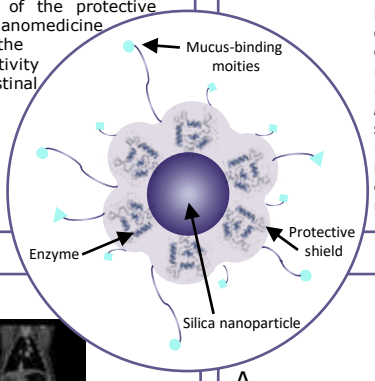

2. Mucoadhesion by design

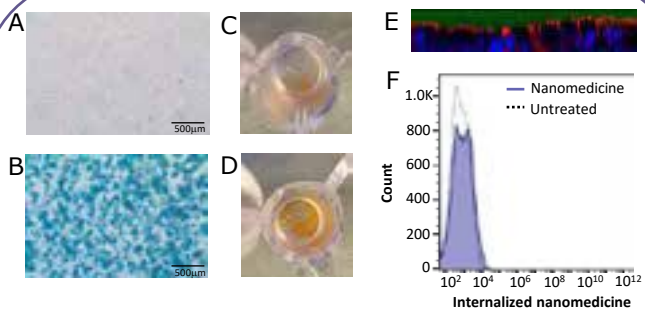

The mucus staining with Alcian Blue of two intestinal barrier models: Caco2 **(A)** and a co-culture of CaCo2 and HT29-MTX-E12 **(B)** reveals the production of mucus by the model developed with the cell co-culture **(B)**. The binding experiments of functionalized-mucus-binding nanoparticles (orange) shows an affinity of the nanomedicine for the mucus **(C-D)**. Confocal microscopy analysis *(blue: nucleus, red: cell membrane, green: nanomedicine)* confirms this affinity and shows a coating of the nanomedicine onto the intestinal barrier **(E)**. By flow cytometry, it is shown that the nanomedicine are not internalized by the intestinal epithelium **(F)**. These experiments highlights the capacity of the functionalized nanomedicine to interact with the intestinal mucus.

4. Intestinal homing

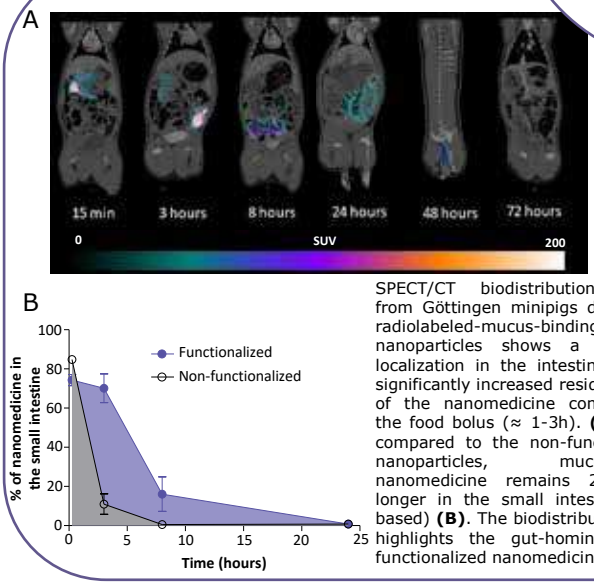

SPECT/CT biodistribution images from Göttingen minipigs dosed with radiolabeled-mucus-binding nanoparticles shows a controlled localization in the intestine and a significantly increased residence time of the nanomedicine compared to the food bolus (≈ 1-3h). **(A)**. When compared to the non-functionalized nanoparticles, mucus-binding nanomedicine remains 2,7 times longer in the small intestine (AUC based) **(B)**. The biodistribution study highlights the gut-homing of the functionalized nanomedicine.

3. Fully biocompatible

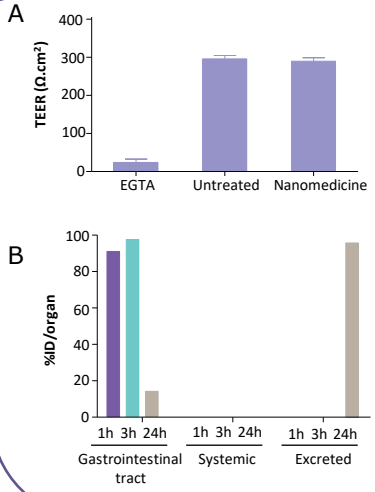

The transepithelial electrical resistance (TEER) measurements across Caco2-HT29-MTX-E12 monolayers shows that the integrity of the epithelial barrier remains intact when in contact with the functionalized nanomedicine **(A)**. The biodistribution study of radiolabeled-mucus-binding nanoparticles after gavage in mice shows that the nanomedicine is localized in the gastrointestinal tract and remains non-systemic. Moreover, the excretion of the compound is in accordance with the mucus turn-over in mice (12-24h) underlying the mucoadhesive properties of the nanomedicine in vivo **(B)**. The biocompatibility studies demonstrate that the nanomedicine is safe for gastrointestinal applications.

Conclusion

Herein, we demonstrate the capacity to coat the intestine with stabilized enzyme activity. In addition, we report the perfect biocompatibility of the nanomedicine for gastrointestinal applications. This paves the way to the development of a series of novel drug compounds for digestive diseases.

Culturing conditions of mesenchymal stem cells derived exosomes alter their protein corona formation, cellular uptake and *in vivo* organ biodistribution

Revadee Liam-Or, Farid N Faruqu, Adam A Walters, Francesco Dazzi, and Khuloud T. Al-Jamal

Institute of Pharmaceutical Science, King's College London, United Kingdom

INTRODUCTION

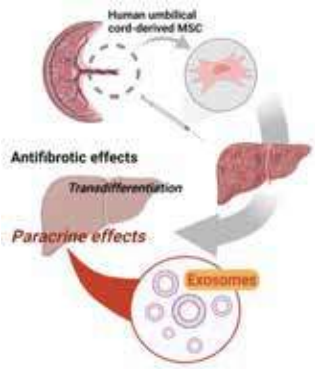

- No effective anti-fibrotic treatments are currently available.
- Several clinical/pre-clinical studies proposed Mesenchymal stem cells (MSCs) as a treatment for liver fibrosis.
- MSC transplantation is limitedly feasible due to low migration and poor cell survival.
- Anti-inflammatory and anti-fibrotic effects are mediated by the paracrine effect of exosomes, ~100-150 nm extracellular vesicles.

AIM

To prepare MSCs derived exosomes (MSC Exo) which have preferential uptake to liver cell subpopulation and induce anti-inflammatory/ anti-fibrotic effects to reduce liver inflammation and fibrosis progression *in vivo*.

METHODS

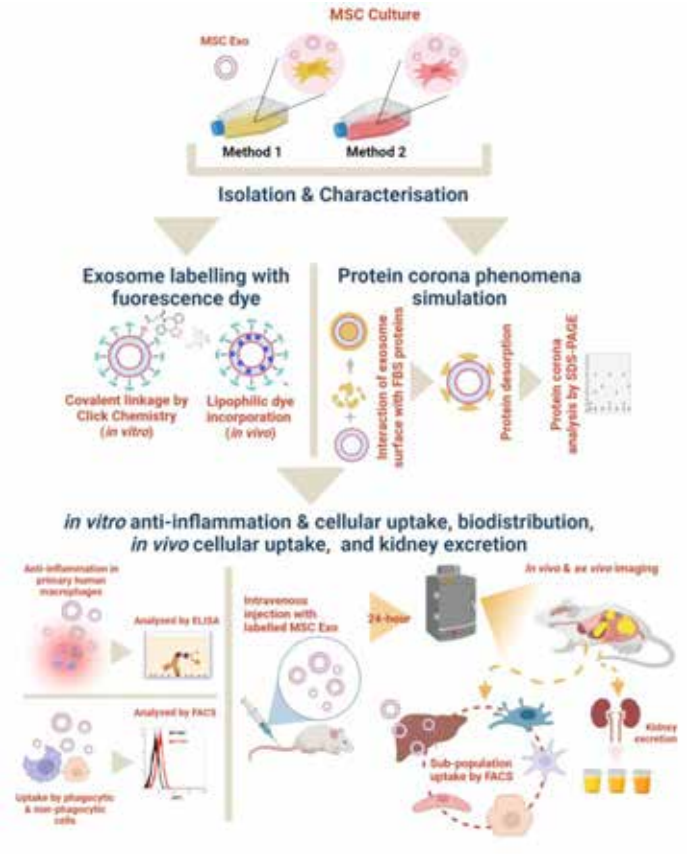

Study of *in vitro* anti-inflammatory activity, *in vivo* biodistribution and cellular uptake by liver cell sub-populations of MSC Exo derived from different culture conditions associated with protein corona formation phenomenon.

RESULTS

MSC Exo characterisation & protein corona analysis

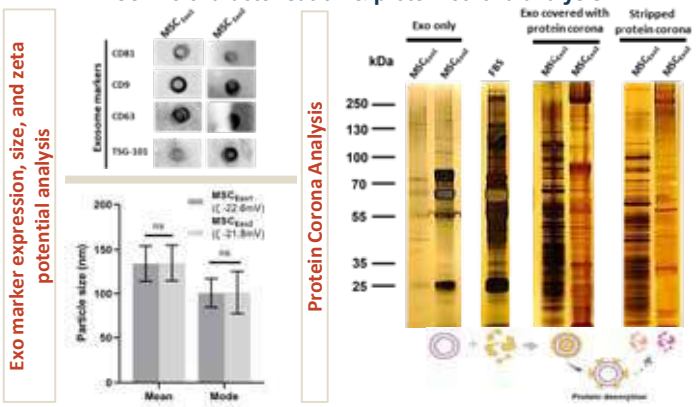

Both type of exosomes expressed exosome markers and were identical in size and zeta-potential. Culturing conditions resulted in different protein corona composition.

In vitro anti-inflammation & cellular uptake

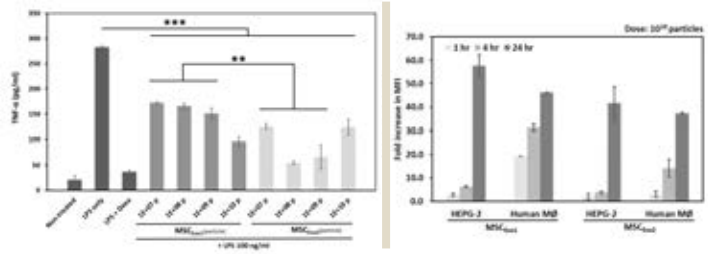

MSC_{Exo2} was more potent than MSC_{Exo1} in anti-inflammation evaluated in primary human macrophages (Human MØ). Both MSC Exo types tended to be more taken up by phagocytic cells than non-phagocytic cells (HEPG-2) over the period of 1-4 hours. The uptake by HEPG-2 could be increased after 24 hour incubation.

Organ biodistribution & urine excretion

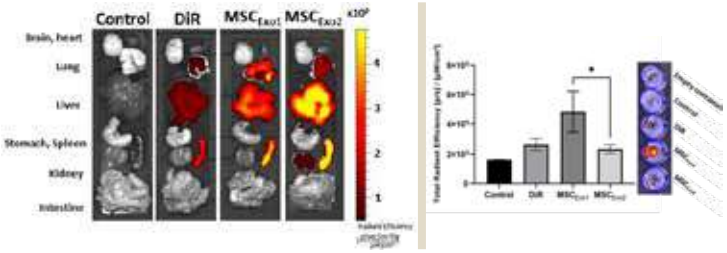

Ex vivo organ imaging showed preferential uptake of MSC_{Exo2} in the liver, while MSC_{Exo1} was excreted more quickly when compared to MSC_{Exo2} over the period of 24 hour post IV.

Uptake of MSC Exo by liver sub-populations

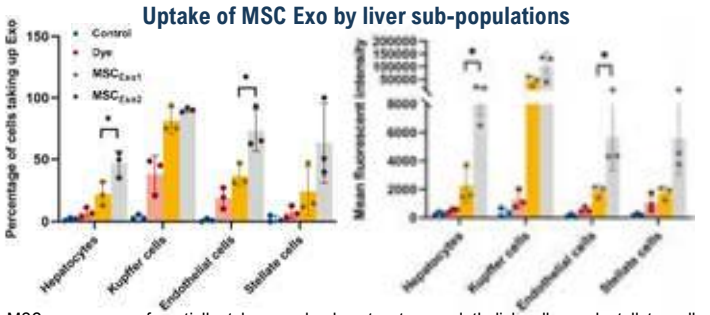

MSC_{Exo2} were preferentially taken up by hepatocytes, endothelial cells, and stellate cells, whereas no difference in the uptake by Kupffer cells between two types of MSC Exo.

CONCLUSIONS

- Culturing conditions did not affect the size and zeta potential of MSC Exo, but could affect the protein corona formation.
- Both MSC exo could mediate the anti-inflammatory effect in Human MØ and exerted good uptake in phagocytic and non phagocytic cells present in the liver (HEPG-2 & Human MØ).
- Organ biodistribution was highly dependent of culturing condition i.e., MSC_{Exo2} favoured accumulation in the liver, while MSC_{Exo1} favoured kidney excretion.
- MSC_{Exo2} had higher uptake in hepatocytes, endothelial cells, and stellate cells, which will be more beneficial for developing therapeutics for liver fibrosis.
- Future works will be focused on *in vivo* therapeutic effects mediated by both types of MSC Exo in animal model with liver fibrosis and association between protein corona composition and organ biodistribution investigated by LC-MS.

REFEENCES: Faruqu FN, Wang JT, Xu L, et al. Theranostics. 2019:1666-1682., Cao, J., Wang, B., Tang, T. et al. Stem Cell Res Ther. 2020:206., Kim M, Yun HW, Park DY, Choi BH, Min BH. Tissue Eng Regen Med. 2018:427-436.

UNIVERSITÄTSmedizin. MAINZ
Hautklinik und Poliklinik

Nanodimensionale polymere Therapeutika für die Tumortherapie
SFB 1066

Biological effects of systemically administered TLR7/8 agonist and antigen-conjugated nanogels on immune cells populations

Carolina Medina-Montano[1], Judith Stickdorn[2], Maximilian Haist[1], Matthias Bros[1], Stephan Grabbe[1], Hansjörg Schild[3], and Lutz Nuhn[2]
1. Department of Dermatology, UMC of the JGU Mainz, Germany. 2. Max Planck Institute for Polymer Research, Mainz, Germany. 3. Institute for Immunology, UMC of the JGU Mainz, Germany.

Introduction

Therapeutic vaccination against tumor antigens is of great interest regarding the variety of tumor types and individual immune condition for each patient. Vaccines for tumor therapy need to comprise tumor antigen, adjuvant and have to ensure passive or active targeting of antigen presenting cells in order to elicit tumor-specific adaptive immune responses. Different strategies, including delivering antigen- encoding mRNAs peptides and full protein-antigens require immune-boosting adjuvants as well as carrier platforms to ensure cell type-specific uptake.

Here, we introduce a pH-responsive nanogel platform the delivery of antitumor vaccinations. The underlying chemical design allows for covalent attachment of an antigen as exemplified in this study for the model antigen ovalbumin and an immune adjuvant (imidazoquinoline-type TLR7/8 agonist) onto the same nanocarrier system.

Results

Synthesis and characterization of TLR7/8 Agonist and Antigen-conjugated nanogels

→ Click reaction works and yields the desired peptide-decorated nanogels

Synthetic design concept based on double reactive precursor block copolymers that self-assemble into block copolymer micelles with amine-reactive cores and a SPAAC-reactive corona. Via aminolysis of the pentafluorophenyl esters, the cores are covalently functionalized with the TLR7/8 agonist IMDQ and Texas Red cadaverine and then sequentially cross-linked and transformed into pH-responsive nanogels. The corona is modified via click ligation of the surface-exposed azides to DBCO-modified (and Alexa Fluor 488-labeled) OVA as model antigen.

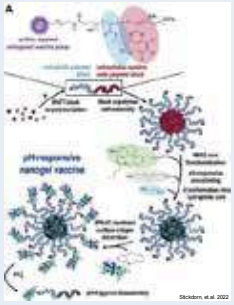

Two-Component nanogel platform can be applied intravenously and generates a cellular immune response

Uptake and maturation

In spleen immune cells

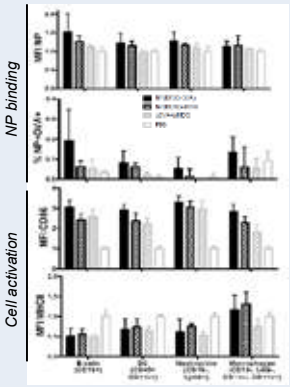

In liver immune cells

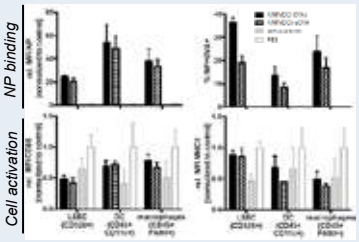

Flow cytometric analysis of liver and spleen immune cell types confirmed uptake of nanocarriers into various antigen-presenting immune cell subpopulations at varying extent. Co-delivery of IMDQ-functionalized particles with OVA protein worked best for the covalent conjugate in most of these immune cell types.

Results

Biodistribution

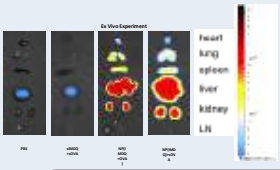

Quantification on organ level

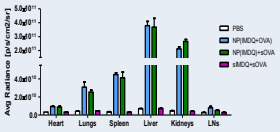

We observed that polymeric nanocarriers when conjugated with TLR7/8 agonists accumulated in the liver and in the kidneys..

Serum shows high levels of pro-inflammatory cytokines

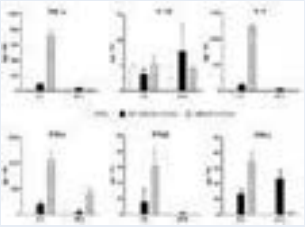

We also monitored the cytokine profile of mice 24 h after i.v. injection and observed the highest levels of the pro-inflammatory cytokines TNF-α and INF-γ in case of application of the dual-antigen/adjuvant loaded nanogel NP(IMDQ+OVA).

Monitoring of liver enzyme parameters displayed no treatment-dependent differences

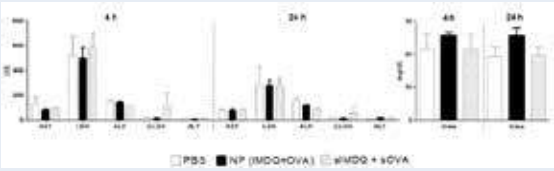

Prompted by the strong accumulation of the nanogels in the liver, we assessed liver enzyme parameters in the blood, but could not observe any signs of toxicity.

Nanogels no elicit histological anomalies

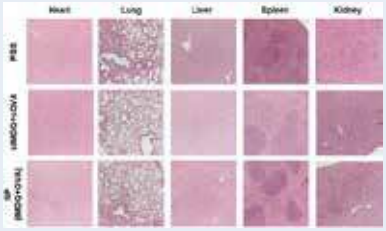

Moreover, histopathological analyses by hematoxylin−eosin staining of liver, spleen, kidney, heart, and lung tissue showed no histological anomalies after i.v. injection of the nanovaccine.

Conclusion

Here, we introduce a pH-responsive nanogel platform which codelivers antigen and adjuvant intended for tumor therapy. This vaccination platform is safe for intravenous application and elicits robust immune responses. Our two-component nanovaccine leads to an uptake of particles into various antigen-presenting immune cell subpopulations, resulting in a specific immune response in spleen and liver immune cells. Analyzed maturation markers (CD86 and MHC-II) in the corresponding immune cell subpopulations showed an activation in the liver, and in the spleen all IMDQ-containing NP increased the expression levels of CD86. Serum showed the highest levels of the pro-inflammatory cytokines TNF-α and INF-γ for the dual-loaded nanogel NP(IMDQ+OVA). Prompted by the strong accumulation of the nanogels in the liver, we monitored liver enzyme parameters in the blood, but observed no differences between different samples both after 4 and 24 h. Moreover, histopathological analyses by hematoxylin−eosin staining of liver, spleen, kidney, heart, and lung tissue showed no histological anomalies after i.v. injection of the nanovaccine.

Altogether, these findings highlight the enhanced safety profile of nanogel-bound IMDQ even after injection into the bloodstream, avoiding adverse systemic immune responses, but instead providing better access to circulating immune cells for improved vaccination performance. Regarding the versatile opportunities for functionalization, our nanogels are promising for the development of highly customized and potent nanovaccines.

References

Contact: gmedinam@students.uni-mainz.de

1. Stickdorn J, Stein L, Arnold-Schild D, Hahlbrock J, Medina-Montano C, Bartneck J, Ziß T, Montermann E, Kappel C, Hobernik D, Haist M, Yurugi H, Raabe M, Best A, Rajalingam K, Radsak MP, David SA, Koynov K, Bros M, Grabbe S, Schild H, Nuhn L. Systemically Administered TLR7/8 Agonist and Antigen-Conjugated Nanogels Govern Immune Responses against Tumors. ACS Nano. 2022 Feb 1. doi: 10.1021/acsnano.1c10709. Epub ahead of print. PMID: 35103463.Bros, M.; Nuhn, L.; Simon, J.; Moll, L.; Mailander, V.; Landfester, K.; Grabbe, S., The Protein Corona as a Confounding Variable of Nanoparticle-Mediated Targeted Vaccine Delivery. Frontiers in immunology 2018, 9, 1760.
2. Nuhn, L.; Van Hoecke, L.; Deswarte, K.; Schepens, B.; Li, Y.; Lambrecht, B. N.; De Koker, S.; David, S. A.; Saelens, X.; De Geest, B. G. Potent Anti-Viral Vaccine Adjuvant Based on PH-Degradable Nanogels with Covalently Linked Small Molecule Imidazoquinoline TLR7/8 Agonist. Biomaterials 2018, 178, 643−651.
3. Dowling, D. J. Recent Advances in the Discovery and Delivery of TLR7/8 Agonists as Vaccine Adjuvants. ImmunoHorizons 2018, 2(6), 185−197.
4. Nuhn, L.; De Koker, S.; Van Lint, S.; Zhong, Z.; Catani, J. P.; Combes, F.; Deswarte, K.; Li, Y.; Lambrecht, B. N.; Lienenklaus, S.; et al. Nanoparticle-Conjugate TLR7/8 Agonist Localized Immunotherapy Provokes Safe Antitumoral Responses. Adv. Mater. 2018, 30 (45), 1803397.

Nanodiamond magnetometry for real-time monitoring of drug efficiency in arthritis treatment

Aldona Mzyk[1,2], Yuchen Tian[1], Viraj Damle[1], Aryan Morita[1], Miguel Alejandro Reina Mahecha[1], Maria Sandovich[1], Hugo van der Veen [1], Romana Schirhagl[1]

[1]UMCG/RUG, Groningen, The Netherlands
[2]IMMS PAS, Krakow, Poland

Introduction

Nanodiamond magnetometry: quantum sensing technique (nanoscale MRI) that enables real time detection of free radical generation.

Free radicals (FRs): short-lived reactive chemical species with unbound electrons. Their imbalance is linked with arthritis development.

Probes: fluorescence nanodiamonds (FNDs) with NV centers that emit red photons upon green laser light illumination. FNDs have magnetic states (marked with ms = +1 and −1) that enable nanoscale MRI.

T1 relaxation time: shorter for a NV center in the presence of higher concentration of the free radicals.

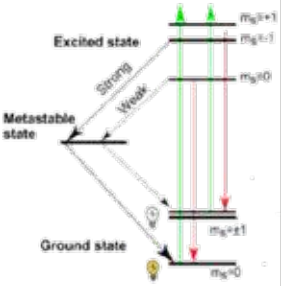

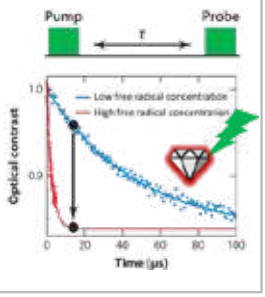

Experimental

In this research we have collected synovial fluid (SF) from patients with:

- Osteoarthritis (OA)
- Rheumatoid arthritis (RA)

We have measured FRs generation using:

- Nanodiamond magnetometry
- DCFDA assay (conventional fluorescent dye)

Results

Free Radicals in synovial fluid

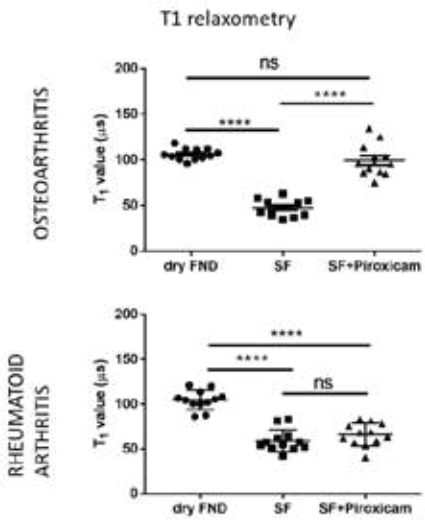

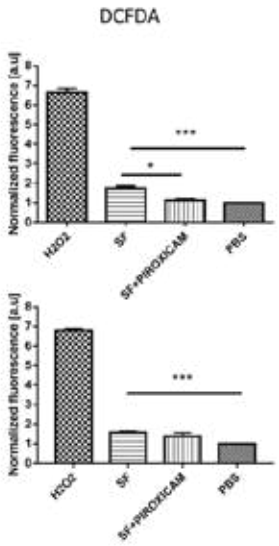

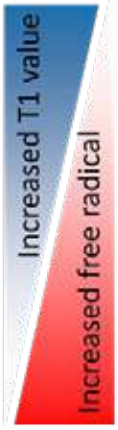

Free Radicals in cells from synovial fluid

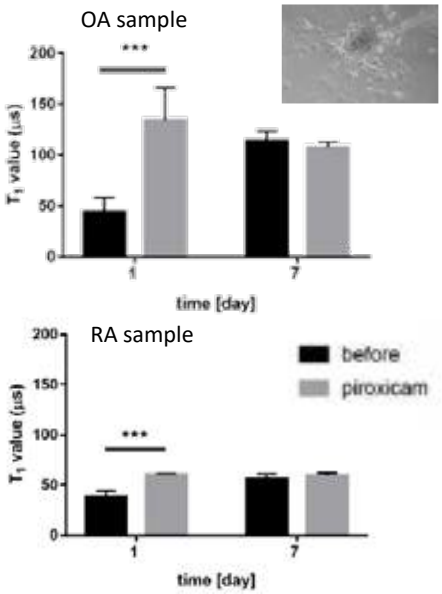

Summary

Our studies have shown for the first time that fluorescent nanodiamonds can detect free radical generation in samples from arthritis patients. This experiment has also presented that nanodiamond magnetometry enables to monitor efficiency of anti-inflammatory therapeutics in real-time. We have found that RA cells are less responsive to piroxicam treatment.

Acknowledgements

Contact details: a.i.mzyk@umcg.nl; romanaschirhagl@gmail.com

Temperature, concentration, and surface modification influence the protein corona

MAX PLANCK INSTITUTE FOR POLYMER RESEARCH

Jennifer Oberländer[1,2 §], Carole Champanhac[1 §], Richard da Costa Marques[1,2], Katharina Landfester[1], Volker Mailänder[1,2]

1. Max-Planck-Institute for Polymer Research, Ackermannweg 10, 55122 Mainz, Germany.
2. Department of Dermatology, University Medical Center of the Johannes Gutenberg-University Mainz, Langenbeckstraße 1, 55131 Mainz, Germany.
§. These authors share the 1st authorship

Background and Motivation

The presence of protein corona around nanocarriers after they have come into contact with protein-containing liquids has been investigated multiple times. However, consistency regarding coating conditions (type of plasma, plasma concentration, temperature…) is not always achieved, making cross-referencing results difficult. Here, we investigated the influence of four key parameters of polystyrene nanoparticles (surfactant, surface charge, temperature, and plasma concentration) on the formation and composition of the protein corona and ultimately on the cellular uptake of pre-coated nanoparticles. We demonstrate that an increase of the human plasma concentration or an increase of the coating temperature leads to a decrease of the uptake of nanoparticles into HeLa cells.

Workflow

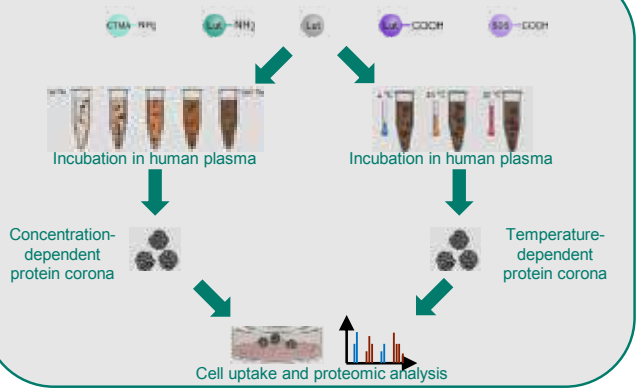

Concentration-dependent protein corona

Uptake of PS-nanoparticles in HeLa cells

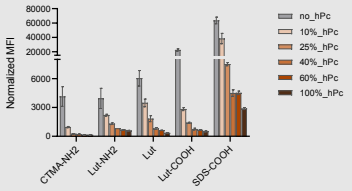

- Reduction of cell uptake with increasing plasma concentration

Top proteins in protein corona

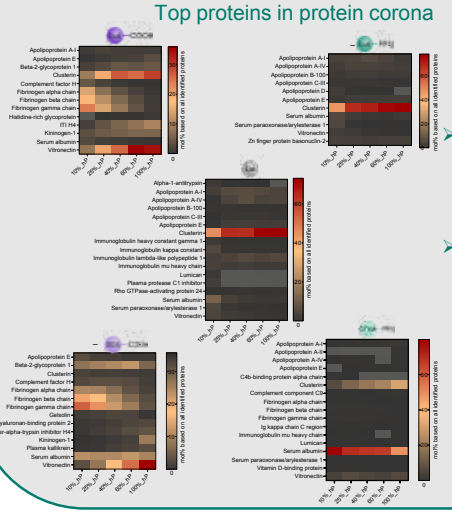

- Increase of clusterin and vitronectin with increasing plasma concentration
- Decrease of serum albumin and fibrinogen with increasing plasma conentration

Temperature-dependent protein corona

Uptake of PS-nanoparticles in HeLa cells

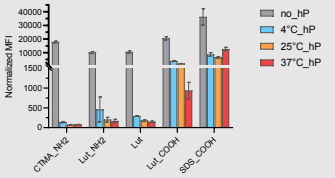

- Reduction of cell uptake with increasing temperature

Top proteins in protein corona

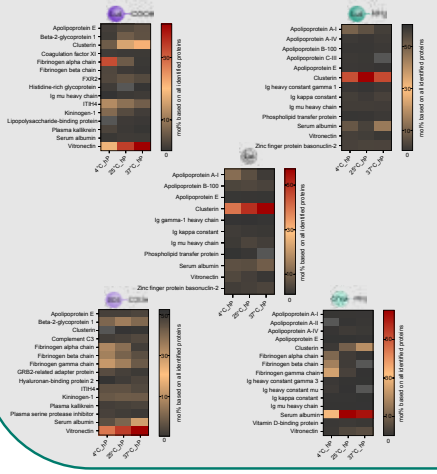

- Increase of clusterin, serum albumin and vitronectin with increasing temperature
- Decrease of fibrinogen with increasing temperature

Conclusion

- Protein corona composition varies with plasma concentration and plasma temperature
- Effect has been observed independently of surface functionalization and surfactant
- Differences in protein corona lead also to differences in cellular uptake
- Cell uptake is reduced with increasing plasma concentration or increasing temperature

UNIVERSITÄTSmedizin. MAINZ

SFB 1066

Jennifer Oberländer (oberlaenderj@mpip-mainz.mpg.de)

FcRn-targeted nanomedicines for intestinal delivery of an antidiabetic peptide

Soraia Pinto [1,2*], **Hélder Santos**[3], **Bruno Sarmento**[1,4]

[1]i3S – Instituto de Investigação e Inovação em Saúde, Universidade do Porto, Porto, Portugal
[2]ICBAS – Instituto de Ciências Biomédicas Abel Salazar, Universidade do Porto, Porto, Portugal
[3]Department of Biomedical Engineering, University Medical Center Groningen, Groningen, The Netherlands
[4]CESPU, Instituto de Investigação e Formação Avançada em Ciências e Tecnologias da Saúde & Instituto Universitário de Ciências da Saúde, Gandra, Portugal
*e-mail: soraia.pinto@i3s.up.pt

Aim

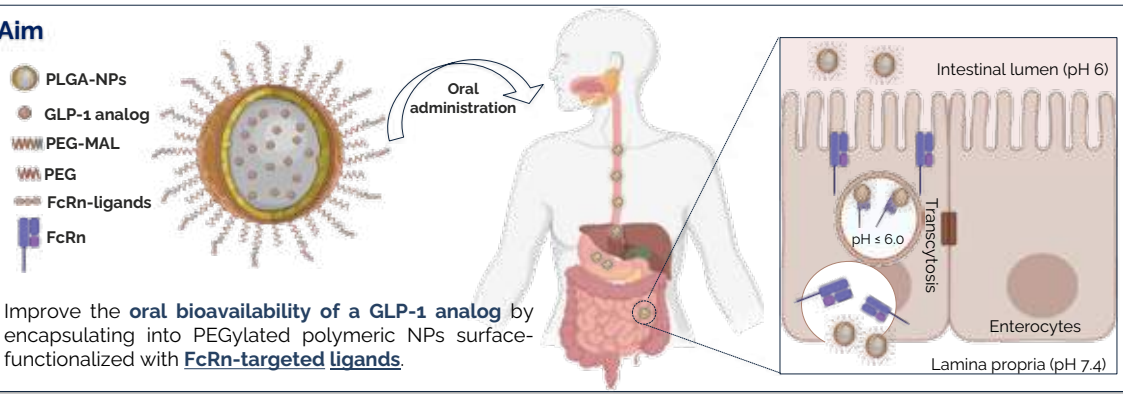

Improve the **oral bioavailability of a GLP-1 analog** by encapsulating into PEGylated polymeric NPs surface-functionalized with **FcRn-targeted ligands**.

Treatment of type 2 diabetes *mellitus*

Methods & Results

A. Binding of FcRn-targeted ligands to hFcRn by SPR

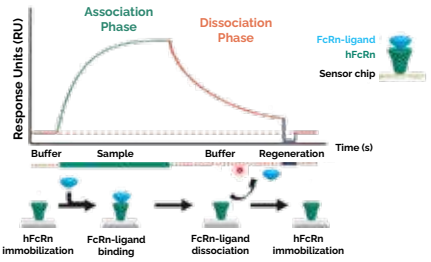

FcRn-targeted ligand	KD (pH 6.0)	KD (pH 7.4)
$FcBP_1$ (QRFVTGHFGGLHPANG)	No binding	No binding
$FcBP_2$ (CQRFVTGHFGGLHPANG)	No binding	No binding
$FcBP_3$ (CQRFVTGHFGGLYPANG)	16.1 ± 3.2 µM	No binding
$FcBP_4$ (CQRFCTGHFGGLYPCNG)	No binding	No binding
$ZFcRn_{16}$-Cys (VDAKYAKEWMRAAHEIR WLPNLTFDQRVAFIHKLEDDPSQSSELLSE AKKLNDSQAPKC)	75 ± 32 nM	No saturation

B. PLGA-PEG-MAL functionalization with FcRn-targeted ligands

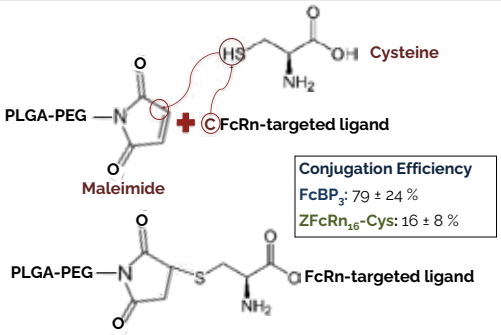

Conjugation Efficiency
$FcBP_3$: 79 ± 24 %
$ZFcRn_{16}$-Cys: 16 ± 8 %

C. Production of GLP-1 analog-loaded NPs

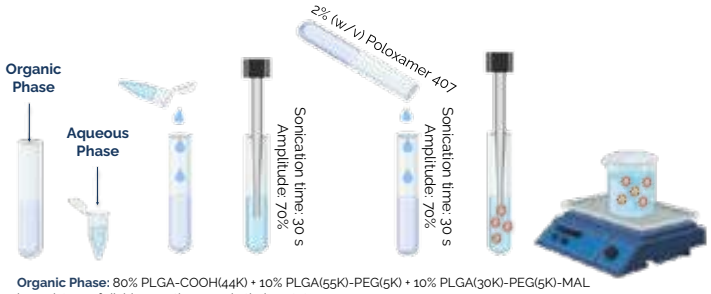

Organic Phase: 80% PLGA-COOH(44K) + 10% PLGA(55K)-PEG(5K) + 10% PLGA(30K)-PEG(5K)-MAL in a mixture of dichloromethane and ethyl acetate

Aqueous Phase: GLP-1 analog (TL = 5%) in ultrapure water

Physicochemical characterization of empty NPs and GLP-1 analog-loaded NPs

Formulation	Average Size (nm)	PdI	ζ-Potential (mV)	AE (%)	DL (%)
Empty NPs	113 ± 2	0.147 ± 0.023	-3.0 ± 0.2	-	-
GLP-1 analog-loaded NPs	110 ± 2	0.163 ± 0.016	-2.3 ± 0.2	78.2 ± 8.4	3.7 ± 0.4

D. *In vitro* release study in GLP-1 analog-loaded NPs

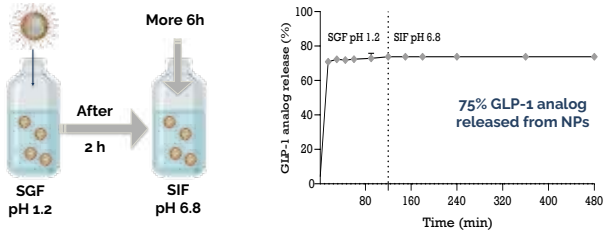

Future Perspectives

Reduce the burst release of the GLP-1 analog.
Evaluate the secondary structure of the GLP-1 analog.
Produce functionalized GLP-1 analog-loaded NPs.
Evaluate the binding-affinity of functionalized NPs with the hFcR by SPR.
Perform *in vitro* uptake studies.

References

[1] IDF Diabetes Atlas. 10th Edition. 2021. 12-17.
[2] Azevedo C, *et al. Advanced Drug Delivery Reviews.* 2021; 175, 113778.
[3] Araújo F. *et al., Journal of Diabetes Science and Tecnology.* 2012; 6(6):1486-1497.
[4] Sockolosky JT, *et al. Proceedings of the National Academy of Sciences of the United States of America.* 2012; 109(40), 16095-100.
[5] Seijsing J. *et al. Proceedings of the National Academy of Sciences of the United States of America. 2014; 111(48), 17110-17115.*

INSTITUTO DE INVESTIGAÇÃO E INOVAÇÃO EM SAÚDE
UNIVERSIDADE DO PORTO

Rua Alfredo Allen, 208
4200-135 Porto
Portugal
+351 220 408 800

www.i3s.up.pt

Acknowledgments

FCT SFRH/BD/144719/2019

Development of Self-Powered Multifunctional Piezomagnetic Nanoparticles for non-invasive BBB modulation and glioblastoma treatment

Arathyram Ramachandra Kurup Sasikala [1*], Dean Kavanagh[2], Hanene Ali-Boucetta[1]

[1] School of Pharmacy, Institute of Clinical Sciences, College of Medical and Dental Sciences, University of Birmingham, Edgbaston, Birmingham, B15 2TT, UK

[2]Institute of Cardiovascular Sciences, College of Medical and Dental Sciences, University of Birmingham, Edgbaston, Birmingham, B15 2TT, UK

Correspondence: a.ramachandrakurupsasikala@bham.ac.uk

Introduction

Current therapies for diseases affecting the brain such as brain cancer and neurodegenerative disorders are limited to those which only reduce the symptoms of the disease but don't stop its progression or treat it[1]. This is due to the presence of a tight barrier in the brain known as the blood brain barrier (BBB) which separates the brain tissue from the body's normal blood circulation. It acts as a protective barrier to the brain from unwanted chemicals but often presents a challenge in shuttling therapeutic cargoes into the brain[2]. Therefore, there is a pressing need for the development of novel drug delivery systems (DDS) to shuttle drugs across the BBB. Recently, a new class of innovative nanoparticles have arisen in the form of piezoelectric nanoparticles which convert any form of mechanical stimulation (such as ultrasound (US)) into electric signals[3] and will be a promising alternative for non-invasive electroporation by producing remote electrical stimulation to cells allowing for the perfusion of agents across the BBB

Aims

- Development of a unique ultrasound (US) and magnetic field (MF) responsive nanoparticle system based on piezoelectric barium titanate and superparamagnetic iron oxide nanoparticles termed as PiezoMagnetic nanoparticles (PMNPs) for the non-invasive BBB modulation
- Assessment of BBB penetration capability of PMNPs in self -assembled multicellular BBB spheroid models using the intrinsic Second Harmonic Generation (SHG) Imaging property of PMNPs.
- Evaluation of therapeutic efficacy of anticancer drug cisplatin (CDDP) conjugated PMNPs on 3D models of glioblastoma multiforme (GBM).

Methods

1. Development of PMNPs were carried out by adding tetragonal barium titanate nanoparticles (BTNPs) to a Fe_3O_4 precursor solution and made them react directly as shown in the Figure 1.

2. Physicochemical characterization of PMNPs were carried out using HRTEM, XRD and FTIR measurements. Ultrasound induced electrical performance of PMNPs were analysed by fabricating a flexible film of PMNPs using PDMS through film casting technique

Figure 1: Schematic showing the synthesis of PMNPs

3. Development of self assembled multicellular BBB spheroid models by coculturing primary human astrocytes, human brain vascular pericytes(HBVP) and primary human brain microvascular endothelial cells(HBMEC).

4. BBB penetration capability of PMNPs was evaluated in self -assembled multicellular BBB spheroid models using the intrinsic Second Harmonic Generation (SHG) Imaging property of PMNPs when stimulated with US (Pulse repetition Frequency 100 Hz, Duty cycle 50%, 0.3W/cm2). Due to the piezoelectric property of PMNPs, they exhibit great efficacy to transduce non-invasive US signals to electrical signals to permeate the tight junction formed by the endothelial cells in the BBB through nano-electroporation as shown in Figure 2.

5. Covalent conjugation of anticancer drug cisplatin to the PMNPs were done and evaluated its anticancer efficacy on glioma (U87) 2D monolayers and tumour spheroids under US stimulations

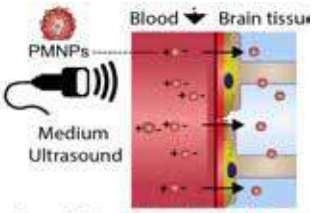

Figure 2: Schematic showing the BBB penet

Results

1. Synthesis and characterisation of PMNPs

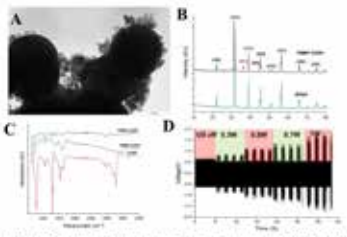

Figure 3: A) HR TEM image of as prepared PMNPs, B) XRD of PMNPs and tetragonal BTNPs, C) FTIR image showing the covalent conjugation of PMNP CDDP, D) output voltage signals from PMNPs stimulated with ultrasound at pulsed mode with 50 % duty cycle and different intensities.

2. Biocompatibility studies of PMNPs

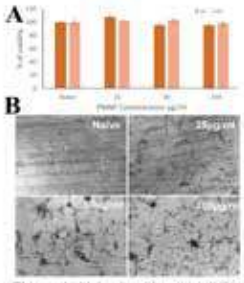

Figure 4: A) In vitro biocompatibility of U87 treated with PMNPs with different concentrations on 24 h and 48 h, B) Bright field image showing the uptake of PMNPs by U87 at 48h .

3. Development and cellular organisation of Multicellular BBB spheroids

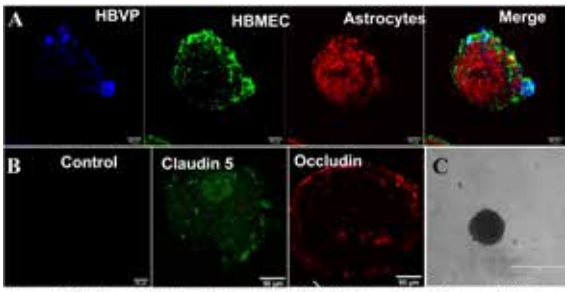

Figure 5. Cellular organization of the multicellular BBB spheroids; A) Representative two-photon images showing the organization of human astrocytes (Red), HBVP (blue) and (a) primary HBMEC (green) when co-cultured to form a spheroid. Astrocytes were pre-labelled with Cell Tracker Deep Red, HBVP with cell tracker blue and HBMEC with cell tracker CM Dil for 1h before coculturing in ultra low attachment plates, B) Two photon images showing the expression of tight junction markers, claudin 5 (green) and occludin (Red) in self-assembled BBB spheroids, C) bright field image of BBB spheroid at 48h

4. US induced penetration capability of PMNPs

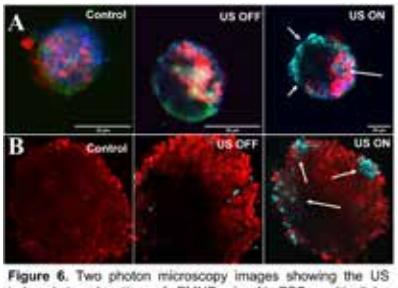

Figure 6. Two photon microscopy images showing the US induced translocation of PMNPs in A) BBB multicellular spheroids (at 25.2 µm depth) and B) U87 spheroids (at 147 µm depth). Cyan colour indicates the SHG signals from PMNPs, For imaging BBB spheroids astrocytes were pre-labelled with Cell Tracker Deep Red, HBVP with cell tracker blue and HBMEC with cell tracker CM Dil. U87 spheroids were pre-labelled with Cell Tracker Deep Red

5. Therapeutic efficacy of PMNP CDDP for glioblastoma treatment

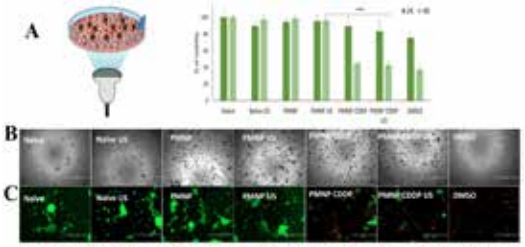

Figure 7. In vitro anticancer effects of PMNP CDDP in human glioma cell lines U87 A) 2D monolayer, B) bright field images and C) Live dead of 2D U87 cell lines treated with PMNPs

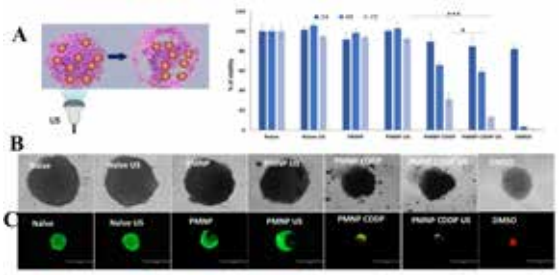

Figure 8. In vitro anticancer effects of PMNP CDDP in human glioma cell lines U87 A) 3D spheroids, C) bright field images and D) Live dead off 3D U87 cell lines treated with PMNPs

Conclusion and future perspective

Ultrasound responsive self powered PMNPs were successfully developed that were able to translocate effectively into BBB spheroids. The PMNP CDDP when stimulated with US exhibited superior anticancer effects in 3D GBM models compared to the PMNP CDDP without US. This is due to the synergistic effect of enhanced cellular penetration of PMNPs and anticancer therapeutic (CDDP) delivery from PMNPs when stimulated with US . Future studies will develop a blood brain barrier tumour model to test the anticancer effects of PMNPs before moving into the *in vivo* studies

Acknowledgement and Reference

This research has been funded by the European Union's Horizon 2020 Research and Innovation Programme under the Marie Sklodowska-Curie Grant Agreement No 898170

Reference

1) 1.Kadry, H.; Noorani, B.; Cucullo, L. Fluids Barriers Cns 2020, 17, (1).
2) 2.Hu, Y.; Hammarlund-Udenaes, M. Mol Pharmaceut 2020, 17, (11), 4029-4039.
3) 3.Sharabi, S.; Bresler, Y.; Ravid, O.; Shemesh, C.; Atrakchi, D.; Schnaider-Beeri, M.; Gosselet, F.; Dehouck, L.; Last, D.; Guez, D.; Daniels, D.; Mardor, Y.; Cooper, I. Drug Deliv 2019, 26, (1), 459-469.

In vivo application of CRISPR/Cas9 gene editing using lipid nanocarriers for therapeutic immune target identification in Glioblastoma

Nadia Rouatbi[1], Julie Tzu-Wen Wang[1], Steven Pollard[2], James Arnold[1] & Khuloud T. Al-Jamal[1]
[1]Institute of Pharmaceutical Sciences, Faculty of Life Sciences and Medicine, King's College London
[2]MRC Centre for Regenerative Medicine, University of Edinburgh

INTRODUCTION

- Despite advances in cancer immunotherapy, little progress has been accomplished in its clinical translation for glioblastoma (GBM). Failures are associated with multiple factors including the highly immunosuppressive tumour microenvironment (TME), tumour heterogeneity, limited drug penetration due to the blood-brain barrier, and the presence of glioblastoma stem cells (GSC) that further contribute to treatment resistance [1].
- CD47 is a transmembrane protein that is overexpressed by multiple types of cancers and it is emerging as a potential immune checkpoint for cancer immunotherapy. Binding of CD47 with its ligand, signal regulatory (SIRPα), inhibits the phagocytic ability of macrophages and microglia, allowing cancer cells to escape immune surveillance and promote tumour proliferation [2].

AIM

The specific aim of this project is to develop an optimised lipid nanocarrier, namely, stable nucleic acid-lipid particles (SNALPs) for *in vivo* CRISPR/Cas9 gene editing of GBM, GSC and/or immune cells in the brain for therapeutic target identification purpose.

METHODS

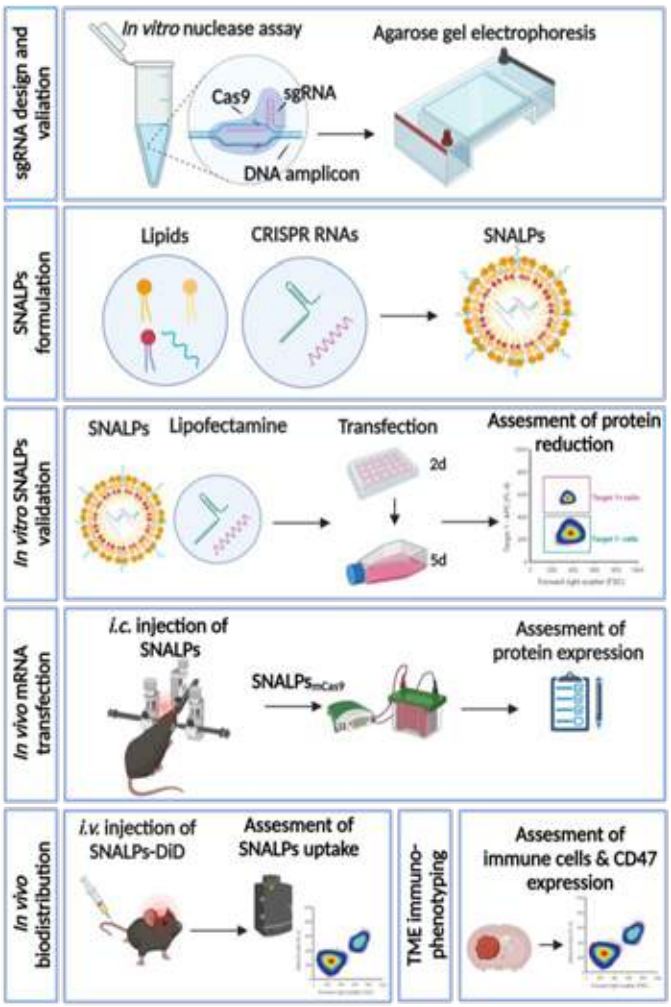

RESULTS

sgCD47 validation

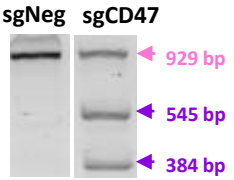

✓sgRNA against the gene of interest (sgCD47) was designed and target specificity was confirmed.

Size/charge characterisation

Size (d.nm)	PDI
139.13 ± 16.5	0.184 ± 0.03

Charge (mV)	mCas9/sgRNA EE(%)
0.4 ± 3.09	89.79 ± 8.88

✓Formulated SNALPs were characterized by particle size <200nm, neutral charge at P.H. 7 and ~90% EE.

In vitro gene knockout validation

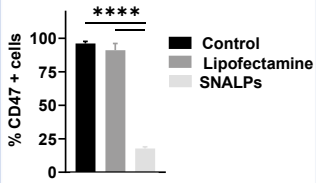

✓SNALPs induced CD47 knockout in GSC (BL6) more efficiently than commercial Lipofectamine.

In vivo mRNA transfection

✓SNALPs encapsulating *m*Cas9 (SNALPs$_{mCas9}$) resulted in Cas9 protein expression in BL6 tumour tissues.

In vivo SNALPs biodistribution

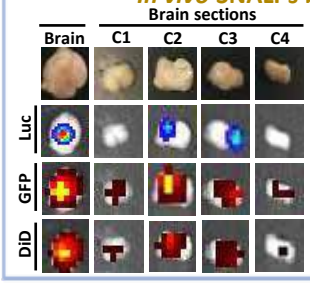

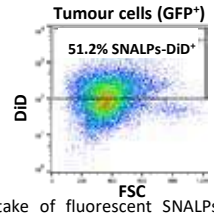

✓Uptake of fluorescent SNALPs (SNALPs-DiD) by orthotopic GSC (BL6) was confirmed by optical imaging and flow cytometry.

Ex-vivo TME immunophenotyping

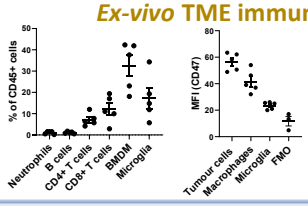

✓Immune sub-populations within the TME were identified following antibody staining and flow cytometry analysis.
✓*CD47* expression on tumour cells, macrophages and microglia was confirmed.

CONCLUSIONS

SNALPs induced efficient knockout of CD47 *in vitro*, and were able to transfect *m*Cas9 into orthotopic GSC tumours following *i.c.* injection. SNALPs were shown to accumulate in intracranially implanted BL6 tumours. The next phase of the project will investigate the *in vivo* gene editing efficiency following *i.c.* or *i.v.* injection.

References:
[1] Sampson, John H., et al. " *Nature Reviews Cancer* 20.1 (2020): 12-25.
[2] von Roemeling, Christina A., et al. *Nature communications* 11.1 (2020): 1-12.

CLINAM
European Foundation for Clinical Nanomedicine

UNIVERSITÄTSmedizin. Department of Dermatology

Antigen nanocapsule-based combinatorial delivery of STING and TLR7/8 agonists enhances anti-tumor immune responses

Jenny Schunke[1], Natkritta Hüppe[2], Michael Fichter[1,2], Tanja Klaus[1], Michael Kuske[1], Vanessa Bolduan[1], Matthias Bros[1], Stephan Grabbe[1], Katharina Landfester[2], Volker Mailänder[1,2]

1. Department of Dermatology, University Medical Center of the Johannes Gutenberg University Mainz 2. Max Planck Institute for Polymer Research Mainz

Introduction

The prerequisite to generate effective anti-cancer immune responses is the simultaneous delivery of antigens and adjuvants to antigen-presenting cells. Therefore, the aim of this study was the development of protein-based polymeric nanocapsules (NC) consisting of an ovalbumin (OVA) shell and a liquid core containing multiple immunostimulatory adjuvants. The combined encapsulation of R848 (TLR 7/8 agonist) and diABZI (STING agonist) in OVA-NC led to tremendous dendritic cell (DC) maturation, substantial secretion of proinflammatory cytokines and chemokines *in vitro* and *in vivo* as well as tumor regression and increased overall survival in a B16 melanoma mouse model. The herein presented immunotherapy increased the number of tumor infiltrating monocytes and $CD8^+$ T cells and led to a downregulated PD-1 expression on tumor-infiltrating cytotoxic T cells. Additionally, the NC-treatment induced a long lasting immunological memory against OVA-expressing tumor cells in tumor rechallenging experiments.

Material and Methods

Nanocapsules:
OVA-NC: Ovalbumin crosslinked by click chemistry (containing Cy5-Oligo).

Primary immune cells of bone marrow and spleen:
All primary immune cells were obtained from C57BL/6J mice, cultured and treated in specific cell culture media and maintained at 37 °C, 7.5% CO_2. In all experiments the cells were handled under sterile conditions.

Mice:
Wildtype C57BL/6J were obtained from Charles River Laboratories.

B16/OVA-Luc cells:
The melanoma cell line was provided by TRON and cultured in DMEM enriched with 10% FCS and Blasticidin (10 µg/ml). The cell line was tested negative for mycoplasma. $5*10^5$ cells resuspended in 100 µl were injected s.c. into the flanks.

Flow cytometric analysis:
Single cell suspensions were incubated with Fc-block (2.4G2) for 10 min at 4 °C and with monoclonal Abs for 30 min at 4 °C (eBioscience: αCD11c-PE-Cy7, αMHC-II-eFl450, αCD80-PE, αCD86-FITC). Data were acquired with Attune NxT (Life Science) and analyzed using Attune NxT software.

Cytometric Bead Array (CBA):
The LEGENDplex Anti-Virus Response Kit (Biolegend) was used to quantify the amount of secreted cytokines/chemokines.

Results

1 Combination of R848 and diABZI (STING agonist) leads to strong DC maturation

1 OVA-NC uptake by BMDC: microscopy

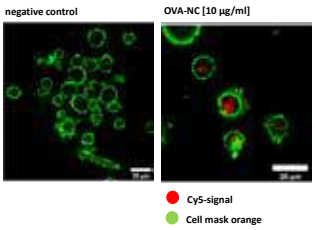

2 OVA-NC treatment increases expression of DC maturation markers

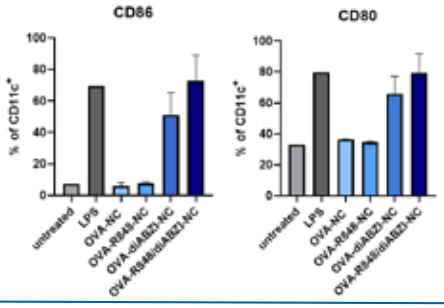

3 Combination of R848 + diABZI leads to secretion of proinflammatory cytokines by splenocytes

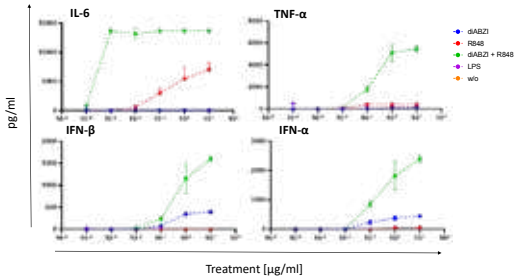

2 Effective treatment of B16 melanoma with diABZI- and diABZI/R848-loaded OVA-Nanocapsules

1 Experimental procedure

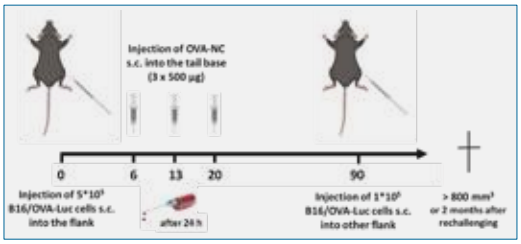

2 Bioluminescent B16/OVA-Luc tumors

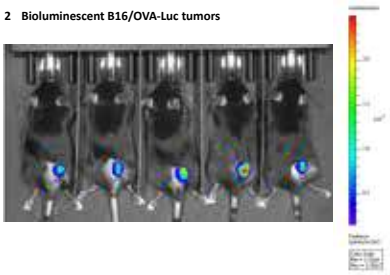

3 Strong secretion of proinflammatory cytokines *in vivo*

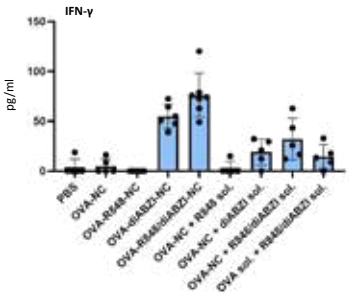

4.1 Tumor growth

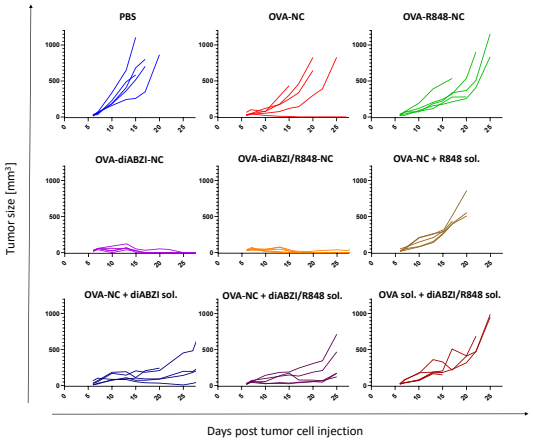

4.2 Tumor growth

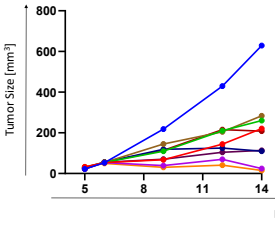

5 Survival

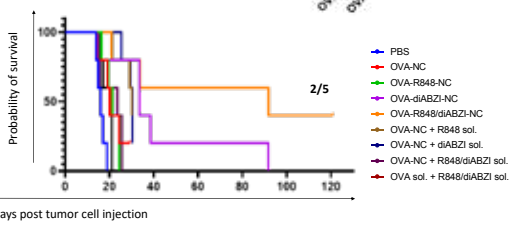

6 Flowcytometric analysis of tumor infiltrating immune cells

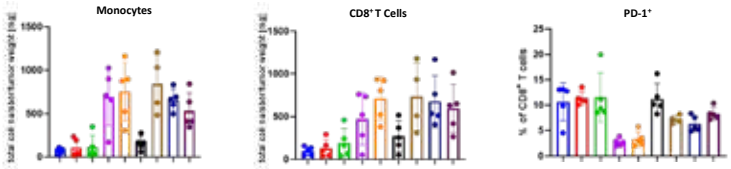

Outlook

- NC application in OVA-independent melanoma model: encapsulation of tumor-specific antigens (e.g. TRP1/TRP2)
- Antibody-based immune cell targeting with OVA-NC
- Optimziation of vaccination scheme and encapsulation of new adjuvant combinations

Summary

The combination of TLR7/8 agonist R848 with diABZI (STING agonist) led to supperadditive effects regarding the maturation and cytokine secretion of DC. Furthermore, mice treated with either OVA-diABZI-NC or OVA-R848/diABZI-NC appeared tumor-free after the 2nd NC injection and showed increased overall survival in a B16 melanoma model even after rechallenge.

pH-Dependent Behavior of Ionizable Cationic Lipids in mRNA-Carrying Lipoplexes Investigated by Molecular Dynamics Simulations

Giovanni Settanni* Wolfgang Brill+, Heinrich Haas+ and Friederike Schmid*
*Physics Department, J.-Gutenberg University Mainz, + BioNTech SE, Mainz

Structure of the lipoplex

The periodic stack of lipid-rich and rna-rich phases is reproduced by the simulations.

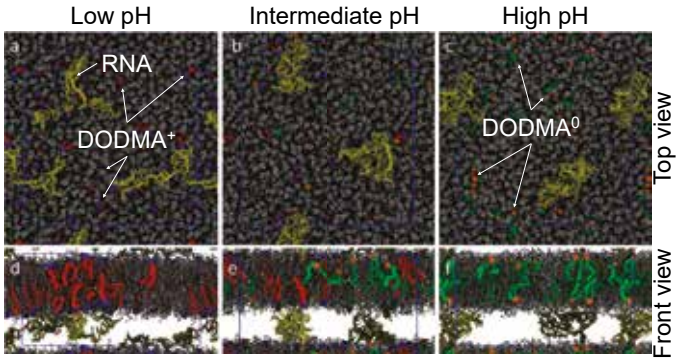

The charged ionizable lipids (DODMA+) accumulate around RNA and drive it to the surface of the lipid bilayer. At high pH the ionizable lipid is uncharged (DODMA0) and RNA leaves the bilayer surface.

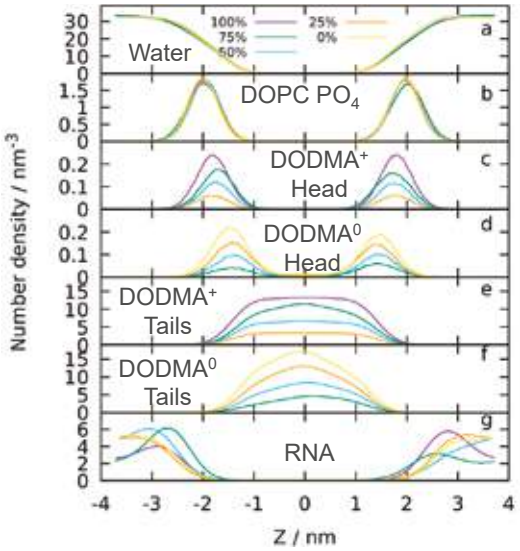

Uncharged ionizable lipids accumulate closer to the bilayer center.

Lipid dynamics

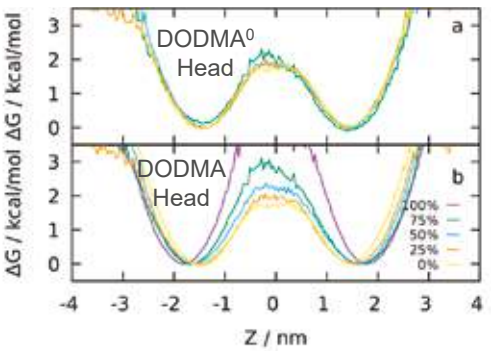

Uncharged ionizable lipids (DODMA0) undergo frequent flip-flop due to a low free energy barrier.

Binding free energy of ionizable lipids to RNA

The excess ionizable lipids om the vicinity of RNA report the binding free energy between the two species.

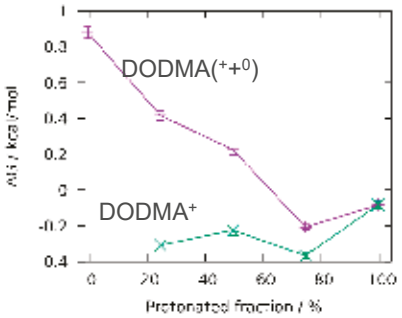

Protonated ionizable lipids have a favorable binding free energy, while uncharged DODMA0 are effectively repelled from RNA. Overall affinity between RNA and DODMA is then pH dependent and it becomes mildly attractive only at low pH.

RNA behavior

Charged ionizable lipids exert a pull on RNA.

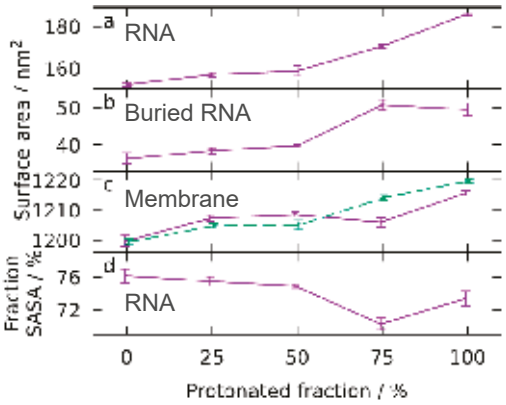

RNA is more stretched at low pH, and a larger surface area is buried into the lipid bilayer.

Methods

Simulations were performed using a **multiscale approach.**

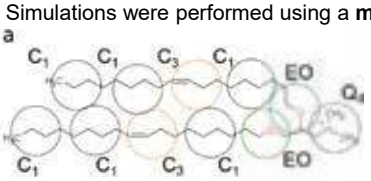

Atomistic (AA) and coarse-grained (CG) representation of DODMA+

System size 15nm x 15nm x 15nm. Number of molecules: 567 DOPC, 78 DODMA, 2 RNA_{40} . Total: 28000 CG beads, 170000 AA atoms. Simulations performed with GROMACS and CHARMM36 force field.

Coarse-grained representation of the complete system (water and ions are omitted for clarity). Lipid diffusion occurs rapidly in this setting. **Simulation length ~12μs.**

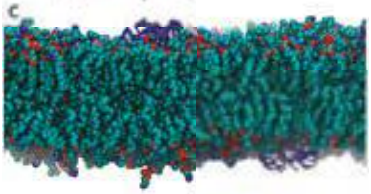

Atomistic representation of the system (water and ions are not shown). Accurate measure of properties. **Simulation length ~1μs.**

Reference

Settanni, G., Brill, W., Haas, H. and Schmid, F. (2022), pH-Dependent Behavior of Ionizable Cationic Lipids in mRNA-Carrying Lipoplexes Investigated by Molecular Dynamics Simulations. Macromol. Rapid Commun. 2100683. https://doi.org/10.1002/marc.202100683

Tumor-penetrating utorubicin-loaded polymersomes for cancer therapy

Valeria Sidorenko[1]*, Lorena Simón-Gracia[1]*, Ain Uustare[2], Ivan Ogibalov[2], Andrus Tasa[2], Olga Tshubrik[2], Tambet Teesalu[1]

[1]Laboratory of Precision and Nanomedicine, Institute of Biomedicine and Translational Medicine, University of Tartu, Tartu, Estonia
[2]Toxinvent LLC, Tartu, Estonia

INTRODUCTION

CendR peptides (sequence: R/KXXR/K) are tumor-penetrating peptides (TPPs) that bind to the neuropilin-1 (NRP-1) receptor overexpressed in tumor cells and tumor vasculature. The binding to NRP-1 triggers the penetration of CendR peptides and their cargo into tumor tissue [1-3] (Fig. 1). We developed polyethylene glycol-polycaprolactone (PEG-PCL) polymeric nanovesicles (polymersomes, PS) functionalized with CendR peptides and loaded with a novel anthracycline utorubicin (UTO). We showed that our nanosystem specifically targets, penetrates, and delivers UTO to tumor cells *in vitro,* accumulates in tumors *in vivo* [4], and has an anti-cancer effect in a mouse model of peritoneal carcinomatosis.

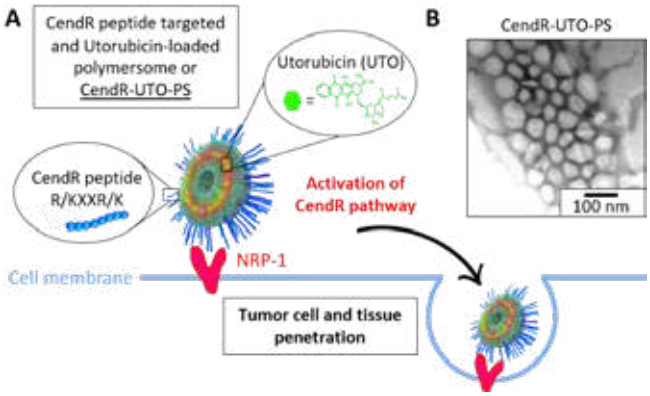

Figure 1. CendR peptide binding to NRP-1 and penetration mechanism. A) CendR peptide-targeted and utorubicin-loaded polymersomes (CendR-UTO-PS) and their penetration into the tumor cells. B) Transmission electron microscopy image of CendR-UTO-PS.

CYTOTOXICITY OF CendR-UTO-PS IN CULTURED CANCER CELLS

Our novel anthracycline UTO showed higher cytotoxicity than the clinically used doxorubicin (DOX) in different cultured cancer cell lines (Fig. 2A). With the aim to improve the biodistribution and tumor homing of UTO, it was encapsulated into polymersomes functionalized with a CendR peptide (CendR-UTO-PS). The cytotoxicity of CendR-UTO-PS was tested in cultured PPC-1 cells (expressing the CendR receptor, NRP-1). CendR-UTO-PS (at 2 µM UTO) showed significantly higher cytotoxicity than non-targeted UTO-PS in PPC-1 cells (Fig. 2B), demonstrating that the anti-cancer effect is potentiated by the binding of the CendR peptide to NPR-1.

A

IC_{50} (µM)	30 min		90 min	
	UTO	DOX	UTO	DOX
U937	0.3 ± 0.04	2.8 ± 0.6	0.1 ± 0.004	1.1 ± 0.1
Jurkat E6.1	0.2 ± 0.05	1.7 ± 0.8	0.3 ± 0.1	1.7 ± 0.5
A549	1.6 ± 0.2	11.4 ± 14.4	0.6 ± 0.1	10.1 ± 0.7
HT-29	0.9 ± 0.3	1.6 ± 0.2	0.7 ± 0.1	1.4 ± 0.9

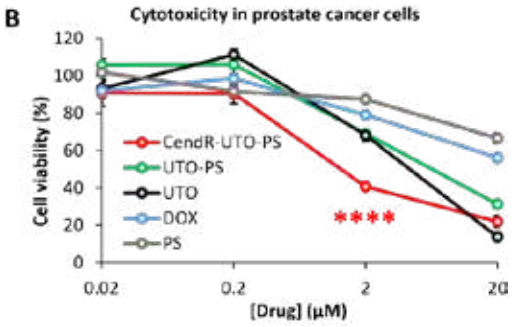

Figure 2. Cytotoxicity of free and nanoencapsulated UTO in cancer cells. A) Viability of cancer cells incubated with UTO or DOX for 30 or 90 min and chase in drug-free medium. IC_{50} (half-maximal inhibitory concentrations) ± SEM are shown, N=3. B) Viability of NRP-1 positive PPC-1 cells after incubation with PS formulations. After 30 min of PS incubation, the cells were washed and incubated for an additional 48 h. N=5, error bars= ± SEM.

CendR-TARGETED PS HOME TO TRIPLE NEGATIVE BREAST TUMORS

CendR-targeted and fluorescent-labeled PS (CendR-PS) along with non-targeted PS (PS) were systemically administered to mice bearing triple-negative breast tumor (MCF10CA1a) xenografts to evaluate the tumor homing of the PS. Live imaging was performed at different time points after PS administration. CendR functionalization significantly increased tumor homing of PS at early and late time points (Fig. 3). The highest tumor homing was observed after 24 and 48 h of CendR-PS injection (Fig. 3B), with the area under the curve (AUC) in tumors being ~40% higher than for non-targeted PS (Fig. 3C).

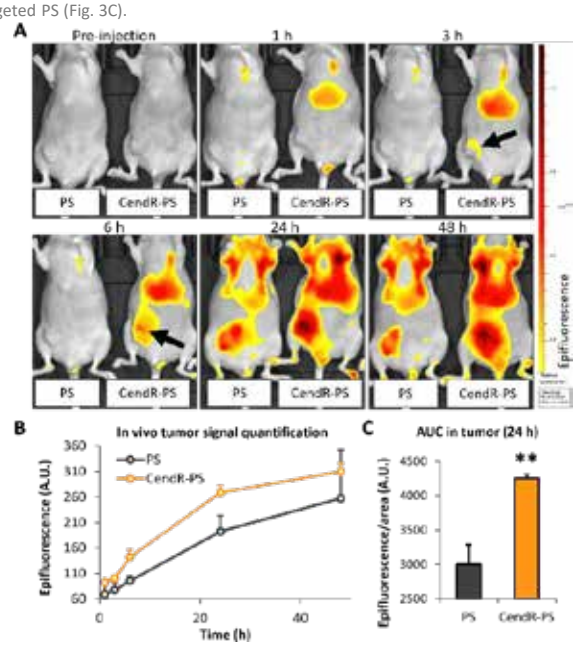

Figure 3. CendR-targeted fluorescent-labeled PS home to MCF10CA1a breast tumor. A) *In vivo* imaging of MCF10CA1a tumor-bearing mice injected with CendR-PS or non-targeted PS. B) Accumulation of PS in tumors at different time points post-injection. C) AUC in tumors at 24 h post-injection calculated from graph 3B. N=3, error bars= + SEM, ** p<0.01.

ANTI-TUMOR ACTIVITY OF UTO-PS IN GASTRIC TUMORS

To assess the anti-cancer effect of nanoformulated UTO, we performed an experimental treatment in mice bearing peritoneal carcinomatosis of gastric carcinoma origin (MKN45P). We observed efficient suppression of tumor growth in mice treated with UTO-PS in comparison with the control group (total UTO dose 13.3 mg/kg) (Fig. 4A). Importantly, the body weight in both groups did not differ significantly, suggesting no signs of systemic toxicity of UTO-PS (Fig. 4B). The therapeutic activity of CendR-UTO-PS is currently being evaluated.

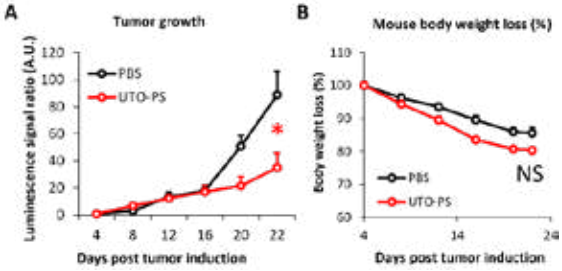

Figure 4. Experimental therapy of MKN45P tumor-bearing mice. Mice bearing disseminated peritoneal tumors induced with MKN45P cells were intraperitoneally injected with UTO-PS (1.4 mg UTO/kg) or PBS (500 µL) every other day. A) Tumor growth monitored by measurement of luciferase activity. B) Mouse body weight was monitored throughout the treatment. N=7 for UTO-PS and N=10 for PBS groups, error bars= + SEM, * p<0.05, NS = not significant.

CONCLUSION

We developed a tumor-specific nanoplatform that selectively delivers a novel drug candidate UTO to breast and peritoneal tumors and has an anti-cancer effect in a model of peritoneal carcinomatosis. Our study encourages further preclinical and clinical studies on UTO as a nanocarrier payload for precision cancer therapy with reduced drug side effects.

Eesti Teadusagentuur
Estonian Research Council
Horizon 2020

References

[1] Teesalu, T., Sugahara, K.N., Kotamraju, V.R. & Ruoslahti, E. (2009). C-end rule peptides mediate neuropilin-1-dependent cell, vascular, and tissue penetration. Proceedings of the National Academy of Sciences 106: 16157–16162.
[2] Sugahara, K.N., Teesalu, T., Karmali, P.P., Kotamraju, V.R., Agemy, L., Girard, O.M., Hanahan, D., Mattrey, R.F. & Ruoslahti, E. (2009). Tissue-Penetrating Delivery of Compounds and Nanoparticles into Tumors. Cancer Cell 8: 510–520.
[3] Simón-Gracia, L., Scodeller, P.D., Fuentes, S.S., … Teesalu, T. (2018) Application of polymersomes engineered to target p32 protein for detection of small breast tumors in mice. Oncotarget 9: 18682–18697.
[4] Simón-Gracia, L., Sidorenko, V., Uustare, A., Ogibalov, I., Tasa, A., Tshubrik, O. & Teesalu, T. (2021). Novel Anthracycline Utorubicin for Cancer Therapy. Angewandte Chemie - International Edition 60: 17018–17027.

NOVEL INSIGHTS ON ENDOSOMAL ESCAPE OF LIPID NANOPARTICLES USING REFLECTOMETRY TECHNIQUES

Alice Spadea[a,b], Mark Jackman[c], Lili Cui[c], Sara Pereira[c], M. Jayne Lawrence[a,b], Richard A. Campbell[b], Marianne Ashford[c]

[a]NorthWest Centre for Advanced Drug Delivery (NoWCADD) School of Health Sciences University of Manchester Oxford Road, Manchester M13 9PL, UK
[b]Division of Pharmacy and Optometry Faculty of Biology, Medicine and Health University of Manchester, Manchester Academic Health Science Centre Oxford Road, Manchester M13 9PL, UK
[c]Advanced Drug Delivery, Pharmaceutical Sciences, R&D, AstraZeneca, Cambridge, UK

Background

RNA delivery and gene therapy hold great potential for the treatment of many diseases. The realisation of RNA therapeutics in the clinic has been hindered due to:

- Instability in biological fluids;
- Lack of cell "targetability";
- Poor permeability of plasma membrane;
- **Escape of endosomal system**.

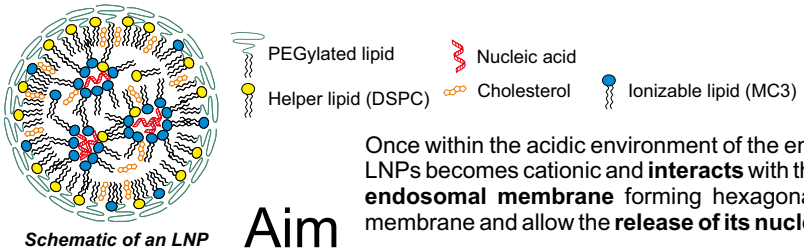

Schematic of an LNP

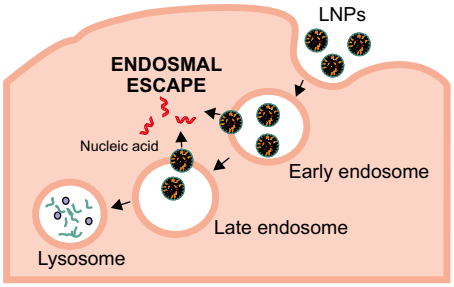

Aim

Once within the acidic environment of the endosome, the **ionisable lipid** contained in the LNPs becomes cationic and **interacts** with the anionic lipids present in the inner side of the **endosomal membrane** forming hexagonal structures that can ultimately disrupt the membrane and allow the **release of its nucleic acid cargo** into the cytosol.

Here, reflectometry techniques are used for the first time to study the **interactions of LNPs and models of endosomal membranes** (EEM) at different pHs to **understand the physicochemical processes** occurring.

Methods

Surface pressure

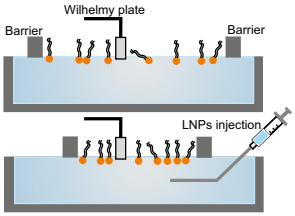

Measures changes in surface pressure/tension of Langmuir monolayers.

Brewster angle microscopy (BAM)

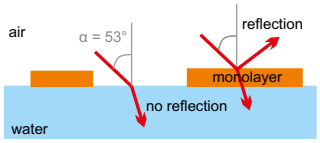

imaging technique used to observe the lateral characteristics of thin films.

Ellipsometry

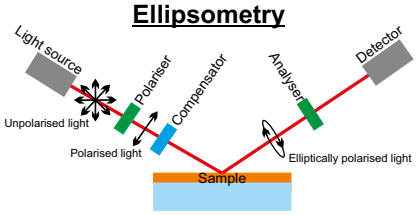

Measures the change in polarisation of light upon reflection at a planar (information on thickness of the sample).

Results

RNA-loaded LNPs pH 5.5 | RNA-free LNPs pH 5.5 | RNA-loaded LNPs pH 7.4

LNPs alone

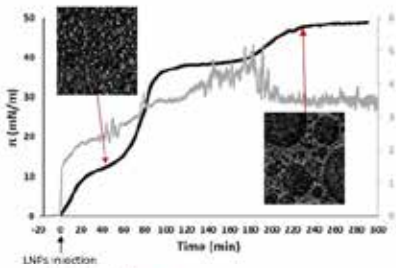

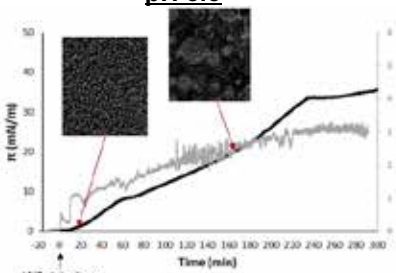

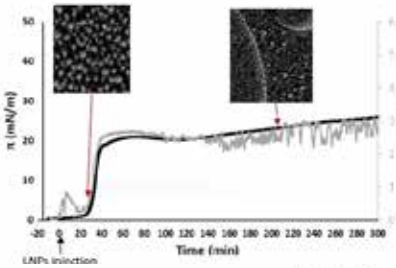

LNPs + EEM

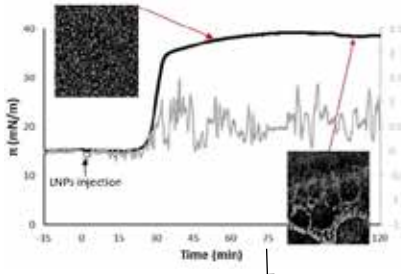

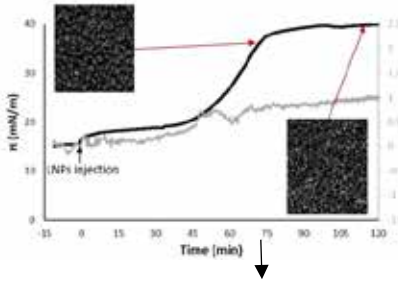

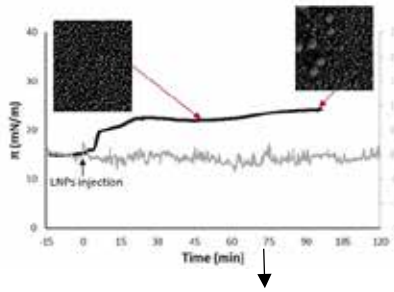

Conclusions

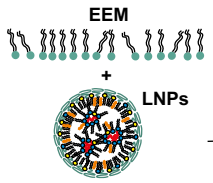

↑ Surface pressure
↑ Δint + bimodal distribution
Bright network BAM

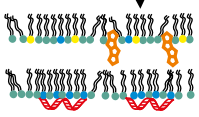

Lipids insertion

Ionisable lipid-RNA complex delivery

↑ Surface pressure
↑ Δint

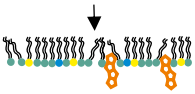

≈ Surface pressure
= Δint + bimodal distribution
Large/thick domains BAM

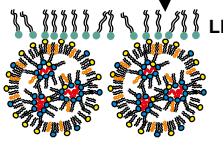

LNPs binding

Diverse Bioactivities of Biogenic SeNps Spur Cancer Cell-based Vaccine Potential

K. Spyridopoulou*, G. Aindelis, E. Tryfonopoulou and K. Chlichlia

Laboratory of Molecular Immunobiology, Department of Molecular Biology and Genetics, Democritus University of Thrace, Greece

*aikspiridopoulou@gmail.com

Background

Selenium (Se) exerts multiple and complex bioactivities, among which are regulation of immune responses and cancer cell growth inhibition. Recent clinical trials have demonstrated the anticancer properties of Se against colorectal cancer in specific. However, Se has a narrow therapeutic index, as higher doses are associated with adverse toxic effects. Selenium nanoparticles (SeNps) though, are more biosafe and more bioavailable Se forms. We employed the probiotic strain *Lactobacillus casei* ATCC 393 (LC) to synthesize biogenic SeNps, extracted them and assayed their bioactivity in colon cancer models.

Aim

To investigate the bioactivity of LC-derived biogenic SeNps in colon cancer cell models.

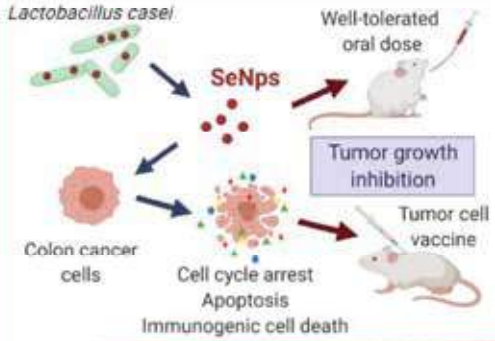

Materials & Methods

- Probiotic bacterial strain *L. casei* ATCC 393 cultured in the presence of $NaHSeO_3$ as a Se source.
- Extraction of SeNps with ultrasonication, NaOH treatment and vacuum filtration.
- UV-Vis, TEM, SEM-EDS, XRD.
- Murine CT26 and human HT29 and Caco-2 colon cancer cell lines.
- Murine primary healthy cells from colonic epithelium.
- Human biopsies of colon cancer or normal tissue.
- Syngeneic CT26 transplantable BALB/c mouse tumor model.
- SRB assay, ELISA, Western blot, Flow cytometry, Fluorescence confocal microscopy.
- Proteome Profiler Human Apoptosis Antibody Array kit.

References

Spyridopoulou, K. et al. Cancers (Basel). 13, 5335 (2021)
Spyridopoulou, K. *et al. Nanoscale Adv.* 3, 2516–2528 (2021)
Spyridopoulou, K. (PhD thesis, DUTh, Greece, 2018)

Part of this work was implemented by utilizing the facilities of the the project "InTechThrace: Integrated Technologies in biomedical research: multilevel biomarker analysis in Thrace" (MIS Code 5047285), under the Operational Program "Competitiveness, Entrepreneurship & Innovation" (EPAnEK), co-funded by the European Regional Development Fund (ERDF) and national resources (Partnership Agreement 2014-2020).

Results and Discussion

Extraction of 360 nm spherical SeNps capped with biomolecules from LC

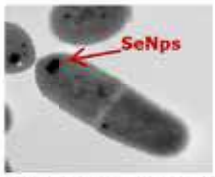

TEM images of the bacteria.

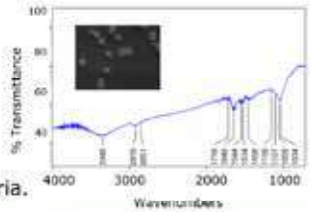

SEM images of extracted SeNps and their μ-FTIR spectrum.

Anticancer specificity

Healthy, EC_{50}= 72 μg/ml
Cancer, EC_{50}= 45 μg/ml

$$SI = \frac{EC50_{\mu}}{EC50_{c}} = 1.6$$

SI: Selectivity index > 1.

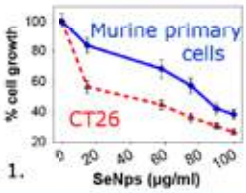

In vitro bioactivity in colon cancer models

CT26, Caco-2 and HT29 colon cancer cells; Murine primary cells; Human biopsies	
Anti-proliferative	Cell growth inhibition, G0/G1 cell cycle arrest, ↑ p21 and p27, ↓ k-67, Survivin
Cancer specificity	Murine primary healthy cells from colon epithelium compared to CT26 cancer cells. Cancer tissue and HT29 cells compared to healthy tissue from human biopsies.
Pro-apoptotic	↑ c-cas3, M30 antigen
	↑ AnnexinV+/PI-, c-cas3, Bax, Puma, TRAIL, c-PARP1, cytochrome c ↓ cas3, Bcl-2, Bcl-xl, Mcl-1, cIAP1, HSP27, HSP70, Survivin, TRAIL DR4 and DR5
Oxidative stress	↑ XIAP, PON2, catalase, ROS ↓ HIF-1a
Immunogenic cell death	↑ cyto HMGB1, cell surface Calreticulin and ERp57, secretion of TNF-α, IL-6, IL-8 ↓ nucl HMGB1, intracellular ATP

Prophylactic SeNps-based strategies prior tumor cells challenge in mice

1) *Per os* administration

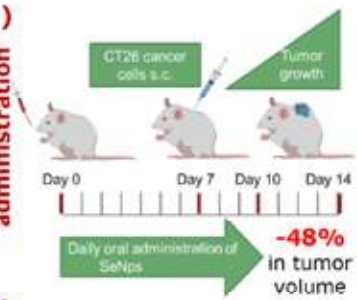

-48% in tumor volume

2) Vaccination with SeNps-treated CT26 cells 7 d prior challenge

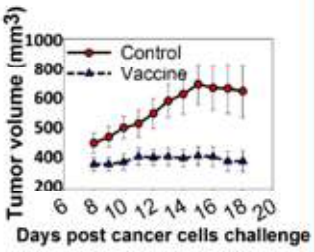

Inhibition of tumor growth upon
1) prophylactic SeNps oral administration
2) vaccination with SeNps-treated tumor cells.

Conclusions

Our results indicate that the SeNps derived from *L. casei* ATCC 393 exert cancer-specific growth inhibitory effects and induce apoptosis, cell cycle arrest and immunogenic cell death in colon cancer cells. Our research highlights the diverse bioactivities of the SeNps that could be linked to the various bacteria-derived biomolecules associated with the nanoparticles. These SeNps, could pose the basis for the development of novel combined-modality treatment approaches against colon cancer.

Application of lysine-based peptide dendrimers D3K2, D3R2, and D3H2 for gene delivery: A functional transfection study *in vitro*

Piotr Tarach[1*], Maciej Sobczak[1], Magdalena Strachowska[1], Irina Tarasenko[3], Emil Fatullaev[2], Igor Neelov[2], Agnieszka Robaszkiewicz[1], Barbara Klajnert-Maculewicz[1], Anna Janaszewska[1*]

[1]Department of General Biophysics, Faculty of Biology and Environmental Protection, University of Lodz, Lodz, Poland

[2]St. Petersburg National Research University of Information Technologies, Mechanics and Optics (ITMO University), St. Petersburg, Russia

[3]Institute of Macromolecular Compounds Russian Academy of Sciences, St. Petersburg, Russia

Abstract

Dendrimers are highly branched, three-dimensional, spherical molecules with well-defined sizes, ranging from 1 nm to about 15 nm for dendrimers with 1 to 10 spherical layers (generations). They have unique physicochemical properties, including low cytotoxicity, efficient cell penetration, and the ability to simultaneously deliver both genetic material and drugs into cells. The most used dendrimers are polyamidoamine, poly(propylene imine), and poly-L-lysine (PLL). PLL dendrimers consist of only lysine residues. In this study, we inserted linear-dipeptide spacers between the neighboring branched-lysine residues of a standard third-generation lysine dendrimer to generate the following third-generation, PLL-based peptide dendrimers: D3K2, containing lysine-dipeptide spacers; D3R2, containing arginine-dipeptide spacers; and D3H2, containing histidine-dipeptide spacers. We show that D3K2, D3R2, and D3H2 peptide dendrimers can silence expression of an important pro-inflammatory-response gene, nuclear factor kappa B (NF-κB) when used to transfect cells with an siRNA directed against the NF-κB subunit p65 *in vitro*. D3K2, D3R2, and D3H2 transfected cells with anti-p65 siRNA and reduced the expression of the p65 subunit as efficiently as Lipofectamine 2000. These results suggest that dendrimers may have potential for the future development of innovative gene therapies.

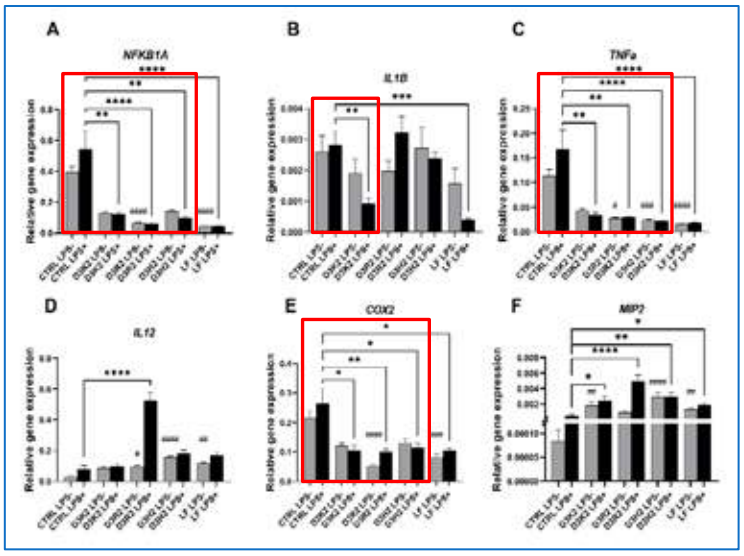

Fig. 1. Relative levels of gene expression in HeLa cells after dendrimer transfection of siRNA.

Conclusions

The results of this study support our hypothesis that PLL-based D3K2, D3R2, and D3H2 peptide dendrimers efficiently deliver siRNA to inhibit p65 expression in HeLa cell line. Transfection with dendrimers reduced p65 expression at least as efficiently as did transfection with Lipofectamine 2000. These results indicate that dendrimers may be used as *in vivo* carriers in future studies of innovative gene therapies. The sizes, internal structures, and dynamic properties of D3K2, D3R2, and D3H2 dendrimers as determined by molecular dynamic simulations agree well with our experimental data.

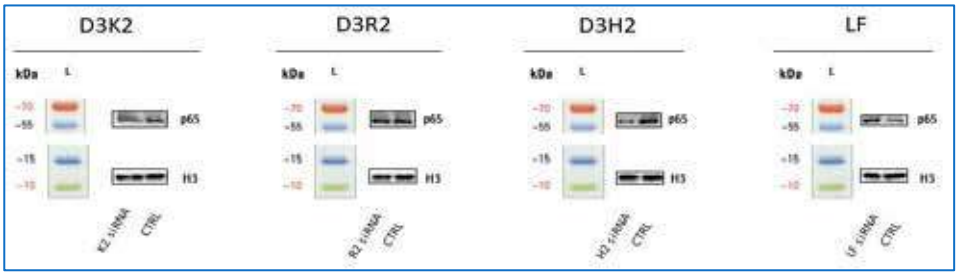

Fig. 2. Immunoblot measurements of gene expression in HeLa cells after transfection with siRNA-containing dendriplexes.

Acknowledgments: I.M. Neelov and E. Fatullaev were supported by grants 20-53-12036 and 20-33-90292 from the Russian Foundation for Basic Research (RFBR). I.I. Tarasenko was supported by the Russian Ministry of Science and Higher Education under State Contract No.14.W03.31.0022.

The conference costs were covered by University Of Lodz Doctoral School Of Exact And Natural Sciences.

Martin Telefont

EBRAINS

Co-funded by the European Union

This research has received funding from the European Union's Horizon 2020 Framework Program for Research and Innovation under the Specific Grant Agreement No. 945539 (Human Brain Project SGA3).

EBRAINS is an AISBL registered in Belgium. It serves as the central hub of a distributed Research Infrastructure tasked with continuing efforts to build and develop a Brain Research Infrastructure. This effort was started in 2013 with the start of the EC-FET Flagship Human Brain Project and has seen contributions from 120+ partners over the decade of work it has active.

EBRAINS has been successful in its application for admittance to the ESFRI Roadmap 2021 and is actively preparing for the transition from project based development and support to research infrastructure development and support.

This poster gives a short overview of services hosted on EBRAINS which could be of interest to members of the nanomedicine community and advances researchers have achieved leveraging it in various settings (e.g. neurology, neurosurgery) and contexts (academia, clinical).

EBRAINS in the RI landscape

EBRAINS is the only pan-European digital distributed infrastructure in Brain Science

EBRAINS is addressing an existing need of researchers in several European Countries for refined research tools and services

341 "research infrastructures" providing services to support "Biological and Medical Sciences"

8 of the 341 are explicitly concerned with neuroscience, and all are **single-site, national bodies**

EBRAINS complements the landscape and promotes **synergies across the still fragmented neuroscience activities in Europe**

EBRAINS selected for the ESFRI Roadmap 2021

The ESFRI Roadmap arguably contains the best European science facilities based on a thorough evaluation and selection procedure

ESFRI's mission is

- to develop the scientific integration of Europe
- to strengthen its international outreach
- and to provide Europe with the most up -to-date Research Infrastructures, responding to the rapidly evolving Science frontiers, also advancing the knowledge -based technologies and their extended use

EBRAINS RI - Life-cycle

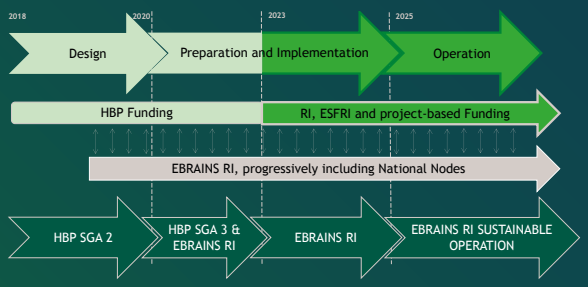

Each EBRAINS service is a building block

EBRAINS is moving towards developing its services following a modular design

Each tool has a separated functionality of the full service. Making it independent and interchangeable, such that it contains everything necessary to execute only one aspect of the desired workflow

EBRAINS is open for collaborations in order to further develop versatile tools that are of interest of the Scientific community

Covering and ensuring equilibrium between three areas:

Neuroscience | **Brain Medicine** | **Brain-inspired technologies**

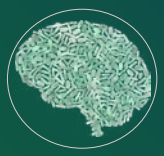

EBRAINS data amplification capacity

Clinical decision support tools tailored to the individual, applied in clinical trials

Multiscale integration to identify key mechanisms that predict disease progression for novel therapeutic solutions

High performance computing enables high-resolution individualization and extension to modelling cohorts

EBRAINS offers a focused and deep range of services

Data and Knowledge
- Online solutions to facilitate sharing of and access to research data, computational models and software

Atlases
- Navigate, characterise and analyse information on the basis of anatomical location

Simulation
- Solutions for brain researchers to conduct sustainable simulation studies and share their results

Brain-Inspired Technologies
- Understand and leverage the computational capabilities of spiking neural networks

Medical Data Analytics
- The Medical Data Analytics service provides two unique EBRAINS platforms, covering key areas in clinical neuroscience research

The Virtual Brain workflow at EBRAINS

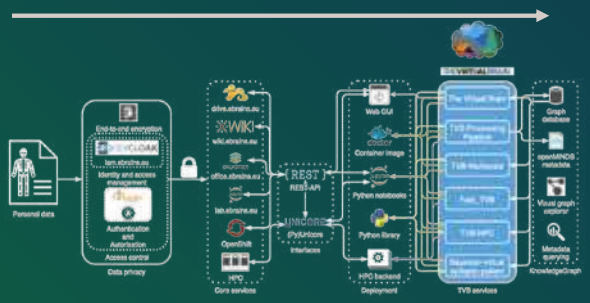

Julius-Maximilians-UNIVERSITÄT WÜRZBURG

Universitätsklinikum Würzburg
Klinik und Poliklinik für Zahn-, Mund-, und Kieferkrankheiten
Abteilung für Funktionswerkstoffe der Medizin und der Zahnheilkunde

fmz Funktionswerkstoffe der Medizin und Zahnheilkunde

Engineering nanogels for drug delivery to pathogenic *Aspergillus fumigatus*

Theresa Vogel[1], Yidong Yu[2], Andreas Beilhack[2], Jürgen Groll[1] and Krystyna Albrecht[1]*

[1]Department for Functional Materials in Medicine and Dentistry at the Institute of Functional Materials and Biofabrication (IFB), University of Würzburg, Pleicherwall 2, D-97070 Würzburg, Germany; URL: www.fmz.uni-wuerzburg.de

[2]Interdisciplinary Center for Clinical Research Laboratory for Experimental Stem Cell Transplantation, Department of Internal Medicine II, University Hospital of Würzburg, Zinklesweg 10, D-97078 Würzburg, Germany

*E-mail: krystyna.albrecht@fmz.uni-wuerzburg.de

Introduction

The opportunistic mold *Aspergillus fumigatus* is one of the main fungal pathogens causing invasive infections in immunocompromised humans. Unfortunately, conventional antifungal agents are associated with low therapeutic efficacy and/or severe side effects.[1] A promising alternative treatment approach is nanoparticle-based antifungal therapy. It leads to increased drug bioavailability and reduced toxicity, both boosting treatment efficacy.[2]

We previously showed that poly(glycidol)-based nanogels (NGs) have great potential when being used as vehicle for antifungals but need improvement when being co-incubated with fungus in the presence of serum.[3] In this study the nanogels were modified to increase their affinity towards the positively charged cell wall of fungal hyphae by tuning their surface charge (ζ) to more negative values.

Previous studies - no interaction visible in the presence of serum

Co-incubation of NGs in medium with 2% FBS

ζ_{LDE} = -27 ± 0.9 mV
Z-Ave$_{DLS}$ = 254 ± 5 nm
PDI$_{DLS}$ = 0.163 ± 0.2

→ Modification necessary
→ Investigation with *ex vivo* PCLS model (0.1% FBS)

Precision-cut lung slices(PCLS) model

[4]

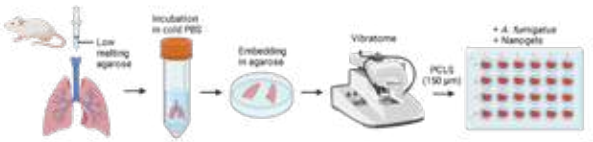

Nanogel synthesis: nanoprecipitation, quenching with 2-carboxyethyl acrylate (CEA)

[4]

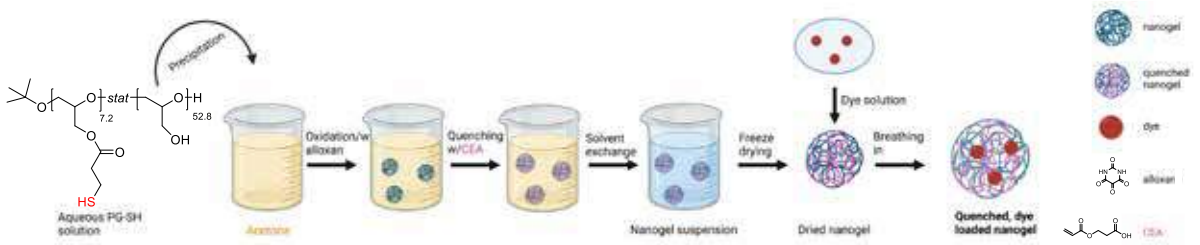

PCLS experiments – analyzed by confocal microscopy

Nanogels loaded with hydrophilic dye Rhodamine 6G

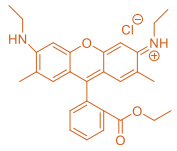

Rhodamine 6G

ζ_{LDE} = -30 ± 0.3 mV
Z-Ave$_{DLS}$ = 432 ± 10 nm
PDI$_{DLS}$ = 0.140 ± 0.07

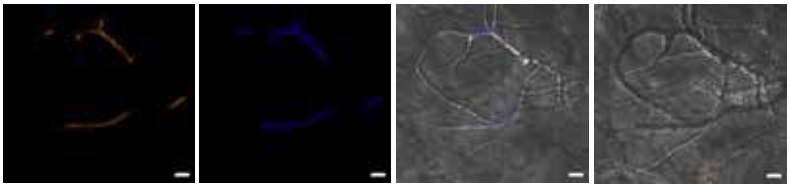

Nanogels loaded with hydrophobic dye Atto647N Maleimide

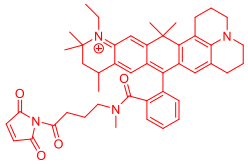

ATTO647N-Maleimid

ζ_{LDE} = -33 ± 0.2 mV
Z-Ave$_{DLS}$ = 366 ± 4 nm
PDI$_{DLS}$ = 0.145 ± 0.04

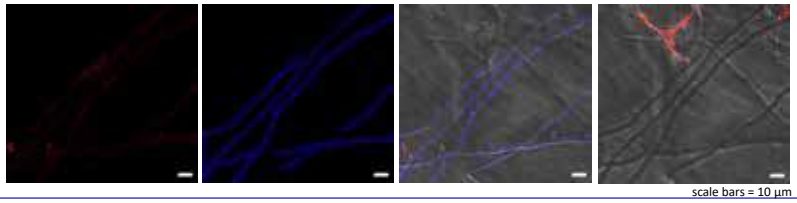

scale bars = 10 µm

Conclusions

Nanogel preparation via precipitation and the modification to a more negative surface charge, as well as the loading of cargo via breathing-in were successful. *Ex vivo* studies using the PCLS model showed that cargo has a clear impact on fungal uptake of nanogels, as those with hydrophilic cargo were well taken up by the fungus and only slightly taken up by the PCLS, while nanogels with hydrophobic cargo were barely taken up by the fungus and showed clear uptake by the PCLS.

Outlook

These results encourage future studies to further improve the interaction of nanogels with fungus as well as the functionalization of nanogels with different targeting moieties and loading with antifungal agents.

References

[1] Y. Yu et al., Expert Opin. Investig.Drugs 2020, 29, 961-971. [2] D. A.Szalewski et al., Can. J. Microbiol. 2018, 453, 439-453. [3] S. Horvat et al., NanoBiomed Res. 2021, 1, 2000060. [4] Created with BioRender.com<https://biorender.com/>

A polyoxometalate incorporating, injectable hydrogel with pH- and NIR-responsiveness for chemo-photothermal therapy

Shiqi Wang University of Helsinki shiqi.wang@helsinki.fi

Project Design

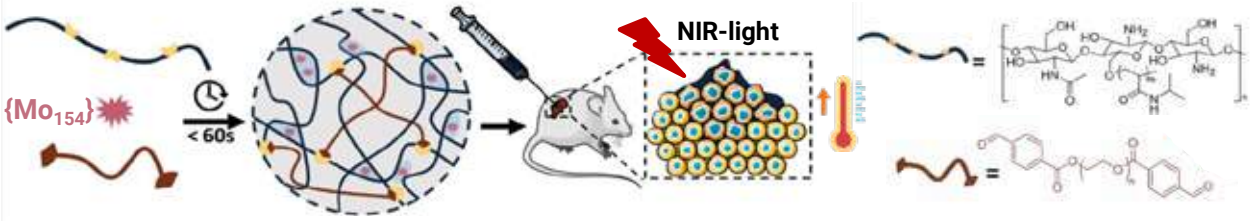

- Fast in-situ gelation
- Laser-induced thermal ablation of tumor
- Laser/pH-controlled drug release

Hydrogel preparation/characterization

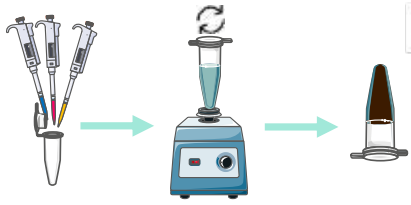

Simply mixing all the components

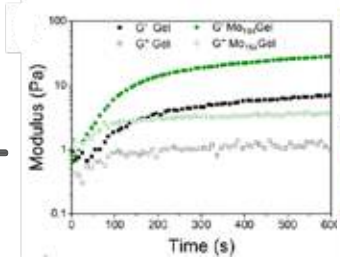

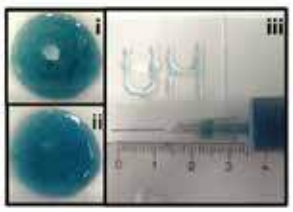

- Fast hydrogel formation < 60s
- Fast self-healing after damage, injectable

pH- and NIR-responsiveness

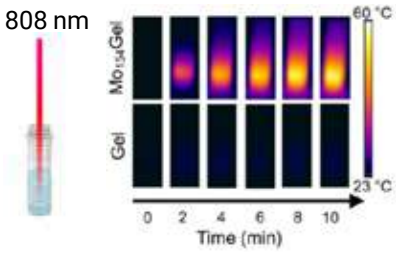

Efficient photothermal behavior of Mo_{154}Gel

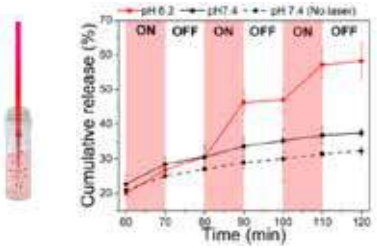

pH- and NIR-controlled DOX release

Chemo-photothermal therapy *in vivo*

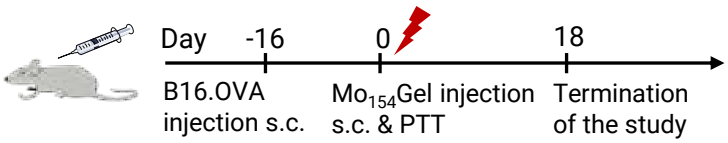

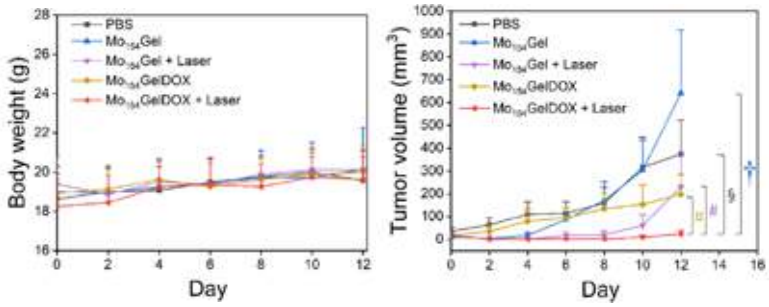

- The combination therapy led to better therapeutic outcomes compared with either chemotherapy or photothermal therapy alone

More details in: Advanced Materials, 2007761. https://doi.org/10.1002/adma.202007761

Comparative analysis of nucleic acid-based adjuvants for the activation of dendritic cells (DC) to improve nano-vaccines

Yanira Zeyn, Matthias Bros
University Medical Center Mainz, Dept. of Dermatology

SFB 1066

Background

- Trimannosylated liposomes address DC (dendritic cells)

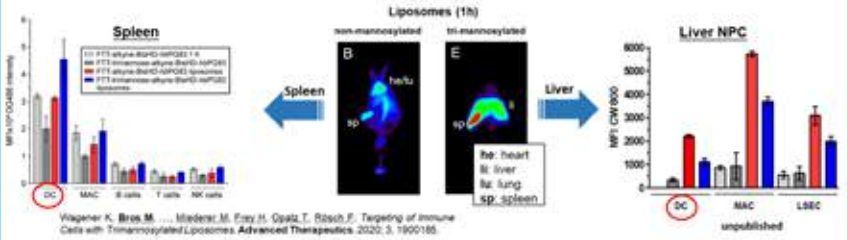

Figure 1

Screening of CpG Oligos regarding DC stimulatory activity

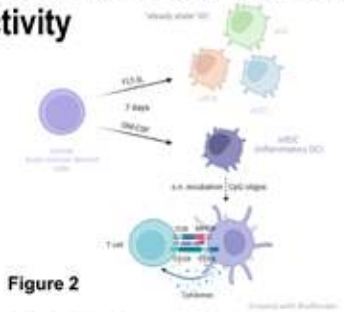

Figure 2

Table 1

CpG name	5'-3' sequence	CpG class
ODN1585	GGGGTCAACGTTGAGGGGGG	A (induce high IFN-α production from pDC)
ODN2336	GGGGACGACGTCGTGGGGGGG	
ODN1668	TCCATGACGTTCCTGATGCT	B (strongly activate B cells; induce weak IFN-α secretion)
ODN1826	TCCATGACGTTCCTGACGTT	
ODNSL01	TCGCGACGTTCGCCCGACGTTCGGTA	
ODN2395	TCGTCGTTTTCGGCGCGCGCCG	C (combination of A + B)
ODNM362	TCGTCGTCGTTCGAACGACGTTGAT	
ODNSL03	TCGCGAACGTTCGCCGCGTTCGAACGCCG	

For the following experiments we are using murine bone marrow derived DC, differentiated from bone marrow with either GM-CSF, yielding a rather homogenous population of inflammatory (inf)DC, or FLT3L giving rise to a heterogeneous composition of DC subpopulations (cDC1, cDC2, pDC) (**Fig. 2**).

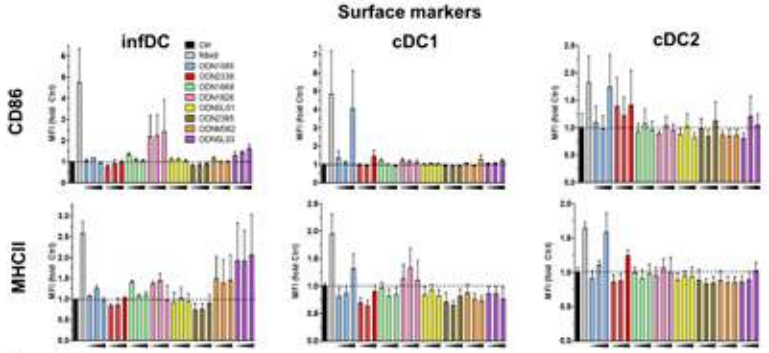

Figure 3

DC were incubated with different concentrations of CpG oligos (50, 100 or 250 ng/ml) or the TLR 7/8 ligand R848 (1 µg/ml). On the next day, expression of MHCII and CD86 by inflammatory (inf) DC and cDC1/2 was assessed by flow cytometric analysis (**Fig. 3**).

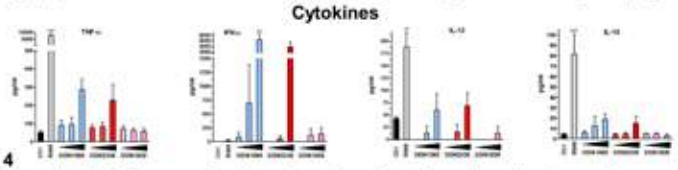

Figure 4

FLT3L-differentiated DC were stimulated and incubated as described and supernatants were retrieved before subjecting cells to surface marker analysis. Cytokine concentrations were assayed by CBA (**Fig. 4**). Data denote the mean±SD of 3 experiments. Statistical differences versus *Ctrl are indicated (one way ANOVA, Tukey test). **p<0.01, ***p<0.001.

Project aim

It is conceivable that only a limited number of nano-vaccines will transfect a given DC, which means that the amount of co-delivered adjuvant will be very limited.
In order to yield maximal stimulation of DC in secondary lymphoid organs and liver (**Fig. 1**), it may be beneficial to co-deliver besides antigen-encoding mRNA that may trigger TLR3 also different types of stimulatory nucleic acid-based adjuvants, which activate distinct danger receptors converging on the level of gene expression. Therefore, co-administration of mRNA in combination with various types of stimulatory nucleic acid-based adjuvants may yield synergistic effects in terms of DC activation.

We have started to screen various CpG-containing oligodesoxynucleotides (CpG oligos) known to trigger TLR9 (**Tab. 1**) as well as DNA oligos that engage cytoplasmatic DNA sensors (CDS, see Outlook) to identify which within either group yield maximal DC activation and may exert synergistic effects when co-applied.

Conclusion / Outlook

The preliminary results show the DC population-specific efficacy of the respective CpG oligos which are the base for further adjuvant analysis.
Ongoing experiments are dedicated to evaluate the suitability of virus-derived DNA oligos (HSV60, ISD, VAVC70, Poly(dA:dT); see **Tab. 2**) which trigger cytoplasmic DNA sensors such as STING for DC stimulation. As a next step potential synergistic effects of both types of nucleic acid-based adjuvants will be evaluated (**Fig. 5**).

Table 2

CDS name	Derived from
HSV-60	herpes simplex virus 1
ISD (Interferon stimulatory DNA)	*Listeria monocytogenes*
VACV-70	vaccinia virus
Poly(dA:dT)	repetitive synthetic double-stranded DNA

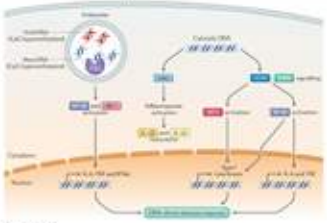

Figure 5

Motwani, M., Pesiridis, S. & Fitzgerald, K.A. DNA sensing by the cGAS–STING pathway in health and disease. Nat Rev Genet 20, 657–674 (2019).